Interactions between turbulent convection and thermal radiation in direct numerical simulations

DISSERTATION
zur Erlangung des akademischen Grades
Doktor-Ingenieur (Dr.-Ing.)

vorgelegt der
Fakultät für Maschinenbau der
Technischen Universität Ilmenau

von Dipl.-Ing.
TOMASZ CZARNOTA

Gutachter:

Univ.-Prof. Dr.-Ing. habil. Claus Wagner
Technische Universität Ilmenau

Univ.-Prof. Dr. rer. nat. habil. Jörg Schumacher
Technische Universität Ilmenau

Prof. Dr.-Ing. Heinz Herwig
Technische Universität Hamburg-Harburg

Tag der Einreichung: 27. Mai 2016
Tag der wissenschaftlichen Aussprache: 19. Dezember 2016

Deutsches Zentrum für Luft- und Raumfahrt e.V.
Institut für Aerodynamik und Strömungstechnik
Abteilung Fluidsysteme
Bunsenstraße 10
37073 Göttingen

Technische Universität Ilmenau
Fakultät für Maschinenbau
Institut für Thermo- und Fluiddynamik
Fachgebiet Aerodynamik
Helmholtzring 1
98693 Ilmenau

urn:nbn:de:gbv:ilm1-2016000777

Omnia possum in eo qui me confortat

Erklärung

Ich versichere, dass ich die vorliegende Arbeit ohne unzulässige Hilfe Dritter und ohne Benutzung anderer als der angegebenen Hilfsmittel angefertigt habe. Die aus anderen Quellen direkt oder indirekt übernommenen Daten und Konzepte sind unter Angabe der Quelle gekennzeichnet.

Bei der Auswahl und Auswertung folgenden Materials haben mir die nachstehend aufgeführten Personen in der jeweils beschriebenen Weise unentgeltlich geholfen:

1. Herr Claus Wagner hat mich in seiner Funktion als mein Doktorvater und fachlicher Betreuer dieser Arbeit im herkömmlichen Umfang im Rahmen von themenbezogenen Diskussionen angeleitet.

Weitere Personen waren an der inhaltlich-materiellen Erstellung der vorliegenden Arbeit nicht beteiligt. Insbesondere habe ich hierfür nicht die entgeltliche Hilfe von Vermittlungs- beziehungsweise Beratungsdiensten (Promotionsberater oder anderer Personen) in Anspruch genommen. Niemand hat von mir unmittelbar oder mittelbar geldwerte Leistungen für Arbeiten erhalten, die im Zusammenhang mit dem Inhalt der vorgelegten Dissertation stehen.

Die Arbeit wurde bisher weder im In- noch im Ausland in gleicher oder ähnlicher Form einer Prüfungsbehörde vorgelegt.

Ich bin darauf hingewiesen worden, dass die Unrichtigkeit der vorstehenden Erklärung als Täuschungsversuch bewertet wird und gemäß §7 Abs. 10 der Promotionsordnung den Abbruch des Promotionsverfahrens zur Folge hat.

Berlin, 16. Mai 2016

Abstract

In the present work, the interactions between turbulent convection and surface-to-surface radiation are investigated by means of direct numerical simulations. The examined domain is a cuboidal Rayleigh–Bénard cell bounded by horizontal plates of finite thickness. The simulations are conducted for the Prandtl number $Pr = 0.7$, Rayleigh numbers ranging from $Ra = 3.5 \times 10^5$ to $Ra = 6.3 \times 10^7$, radiation numbers between $Nr = 0.0008$ and $Nr = 0.0026$, and temperature ratios between $\Theta = 29$ and $\Theta = 45$. Additionally, the thermal diffusivity ratio is set at $\lambda_\kappa = 0.003$ and $\lambda_\kappa = 3.8$. Moreover, blackbody radiation is considered, and the side walls are assumed to be transparent to radiation but adiabatic for conduction.

The large-scale circulations are found to be larger in the presence of radiation and to render the bulk more uniform. Moreover, the radiation-induced decrease of the turbulence intensities in the bulk is found to vary with Ra and the plates' conductivity. Furthermore, when $\lambda_\kappa = 0.003$, radiation visibly affects the temperature of the heat sources by cooling the heating plates and heating the cooling plates. The intensity of these changes is, however, spatially dependent. Thus, the temperatures of the cold plumes are affected equally by radiation, while those of the hot plumes are affected differently, depending on their location. On the other hand, when $\lambda_\kappa = 3.8$, the hot and cold plumes are similar in the absence and presence of radiation.

The evaluation of the Nusselt number shows that the radiative heat flux contributes considerably to the total one, particularly for low conductivity plates and low Ra. Moreover, the radiative heat transfer increases faster with Nr than with Θ. Furthermore, when $\lambda_\kappa = 0.003$, the convective drop is observed. It is found that in regions where the plumes emerge, only the radiative heat flux and its intensity are responsible for this drop, while in regions where the plumes arrive, the convective heat transported by the arriving plumes contributes as well.

Reducing the complexity level of the boundary conditions by neglecting radiation or temperature deviations does not influence the mean temperature above which the development of plumes starts. However, the predicted sheet-like plumes are colder and larger. This temperature decrease is caused by the overproduction of the moderately warm plumes at the cost of the underproduction of the warmest plumes in the centre and close to the lateral walls.

Kurzfassung

Das Ziel der vorliegenden Arbeit ist die Untersuchung der Interaktionen zwischen turbulenter Konvektion und Oberflächenstrahlung durch direkte numerische Simulationen. Bei dem untersuchten Bereich handelt es sich um eine quaderförmige Konvektionszelle, die durch horizontale Platten endlicher Dicke begrenzt ist. Die Simulationen werden für die Prandtl–Zahl $Pr = 0,7$, Rayleigh–Zahlen im Bereich von $Ra = 3,5 \times 10^5$ bis $Ra = 6,3 \times 10^7$, Strahlungszahlen zwischen $Nr = 0,0008$ und $Nr = 0,0026$ und Temperaturverhältnissen zwischen $\Theta = 29$ und $\Theta = 45$ durchgeführt. Zusätzlich ist das Verhältnis der Temperaturleitfähigkeit auf $\lambda_\kappa = 0,003$ und $\lambda_\kappa = 3,8$ eingestellt. Darüber hinaus wird die Schwarzkörperstrahlung betrachtet; dabei geht man davon aus, dass die Seitenwände für die Strahlung durchlässig sind, nicht jedoch für die Wärmeleitung.

Die großskaligen Konvektionsrollen sind in Gegenwart von Strahlung größer und sie machen den Bulk gleichförmiger. Überdies ist die durch die Strahlung induzierte Senkung der Turbulezintesität im Bulk von der *Ra* und der Plattenleitfähigkeit abhängig. Bei $\lambda_\kappa = 0,003$ beeinflusst die Strahlung die Temperatur der Wärmequellen sichtbar: die Heizplatten werden gekühlt und die Kühlplatten erwärmt. Die Intensität dieser Veränderungen ist jedoch ortsabhängig. Dadurch werden strahlungsbedingt die Temperaturen der kalten *Plumes* gleichmäßig beeinflusst, während die Temperaturen der heißen *Plumes* unterschiedlich betroffen sind, je nach ihrer Lage. Bei $\lambda_\kappa = 3,8$ sind die heißen und kalten *Plumes* sowohl in Gegenwart als auch in Abwesenheit von Strahlung ähnlich.

Die Auswertung der Nusselt–Zahl zeigt, dass die Wärmestromdichte der Strahlung wesentlich zur Gesamtwärmestromdichte beiträgt, besonders bei den Platten mit geringer Leitfähigkeit und niedrigen *Ra*. Darüber hinaus erhöht sich der Strahlungsaustausch mit der *Nr* schneller als mit Θ. Außerdem wird bei $\lambda_\kappa = 0,003$ der konvektive Abfall festgestellt. Die Untersuchungen ergaben, dass in Regionen, in denen die *Plumes* entstehen, nur die Wärmestromdichte der Strahlung und ihre Intensität für diesen Abfall verantwortlich sind, während in Regionen, wo die *Plumes* ankommen, die durch die ankommenden *Plumes* verursachte konvektive Wärme ebenfalls eine Rolle spielt.

Wenn man das Komplexitätsniveau der Randbedingungen reduziert, so dass die Strahlung oder die Temperaturabweichungen vernachlässigt sind, beginnt

die Entwicklung der thermischen *Plumes* bei ähnlichen Durchschnittstemperaturen. Jedoch sind die vorhergesagten flächigen *Plumes* kälter und größer. Dieser Temperaturabfall wird durch die Überproduktion der mäßig warmen *Plumes* auf Kosten der Unterproduktion der wärmsten *Plumes* in der Mitte und bei den Seitenwänden verursacht.

Contents

Nomenclature

Latin symbols

A	area
$\mathscr{A}, \mathscr{B}, \mathscr{C}$	fitting coefficients
$\hat{g}$	gravitational acceleration
h_s	height of the solid plates
H	height of the fluid layer
k	thermal conductivity
L	length of the fluid layer
Nr	radiation number $Nr = \hat{\sigma}\hat{\Delta T}^3 \hat{H}/\hat{k}_f$
Pr	Prandtl number $Pr = \hat{\nu}/\hat{\kappa}_f$
q	rate of energy
$\dot{q}$	heat flux
Ra	Rayleigh number $Ra = \hat{\beta}\hat{g}\hat{H}^3\hat{\Delta T}/\hat{\nu}\hat{\kappa}_f$
Re	Reynolds number $Re = \hat{U}\hat{H}/\hat{\nu}$
ts	time step
T	temperature
ΔT	temperature difference $\Delta T = T_{bot} - T_{top}$
T_0	mean bulk temperature $T_0 = 0.5\left(T_{bot} + T_{top}\right)$
TIR	elapsed time steps until recalculation of irradiation
u_i	Cartesian velocity components; i=1, 2, 3 $\equiv u, v, w$
U	mean large-scale velocity
W	width of the fluid layer
WCT	Wall Clock Time
x_i	position in the Cartesian coordinate system; i=1, 2, 3 $\equiv x, y, z$

Greek symbols

α	absorptivity

β	isobaric thermal expansion coefficient
δ	standard deviation
δ_{ij}	Kronecker delta
ϵ	dissipation rate
ε	emissivity
ζ	fitting function
η	microscales of turbulence
ϑ	function for conditionally averaged quantities
Θ	temperature ratio $\Theta = \hat{T}_0/\hat{\Delta T}$
κ	thermal diffusivity
λ_k	thermal conductivity ratio $\lambda_k = \hat{k}_s/\hat{k}_f$
λ_κ	thermal diffusivity ratio $\lambda_\kappa = \hat{\kappa}_s/\hat{\kappa}_f$
ν	kinematic viscosity
ξ	fitting function for PDF_T
ρ	density
σ	Stefan–Boltzmann constant $\sigma = 5.67 \times 10^{-8}\ \left[W/m^2 \cdot K^4\right]$
τ	transmissivity
ϕ	polar angles
ψ	fitting function for Ra, Nr and Θ

Indices

bot	bottom solid plate
bulk	bulk
cond	conductive
c	convective
diff	difussive
e	emissive
eff	effective quantity
f	fluid layer
ir	irradiative
NRM	Newton–Raphson's method
out	ambient environment
r	radiative
s	solid layer
sw	side walls
t	time
rms	the root mean square of a varying quantity
top	top solid plate
TSE	Taylor Series Expansion
V	volume

Abbreviations

BC	boundary condition
DNS	direct numerical simulations
HCP	highly conductive plates of a finite thickness
IC	interface condition
ITP	infinitely thin plates with homogeneous temperature distribution
ITP-nh	infinitely thin plates with non-homogeneous temperature distribution
LCP	low conductivity plates of a finite thickness
LCP-rad	low conductivity plates of a finite thickness which account for the exchange of thermal radiation
PDF	probability density function
RB	Rayleigh–Bénard
RBC	Rayleigh–Bénard convection
SLP	sheet-like plumes

Another symbols

$\hat{}$	dimensional quantities
$\langle\cdot\rangle_{t,V}$	time- and volume-averaging

List of Figures

List of Tables

1

INTRODUCTION

Understanding turbulent Rayleigh–Bénard convection (RBC), i.e. the flow in a fluid layer heated from below and cooled from above, is continuously one of the fundamental problems in fluid dynamics, despite the fact that the principal mechanism behind this type of flow was discovered Before Common Era (BCE). Archimedes of Syracuse (about 250 BCE) observed that whenever the density of a body (or a fluid particle) differs from the density of the surrounding medium, the occurring buoyant force causes that body to rise, sink or remain in place depending on the difference between the buoyant force and body weight. In RBC such differences in densities are caused by spatial temperature variations. This type of fluid flow is found for example in a heated pot filled with water or in thermal convection from the human body (e.g. Nielsen et al. 2008), in rooms and cabins (e.g. Nielsen 2009), in atmospheres (e.g. Hartmann et al. 2001) and oceans (e.g. Marshall and Schott 1999), and in the outer layer of stars (Kadanoff 2001) including the Sun (Cattaneo et al. 2003).

Although numerous studies have been carried out to better understand the associated convective flow phenomena, in many of these numerical simulations the heating and cooling plates are assumed to be isothermal. This boundary condition corresponds to infinite thermal conductivity of the plates and approximates high conductivity plates, which are commonly used in RBC experiments. Alternatively, the lumped capacitance model is used in engineering applications to approximate conduction through solid bodies (Wagner 2014) whenever the assumption of homogeneous temperature inside a body is adequate.

However, these boundary conditions (BCs) lose their validity if low conductivity materials are used. This is true in many applications, such as those used in aircraft cabins (e.g. dummies), in nature (e.g. layers of the earth's surface) or even in recent RBC experiments relying on a Plexiglas sheet to separate the

working fluid from the cooling system (Kunnen et al. 2010). In such cases, a constant surface heat flux is often used to reflect the thermal conditions on the bounding surfaces of the fluid.

Although the so-called sandwich constructions, e.g. aluminium plates insulated with Styrodur, are often built in RBC experiments to ensure low level of non-homogeneity at the solid–fluid interfaces, the resulting spatial distributions of temperature and heat flux are usually non-uniform despite the fact that the plates are highly conductive. One of the reasons for this fact are perforations made in plates to hold thermometers, which are used for the measurements of the plates' temperatures (Roche et al. 2005). Experimentalists claim that the temperatures at the interfaces vary about $\pm 0.1K$ (Qiu and Tong 2001a; Du Puits et al. 2007; Maystrenko et al. 2007; Ebert et al. 2008) which can be expressed as up to 2.5% of the maximum ΔT used in these experiments. Obviously, these variations are greater when plates are made of low conductivity materials, e.g. side walls of an aircraft cabin, especially when several layers with different conductivities are considered, e.g. sophisticated passenger thermal comfort models (Konstantinov et al. 2014). When transient non-homogeneous temperature distribution occurs at the solid–fluid interface, applying simplified boundary conditions of constant temperature or constant flux may give inaccurate and thus unacceptable results. Therefore, in this study the problem of heat conduction through the solid layer of finite thickness is addressed.

Furthermore, the BCs to be investigated here allow studying the interaction of RBC and thermal radiation. While conductive and convective heat transfer between two locations depends on the first power of the temperature difference between these locations, thermal radiation between two surfaces is proportional to the difference between the fourth power of their absolute temperatures. For this reason radiative heat transfer becomes especially important, or even dominant over conduction and convection, at high absolute temperatures. Therefore, thermal radiation plays an important role in many engineering applications, such as combustion applications (fires, furnaces, rocket nozzles, engines, etc.) in nuclear reactions (such as in the sun, in a fusion reactor, or in nuclear bombs), or solar collectors.

However, thermal radiation is also important in a low temperature range, e.g. indoor flows. Simulations of heat and mass transfer in an aircraft cabin without the radiative heat transfer modelling gives non-physical results (Konstantinov et al. 2009). Moreover, thermal radiation is one of the factors that affect thermal comfort for occupants of buildings and other enclosures (aircraft and train cabins, etc.) regardless of the temperature of the enclosed fluid. Additionally, since radiation may interact with turbulent convection at the surfaces bounding the fluid, it may further affect thermal comfort by modifying the tem-

perature of these surfaces and hence the fluid temperature and flow field. This is true even if surface-to-surface radiation is considered, which implies that the fluid is radiatively non-participating.

Since in many RBC experiments side walls are made of transparent Plexiglas or polycarbonate (Daya and Ecke 2001, 2002; Qiu and Tong 2001a,b; Shang et al. 2003), radiation is transmitted through them, which eventually may affect the heat transfer inside the cell. In fact, a person sitting near a window in direct solar radiation can experience a significant heat gain (Huizenga et al. 2006). Therefore, the problem of interaction between turbulent RBC and thermal radiation assuming transparent side walls and radiatively non-participating medium is also addressed.

1.1 Temperature boundary conditions

1.1.1 Constant temperature and constant heat flux

Perusal of prior investigations by Brown et al. (2005); Hunt et al. (2003); Johnston and Doering (2009); Verzicco and Sreenivasan (2008) and Wittenberg (2010) reveals that several attempts have been made to acquire the understanding of the difference between constant temperature and constant heat flux boundary conditions.

The effect of these two boundary conditions has been recently compared by Verzicco and Sreenivasan (2008). They conducted direct numerical simulations (DNS) in a 3D cylindrical Rayleigh–Bénard (RB) cell with a constant temperature at the top and bottom plates. Alternatively, they applied a constant heat flux at the bottom plate. Their studies indicated that the heat transfer is suppressed for $Ra > 10^9$ in simulations for imposed heat flux and is closer to the one measured by Chavanne et al. (2001); Niemela et al. (2000) and Nikolaenko et al. (2005). Nevertheless, for lower Ra the results are comparable.

Moreover, 2D simulations performed by Johnston and Doering (2009) in a rectangular RB cell reveal that for $5 \times 10^6 \lesssim Ra \lesssim 10^{10}$ the Nusselt numbers obtained for constant temperature and constant heat flux BCs are very similar.

Furthermore, Stevens et al. (2010) performed a 3D DNS in a similar cylindrical cell as Verzicco and Sreenivasan (2008) and also compared their results with the experimental ones obtained by Chavanne et al. (2001) and Niemela et al. (2000). However, the comparison revealed that the Nusselt numbers obtained in simulations for the constant temperature BCs are in good agreement with those from experiments. They suggested that the observed inconsistency was due to insufficient grid resolution used in the previous studies which led to the underestimation of thermal dissipation close to the side wall, i.e. where the grid cells are the largest.

In addition to the above, Hunt et al. (2003) pointed out that temperature fluctuations occurring near the heating surface are larger when the constant heat flux is applied. Moreover, they suggested that the values of temperature fluctuations obtained for the constant temperature and constant heat flux BCs constitute respectively the lower and upper limit. Hence, the fluctuations obtained for more realistic conductive plate would lie in between these limits.

To sum up, it is desirable to better understand the consequences which arise from applying simplified BCs. Therefore, it might be fruitful to compare the results obtained for at least one of the limiting cases, e.g. the constant temperature BCs, with the more realistic BCs.

1.1.2 Spatial non-homogeneity of the plates temperature

Since understanding how the discrete heat sources affect the heat and mass transfer is important for instance in designing electronic equipment or energy efficient buildings, this subject has also received considerable attention from researchers.

Non-homogeneous heating was studied by Jaikrishna et al. (2010), who found that the distribution of the heat sources affects the temperature contours in the square cavity. Moreover, they observed that the Nusselt number is decreased for split heat sources compared to continuous heating.

A similar study was conducted by Kandaswamy et al. (2008), who studied 2D natural convection in enclosure with partially thermally active side walls developed under internal heat generation. They considered different location of heat sources, i.e. heated and cooled plates located on the side walls. They found that changing the location of these heat sources affects the number and strength of the convection rolls. Moreover, the variations of hot plate location lead to the change of the heat transfer rate. On the other hand, the variations of cold plate location do not affect the heat transfer rate. The highest heat transfer rate was obtained when the heat sources were in the middle of the side walls. Triveni et al. (2014) studied 2D natural convection in a right-angle triangular cavity filled with water. It was partially heated from the bottom and partially cooled from the left. They also noticed that changing the location of these heat sources affects the number and strength of the convection rolls. As opposed to Kandaswamy et al. (2008), they noted that the variation of the location of any plate affects the heat transfer rate.

Basak et al. (2006) and Aswatha et al. (2011) investigated the effect of different thermal boundary conditions at the hot wall on the heat transfer in a 2D cavity. They employed uniform, sinusoidal and linearly varying temperatures at the bottom wall and discovered that non-uniform heating produces greater heat transfer rates in the centre of the bottom wall than the uniform heating for the Rayleigh numbers $10^3 < Ra < 10^5$.

A theoretical analysis of convection rolls developed in the presence of the sinusoidally varying temperature imposed on the infinitely thin heated plate was performed by Freund et al. (2011). The amplitude characterising the spatial temperature modulations was approximately 0.01, and the considered forcing wavenumber was widely varying. When the latter was close to the critical wavenumber of the unforced system, the positions of the convection rolls were locked, and the strongest up-flow occurred at the maxima of the temperature modulation. Furthermore, a qualitative agreement with these theoretical predictions was found by Weiss et al. (2014), who investigated similar system experimentally.

Arguing that thermal characteristics of the plates can be responsible for the differences in results obtained in various experiments and numerical simulations, Chillà et al. (2004) proposed a model predicting whether the plate is able to maintain a constant uniform surface temperature during the development of flow structures, i.e. thermal plumes. The model estimations are based on the plates quality factor Cr that depends on the ratios of the plate to fluid conductivities, heat capacities and heights of the solid and fluid layers, as well as the Reynolds number (Re), the Prandtl number (Pr) and the aspect ratio of the cell. Since their primary aim was to explain why the ultimate regime is observed only in certain experiments, they determined the critical Cr value of 0.8 above which the plates temperature is maintained uniform, and hence the transition to the ultimate regime is evident. This model was tested by Roche et al. (2005) who conducted experiments with high and low conductivity plates for a very similar experimental setup and the operating procedure as those presented in Chillà et al. (2004). Nevertheless, they found the transition to the ultimate regime for low and high conductivity plates although the corresponding Cr was respectively lower and higher than the critical one. This finding contradicts with the model's predictions.

Although the above studies address the effects of the non-homogeneous heating, the imposed distributions of the heat sources are rather arbitrary or the results are inconsistent and require further investigations. In the present study, the temperature distributions which are developed at the solid–fluid interfaces reflect the large-scale circulations.

1.1.3 Temporal temperature and velocity fluctuations

In Rayleigh–Bénard convection, the temperature and velocity fluctuations are caused by thermal plumes or turbulent background depending on the location in the cell, e.g. in the aspect-ratio-one cell fluctuations near the wall are mainly caused by plumes, while those in bulk region - by turbulent background (Shang et al. 2003; Grossmann and Lohse 2004). Thus, the analysis of local fluctuations nicely complements global properties of turbulent convection,

such as the Nusselt number. It is also helpful in constructing and validating theories, particularly in determining the scaling behaviours.

Daya and Ecke (2001) investigated how the geometry of the container affects the fluctuation magnitudes and their scaling with the Rayleigh number. They performed simulations in cylindrical and square convection cells. The two geometrically different cells had the same height and cross sectional area and their aspect ratios were 0.7 and 0.79 for the square and cylindrical cells, respectively. They found that the fluctuations of the temperature and vertical velocity measured in the centre of the square cell are smaller than those found in the cylindrical cell. Moreover, the ratio between the fluctuations obtained in the square and cylindrical cell decreases with increasing Rayleigh numbers leading to different scaling exponents for different geometries. They also pointed out that although the local fluctuations strongly depend on geometry, global properties like the heat transport do not. Finally, they concluded that interior turbulent fluctuations are non-universal in low aspect ratio convection, which should be taken into account in turbulent convection models.

Further investigation of these authors focused on the dependency of the interior fluctuations on the Prandtl number for $2 \times 10^8 \lesssim Ra \lesssim 4 \times 10^{10}$ (Daya and Ecke 2002). Their results reveal that the rms temperature and vertical velocity fluctuations significantly decrease with Pr in contrast to the global heat transport, whose variations are very weak. Additionally, they noted that the power law scaling of the interior fluctuations proportional to $Ra^{\beta}Pr^{\gamma}$ is inadequate when β and γ are constant. Instead, the scaling exponents for the temperature fluctuations depend on the control parameters, i.e. $\beta = \beta(Pr)$, $\gamma = \gamma(Ra)$.

Measurements of the temperature fluctuations at the heating plate conducted by Gauthier and Roche (2008) in a cylindrical RB cell provide the evidence of the laminar-to-turbulent transition of the boundary layer (BL). According to Kraichnan (1962), the Nusselt number is significantly increased above a large critical Rayleigh number. This phenomenon is associated with the change of the BL from laminar to turbulent and corresponds to the so-called Kraichnan's ultimate regime of convection. Gauthier and Roche (2008) observed that the temperature fluctuations at the plates and in the bulk are similar for $Ra \lesssim 10^{12}$. On the other hand, for $2 \times Ra \gtrsim 10^{12}$ the fluctuations at the plates become increasingly greater than those in the bulk. Moreover, they discovered that the heat transfer also significantly grows with Ra above this threshold. Assuming that the fluctuations at the plates represent those in the BL, Gauthier and Roche (2008) concluded that their findings indicate the occurrence of the ultimate regime above $Ra \sim 10^{12}$.

The temporal fluctuations of the thermal boundary conditions in the buoyancy-driven flows were the subject of several numerical and experimental studies (e.g. Antohe and Lage 1996a,b; Hyun 1994). Such temperature oscillations at the fluid boundary are commonly characterised by the modulation (heating) amplitude and frequency. If the heating frequency matches the natu-

ral frequency of the flow, flow resonance occurs, which results in a maximum increase of the time-averaged heat transfer rate (Kwak and Hyun 1996).

A theoretical and numerical investigation of the effects of the heating amplitude and frequency on 2D convection was performed by Antohe and Lage (1996a). They considered a rectangular enclosure filled with water (Prandtl number $Pr = 7$) under time-periodic square wave heating in the horizontal direction. The theoretical predictions agreed well with the numerical results showing that the flow intensity and mid-plane Nusselt number increase with the heating amplitude when the heating frequency equals the resonance frequency. However, the change of heating amplitude did not affect the resonance frequency for any of the considered Rayleigh numbers, i.e. $10^7 < Ra < 10^9$.

The influence of the time-periodic boundary condition on the convective heat transfer was studied by Nithyadevi et al. (2006). They considered a square cavity with partially active vertical walls and noted that the averaged Nusselt number depends on the amplitude and period of the periodically heated plate. Furthermore, they presented the time evolution of the local Nusselt number for a certain amplitude and period showing that Nu does not considerably vary with time after the flow is established.

Lakhal et al. (1999) studied how different time variations of a partially heated side wall affect the air flow and heat transfer in a square cavity cooled from above. Comparing the results obtained for sinusoidally varying temperature with those for pulsating temperature, they noticed that the heat transfer and flow intensity are enhanced if the temperature is varied in a pulsating manner.

1.1.4 Conductive plates and walls

Since constant temperature and constant heat flux boundary conditions only approximate the infinite and finite conductivity of the solid layers, some studies on the effects of the conductive plates and walls have been carried out as well.

Lienhard (1987) considered a multi-layer system consisting of fluid and conductive layers heated from below and cooled from above. He presented an exact analytical solution of the one-dimensional convection stability problem and obtained the critical Rayleigh numbers for the case of three and four fluid layers separated by midlayers of various thickness and conductivities. Nevertheless, the solution does not account for the radiative heat transfer across the fluid layers and hence has a limited applicability.

Another theoretical study on the fluid layer bounded with conductive plates was carried out by Wittenberg (2010). He considered a Rayleigh–Bénard cell with horizontally periodic boundary conditions. The top and bottom imperfectly conductive plates were modelled by a mixed (Robin) thermal BCs with a fixed Biot number. Alternatively, they were modelled by conductive homogeneous isotropic plates of equal thickness and the same thermal properties, in

which the temperatures on the outer sides of the plates were fixed. He found that the heat transport depends on the ratio between the two other ratios - the plate to fluid thickness and conductivity. Additionally, when this ratio equals the Biot number, the bounding problems with two BCs for the Nusselt number can be successfully mapped onto one another.

Direct numerical simulations of turbulent convection coupled with heat conduction were performed by Hunt et al. (2003). They considered a rectangular box with a conductive bottom plate, an adiabatic top one and periodic BCs in the horizontal directions. Their results obtained for different ratios of the plate and fluid thermal diffusivities show that the temporal fluctuations at the solid–fluid interface increase with decreasing thermal diffusivity ratios. However, it was also found that the profiles of the mean temperature are quite insensitive to the change of the thermal diffusivity ratio.

Verzicco (2004) studied the effect of the plate difficulty to maintain a constant and uniform temperature distribution at the solid–fluid interface on the heat transfer in turbulent RBC. His investigation was based on direct numerical simulations. He pointed out that the plate finite conductivity decreases the Nusselt number not only by decreasing the temperature difference between the outer side of the plate and the solid–fluid interface, but also by modifying the plume dynamics. Moreover, based on the numerical data for the cylindrical cell of aspect ratio 0.5 Verzicco (2004) derived the empirical formula to determine the corrected Nusselt number which reduces the ideal value obtained for perfectly conductive plates. His formula, which depends on the ratio of the thermal resistance of the fluid and the plates, was later experimentally confirmed by Brown et al. (2005).

The influence of the side wall conductance on the measurements of the heat transport in turbulent RBC was studied by Ahlers (2000). He drew attention to the part of the heat, applied to the heating plate, that heats the side walls instead of the fluid. In order to estimate the correction of the measured heat transport, two models based on calculations of the two-dimensional temperature fields assuming a fixed thin and average BL thickness were considered. An analysis of several combinations of the side walls and fluid conductivities revealed that the Nu correction is high for high ratio between the conductivity of the side wall and fluid and low when this ratio is low. Moreover, the side wall effect was found to be more important near the heating and cooling plates than in the centre of the wall.

A similar investigation was performed by Roche et al. (2001). They proposed a simple model for an estimate of the side wall effect. The Nusselt number correction calculated with this model was determined by the wall number defined as the ratio of the empty cell conduction to that of the quiescent fluid. It was found to be considerably larger than the correction traditionally obtained by measuring the heat conductivity of the empty cell and subtracting it from the

one obtained under investigated flow conditions. Moreover, Roche et al. (2001) found good agreement between the performed controlled experiments and the data corrected using their model. Additionally, they suggested that the effect of conductive side walls can explain the discrepancies between the numerical and experimental results noted in the literature.

1.2 Thermal radiation

Although in many engineering applications, the coupled convection-radiation problem plays an important role, the fundamental aspects of the interaction between these two processes are still uncomprehended.

There have been only a few studies on analytical solutions for the onset of convection in a rectangular enclosure heated from below and cooled from above considering thermal radiation (such as Gille and Goody 1964; Lienhard 1990 and Hutchison and Richards 1999). Only a limited number of experiments have been conducted as well. Among them are the first laboratory experiment by Gille and Goody (1964) and the later study conducted by Hutchison and Richards (1999).

Regarding numerical simulations, considering thermal radiation is still computationally expensive despite the continuously increasing computing power. Those who eventually perform the simulations employ a series of simplifications in order to accomplish their simulations within a reasonable amount of time. The most common approach is to assume that radiation does not depend on the wavelength, and to approximate its directional nature by a diffuse emission. Nevertheless, the intensity of the irradiation still depends on the geometrical features and the thermal properties of the radiatively interacting surfaces.

Since the problems of radiative heat transfer in a participating medium are usually complex, approximate methods are often preferred. The computational aspects of different radiation models were studied by Yücel et al. (1989), who compared the discrete ordinates method with the P-1 differential approximation in terms of prediction accuracy and computational efficiency for a 2D simulation of a laminar, steady flow bounded by a square enclosure heated from the side. For certain cases they found that the P-1 approximation requires slightly less CPU time to converge. However, in comparison with the discrete ordinate method, the P-1 approximation yields higher velocities, especially in the inner core region. Another method for computing the radiative heat transfer was suggested by Lan et al. (2003), who developed a spectral method of solving the exact integral formulation of the radiative heat transfer. Aside from these approximate methods, there are many other approaches for computing the radiative heat transfer. A detailed overview of various analytical and numerical methods, including their strengths and limitations, was presented by Mishra and Prasad

(1998).

Another possibility of significantly reducing the computational effort is to perform 2D simulations. This simplification was used, for example, by Webb and Viskanta (1987), who analysed the radiation-induced natural convection in a rectangular enclosure with one transparent vertical wall and adiabatic horizontal walls. They assumed a laminar, steady flow of a semitransparent fluid and a one-dimensional radiation field. Their results show that the flow structure loses completely its centrosymmetry, especially at high Rayleigh numbers. Laminar convection and surface radiation in a square Rayleigh–Bénard cell was studied by Ridouane et al. (2004). They noticed that radiation causes a drop in the convective heat transfer, resulting in a reduced flow intensity. Moreover, their results show that the reduced momentum transport is partially compensated for by the radiative heat transfer. A further investigation by Ridouane et al. (2006) revealed that the radiative heat transfer depends mainly on the emissivity of the active walls, i.e. the heating and cooling plates, and only negligibly on the emissivity of the adiabatic walls. More recently, Gad and Balaji (2010) performed 2D simulations of the surface radiation and laminar convection in a Rayleigh–Bénard cell, to determine the critical Rayleigh number for the onset of convection. They considered a high emissivity of the heating and cooling plates (emissivity $\varepsilon = 0.85$) and adiabatic side walls maintained at emissivities between 0 and 0.85. Applying the discrete ordinates method to simulate the radiative heat transfer, they noticed that the critical Rayleigh number determining the onset of convection becomes less sensitive to the emissivity of the side walls when the cell's length to height aspect ratio increases.

With the beginning of the 21st century, three dimensional (3D) DNS of natural convection and thermal radiation became more feasible due to the development of supercomputers. Colomer et al. (2004) studied the convection and radiation in a differentially heated cavity using the discrete ordinates method, performing simulations for both transparent and participating fluids, and showing that radiation significantly increases the heat flux. Xu et al. (2007) applied the discontinuous Galerkin finite element method to simulate combined radiation and Rayleigh–Bénard–Marangoni convection in an open cylinder heated through its side wall and cooled at the top surface via radiation. They found a weak effect of internal radiation on the velocity profiles, yet a strong effect on the temperature distribution.

A parametric study of control parameters for radiation was performed by Lan et al. (2003), who employed the spectral method, which includes the exact integral formulation of radiative heat transfer, in a 3D DNS of laminar convection and radiation in a cuboidal Rayleigh–Bénard cell filled with a radiatively participating medium. They showed that the stabilising effect of the radiative heat transfer on laminar convection increases with the increasing conduction–radiation parameter or optical thickness of the fluid. Their numerical results

agreed well with the experimental data obtained for a similar configuration. Further, Xu et al. (2007) analysed the influence of the control parameters for radiation on the stability of the flow in a vertical cylinder filled with a medium with a low Prandtl number. They found that convective flows are more stable for higher fluid absorption coefficients.

1.3 Flow structures in thermal convection

Rayleigh–Bénard convection is a pattern-formation system with two coexisting coherent flow structures, i.e. the large-scale circulations (LSC) and the thermal plumes (Siggia 1994; Qiu and Tong 2001b).

The existence of the large-scale circulations was discovered by Krishnamurti and Howard (1981) by means of flow visualisation. The authors described the LSC as the largest constrained by the cell walls scale of motion that circulates due to the hot rising and cold sinking transient bubbles or plumes along with the plumes drifting in one direction near the bottom plate and in the opposite direction near the top plate.

Since the LSC carry the information, which can be used to build theoretical dependencies between the Nusselt, Reynolds, Rayleigh and Prandtl numbers, e.g. the Grossmann–Lohse theory (Grossmann and Lohse 2000), they were the subject of studies over years (e.g. Krishnamurti and Howard 1981; Xi et al. 2004; Wagner et al. 2012). Studying the geometrical features of the LSC, Niemela and Sreenivasan (2003) found that the shape of the LSC changes from elliptical to squarish when the Rayleigh number increases. Furthermore, it was found that the LSC are initiated by thermal plumes (Villermaux 1995; Sreenivasan et al. 2002; Xi et al. 2004) and in the region next to the side wall they are mainly driven by the composite plumes (Qiu and Tong 2001a) created due to the hydrodynamic attraction (Qiu and Tong 2002) or the interaction between the plumes and the surrounding them vortices (Xi et al. 2004).

In general, thermal plumes are the elongated portions of rising/falling fluid, whose temperatures are hotter/colder than the surrounding fluid. They are generated in the thermal boundary layers as the sheet-like plumes (SLP) and are ejected to the bulk at the borders between the BL and the bulk or even slightly further (Shishkina and Wagner 2006). On the other hand, the plumes in the bulk have a mushroom-like form and travel towards the opposite horizontal plate.

In order to check how the plumes are affected by changes of the dimensionless control parameters or the boundary conditions, it is necessary to identify and characterise them. Although it is relatively easy to qualitatively detect plumes in experiments or in 3D visualisations of numerical data, the quantitative identification is a challenging task.

Belmonte and Libchaber (1996) concluded that the skewness of the time

derivative of temperature characterises thermal fronts or plumes. Another selection criterion was proposed by Julien et al. (1999) who extracted the plumes by applying a threshold to the temperature, vertical velocity and vertical vorticity fields. On the other hand, Zhou and Xia (2002) used a threshold of the temperature difference and Ching et al. (2004) extracted the plumes by associating a conditionally averaged velocity with the plumes' velocity.

Having considered a cylindrical RB cell filled with water, Shishkina and Wagner (2008) proposed an approach how to extract the SLP using a temperature threshold that is defined based on the thermal dissipation rate. Additionally, they performed a detailed analysis of the extracted coherent structures - plume by plume, one by one. Their analysis revealed that SLP differ from each other in their geometrical and physical properties, such as their mean temperature, heat flux, area, diameter, etc. On the other hand, experimental studies of turbulent convection in water conducted by Zhou et al. (2007) show that the sheet-like plumes' area and their heat flux reflect log-normal distributions. The above mentioned studies suggest that although thermal plumes are unique in general, there are similarities between them.

1.4 The Nusselt number scaling

One of the fundamental quantities of interest in RBC is the global heat transport, usually expressed by the Nusselt number. In fact, for decades, series of studies have been devoted to describe how the Nusselt number scales with the parameters that define the system, i.e. the Rayleigh number, Prandtl number and aspect ratio characterising the geometry of convection cell.

One of the first research was conducted by Priestley (1954) who postulated the power law $Nu \sim \mathscr{A} Ra^{\mathscr{B}}$, where $\mathscr{B} = 1/3$, pretermitting the effect of Pr. This power law is often referred to as the 'classical scaling', which assumes that the top and the bottom BLs are independent since the heat flux does not depend on the height of the container. It also assumes that the mixing of elements does not directly depend on the thermal conductivity and kinematic viscosity.

The effect of Prandtl number was taken into account by Kraichnan (1962) who scaled the Nusselt number as $(RaPr)^{1/3}$ for $Pr < 0.1$. Moreover, he predicted that the effect of Pr, for $Pr > 0.1$, is constant for a given Ra. Hence, the power law in this region has the form of the 'classical scaling'. Furthermore, he postulated that at extremely large Ra (between $Ra = 10^{18}$ and $Ra = 10^{24}$), the BL becomes turbulent and the flow is dominated by a turbulent bulk. Therefore, in this so-called ultimate regime, the asymptotic law of heat transport is $Nu \sim \mathscr{A} Ra^{1/2}$.

Another power law was presented by Castaing et al. (1989). They investigated RBC in helium gas ($Pr \sim 1$) and showed that the power law $Nu \sim \mathscr{A} Ra^{\mathscr{B}}$, where $\mathscr{B} = 2/7$ instead of $\mathscr{B} = 1/3$, closer represents their experimental data

for $4 \times 10^7 < Ra < 6 \times 10^{12}$. Their finding was explained by the existence of the mixing zone between the BL and the bulk in which the fluid is accelerated, so that it can smoothly merge into the bulk flow. That was the backbone for the mixing zone model in which they assumed that the motion in the bulk (particularly thermal plumes) is responsible for heat transport across the cell and that it produces the so-called wind, characterised by the velocity that is parallel to the plate and stabilises the BL. This is in clear contrast to the classical theory, in which the isolated BL is self-stabilising.

The exponent 2/7 was further confirmed by many experimental and numerical studies (e.g. Wu and Libchaber 1992; Siggia 1994; Kerr 1996; Emran and Schumacher 2008). Interestingly enough, it was also confirmed by Shraiman and Siggia (1990) who reported a theoretical study assuming that buoyancy is only responsible for driving the large-scale circulations.

On the other hand, an experimental study in cylindrical RB cell filled with mercury, which corresponds to a low Prandtl number fluid ($Pr = 0.025$), performed by Cioni et al. (1997) revealed even lower scaling exponent, i.e. $\mathscr{B} = 0.2$, for $4.5 \times 10^8 < Ra < 2.1 \times 10^9$. Moreover, comparing the Nusselt number obtained in their experiment with mercury for $Ra = 10^8$ with the ones obtained by Fitzjarrald (1976); Threlfall (1975); Chillá et al. (1993) in air ($Pr \sim 0.7$), helium ($Pr = 0.8$) and water ($Pr \sim 6$) led them to support the theory of Kraichnan (1962).

In a consecutive series of papers Grossmann and Lohse (2000, 2001, 2002, 2003, 2004) developed a comprehensive scaling of the Nusselt and the Reynolds number in turbulent thermal convection. The theory behind this scaling is often referred to as the unifying theory or the Grossmann–Lohse (GL) theory and makes use of the exact relations for the global dissipation rates derived from the Boussinesq equations and BCs assuming only statistical stationarity.

Having considered the physics of the bulk as well as the BL and plumes to be fundamentally different, Grossmann and Lohse suggested to split the volume-averaged kinetic dissipation rate into the bulk and boundary layer contributions. Additionally, the volume-averaged thermal dissipation rate is split into the background and plumes with boundary layer contributions.

The theory assumes that the Reynolds number should be defined by the velocity of the large-scale wind (or LSC) which stirs the bulk and drives the turbulence there. Furthermore, the estimations of scaling relations in the bulk are derived for homogeneous isotropic turbulence. In addition, the kinetic boundary layer develops in a region adjacent to all walls in a form of a shear layer, and the thermal boundary layer is present in the vicinity of the heated and cooled surfaces. The thicknesses of these BLs are obtained from the Prandtl–Blasius theory (Prandtl 1905; Blasius 1908; Horn 2015).

The GL theory splits the *Ra*–*Pr* parameter space into four main regimes presented in the form of a phase diagram. The division is based on whether the

global dissipations are dominated by the bulk (background) contributions or BL (and plumes) contributions, and whether the thermal or kinetic BL is thicker.

Finally, the GL theory provides the accurate and approximate relations for $Nu(Ra, Pr)$ and $Re(Ra, Pr)$. The first ones are embodied by two implicit equations with free parameters obtained by fitting experimental and numerical data. On the other hand, the approximate relations are in the form of power law scalings $Nu \sim \mathscr{A} Ra^{\mathscr{B}} Pr^{\mathscr{C}}$ and account only for the dominating contributions. Thus, if data in a crossover range are examined, a superposition of the corresponding power laws should be considered. For example, for moderate Ra and $Pr \approx 1$ superposition of single power laws leads to the exponent $\mathscr{B} \approx 2/7$.

Although the Grossmann–Lohse theory is the most accepted viewpoint today, considerable differences still exist in the heat transfer obtained in different experimental and numerical setups (Stevens et al. 2011). Some of the possible reasons for these discrepancies are the variations of the Prandtl number, non-Oberbeck–Boussinesq effects, employment of constant temperature or constant heat flux BCs, non-uniform heating and cooling as well as side wall conductance and wall roughness or thermal radiation (Stevens et al. 2011). Moreover, Wagner and Shishkina (2013) showed that for small and moderate Rayleigh numbers, the Nusselt number obtained for the cylindrical cell is greater than for the box. It should be noted here that the geometrical properties of the RB cell are not included in the Grossmann–Lohse theory.

Paying a great attention to the importance of these effects, researchers devoted themselves to various experiments and numerical simulations and, in consequence, extended the available data set (Ahlers 2000; Roche et al. 2001; Verzicco 2004; Brown et al. 2005; Ahlers et al. 2009). Thanks to the joint efforts, the GL theory was recently refined by Stevens et al. (2013). They modernised the amplitude parameter of the Prandtl BL thickness. Additionally, they updated the value of dimensionless prefactors, which express the absolute size of the kinetic dissipation rates in the bulk and in the BL and of the thermal dissipation rates in the background and in the BL plus plumes. In order to determine these prefactors, experimental data were used; they were obtained for a cylindrical cell of aspect ratio one and wide range of Prandtl and Rayleigh numbers. Stevens et al. (2013) concluded that the updated prefactors significantly improved the predictions of the GL theory when comparing to several available experimental and numerical data.

Nevertheless, the more we understand the effects that influence the global heat transport, the better we can incorporate them into the further refinement of the present scaling.

1.5 Aims, objectives and outline

1.5.1 Aims

The aim of the present research is to further develop an existing DNS code (FLOWSI) in order to perform a 3D direct numerical simulations of Rayleigh–Bénard convection and surface-to-surface thermal radiation in a cuboidal enclosure with conductive active walls. The final goal is to investigate the role of radiation in the buoyancy driven flows with transient heating and cooling as well as to explore the consequences of employing simplified boundary conditions. What makes this study distinctive, is that the main area of focus is on the turbulent instead of on the laminar flow. Furthermore, the DNS solutions for 3D conduction-convection-radiation problem in long enclosures are scarce in literature.

1.5.2 Objectives

The specific objectives of the research are expressed through the following questions that shall be answered:

- How does the surface-to-surface radiation affect the bulk dynamics in the long RB cell with conductive active walls and how do these changes depend on the thermal diffusivity ratio and the Rayleigh number?
- How do the radiation-induced changes of the interface conditions affect the thermal plumes in the cuboidal RB cell with conductive active walls and how do these interface condition modifications depend on the thermal diffusivity ratio and the Rayleigh number?
- How do the convective and radiative heat fluxes contribute to the total heat transfer with respect to the changes of the thermal diffusivity ratio and the Rayleigh number?
- What are the mechanisms of the convective drop in the RB cell with low conductivity active walls and how does this drop vary in space?
- What is the correlation between the convective and radiative Nusselt number in time and space in the considered RB enclosure with low and high conductivity plates?
- How does the distribution of the radiative Nusselt number depend on the thermal diffusivity ratio?
- How do the control parameters for radiation and the Rayleigh number affect the radiative and convective Nusselt numbers as well as the effective Rayleigh number in the RB cell with low conductivity active walls?

- How do the coherent structures and the global heat transfer change with reducing the complexity level of the thermal boundary conditions?
- How can the irradiation calculations be simplified?

1.5.3 Outline

It remains to outline the structure of the work that this thesis comprises.

Chapters 2–3 provide the background information related to the topic addressed in the dissertation.

Chapter 4 presents the computational domain and numerical methodology.

Chapters 5–7 are dedicated to the effects of radiation on the bulk dynamics, interface conditions and heat transfer, respectively. There, the Rayleigh–Bénard cell is equipped with high and low conductivity plates. Moreover, the results obtained for $3.5 \times 10^5 \leqslant Ra \leqslant 6.3 \times 10^7$ in the absence of radiation are compared with these obtained in the presence of radiation for which $Nr = 0.0008$ and $\Theta = 29$. The values of the dimensionless and dimensional control parameters used in the simulations which results are shown in these chapters are collected in Table A1.

Chapter 8 shows the parametric study for the Rayleigh–Bénard convection coupled with surface-to-surface radiation in the cell with low conductivity plates. Variations of the radiation control parameters and the Rayleigh number are considered and the response of the system in terms of the radiative and convective heat transfer as well as the effective Rayleigh number is expressed in the form of scaling relations. The values of the dimensionless and dimensional control parameters used in the simulations which results are shown in this chapter are collected in Table A2.

Chapter 9 is devoted to the influence of the simplified boundary conditions on the coherent structures, accuracy of the irradiation calculations and the global heat transfer. Moreover, the simulations with different BCs which results are presented in Section 9.1 are collected in Table 9.1 and the one which results are shown in Section 9.2 is the same as that used in Section 7.3.3 of Chapters 7, i.e. see Table A1. Furthermore, the simulations used to obtain the $Nu \sim Ra$ scaling in Section 9.3 are illustrated in Figure 9.12.

Finally, the main conclusions are summarized in Chapter 10, and the details of the simulation parameters are provided in Appendix A.

2

FUNDAMENTALS OF RAYLEIGH–BÉNARD CONVECTION

2.1 Basic concept

Rayleigh–Bénard convection is a type of thermally driven flow, in which a fluid layer is heated from below and cooled from above. The exploration in this area was pioneered by Bérnard (1900), who experimentally studied the formation of convection patterns. Another pioneer of research in RBC was Rayleigh (1916), to whom we owe the theoretical description of the onset of convection. He identified the control parameter for this flow regime to be the ratio of the buoyancy force to viscous and thermal dissipation

$$Ra = \frac{\hat{\beta}\hat{g}\hat{H}^3\hat{\Delta T}}{\hat{\nu}\hat{\kappa}_f}. \tag{2.1}$$

In his honour this quantity was named Rayleigh number afterwards. There, $\hat{\beta}$ denotes the isobaric thermal expansion coefficient, and $\hat{g}$ the gravitational acceleration acting in the vertical z-direction. Further, $\hat{\Delta T}$ represents the temperature difference between the outer sides of the heating and cooling plates, and $\hat{H}$ is the height of the fluid layer, while $\hat{\nu}$ and $\hat{\kappa}_f$ stand for the kinematic viscosity and thermal diffusivity of the fluid layer, respectively.

Considering a certain fluid-filled container, increasing the temperature difference between the heating and cooling plates increases the Rayleigh number. Above the sufficiently large value, i.e. the critical Rayleigh number, the onset of convection occurs and the fluid forms quasi two-dimensional steady rolls. Further increase in the Rayleigh number results in a transition to steady three-dimensional structures and then to time-dependent flow, or directly to time-dependent flow in case of low Prandtl number fluid. This time-dependent flow

can be initially considered, to some extent, as a laminar flow (Ahlers 2009) since only further increase in the Rayleigh number causes a break of the flow structures into small scale fluctuations, such that the bulk can be considered as turbulent (Ahlers et al. 2009).

Another important parameters controlling convection are the aspect ratio determined by the geometry (i.e. the lateral extent per height of the fluid layer), and the Prandtl number

$$Pr = \frac{\hat{\nu}}{\hat{\kappa}_f}, \tag{2.2}$$

which describes the relationship between the momentum and thermal diffusivities. In other words, the Prandtl number characterises the fluid. It is very low, i.e. $Pr \ll 1$, for liquid metals and approximately 1 for gases. On the other hand, liquids have in general high Prandtl numbers, especially oils and alcohols with values as high as 10^5.

2.2 Governing equations of fluid dynamics

The equations for Rayleigh–Bénard convection are obtained from the fundamental equations governing the fluid dynamics, i.e. the continuity, Navier–Stokes and energy equations. They mathematically describe the fundamental physical principles - the conservation of mass, momentum and energy. In the following the equations are written by using index notation and Einstein summation convention.

2.2.1 Continuity equation

The conservation form of the continuity equation expressed in the form of partial differential equation is given by

$$\frac{\partial \hat{\rho}}{\partial \hat{t}} + \frac{\partial (\hat{\rho} \hat{u}_j)}{\partial \hat{x}_j} = 0. \tag{2.3}$$

Here, $\hat{\rho}$ denotes the density of the fluid element, $\hat{t}$ time, and $\hat{u}_j (j = 1,2,3 \equiv u, v, w)$ the Cartesian velocity component in the j-direction, while $\hat{x}_j (j = 1,2,3 \equiv x, y, z)$ stands for the position in the Cartesian coordinate system.

2.2.2 Navier–Stokes equations

The Navier–Stokes equations or the momentum equations are derived from the Newton's 2nd law and their conservation form reads

$$\frac{\partial (\hat{\rho} \hat{u}_i)}{\partial \hat{t}} + \frac{\partial (\hat{\rho} \hat{u}_i \hat{u}_j)}{\partial \hat{x}_j} = \frac{\partial \hat{s}_{ij}}{\partial \hat{x}_j} - \frac{\partial \hat{p}}{\partial \hat{x}_i} + \hat{f}_i. \tag{2.4}$$

Here, $\hat{f}_i$ denotes the body force acting directly on the fluid element in i-direction, $\hat{p}$ the pressure, and $\hat{s}_{ij}$ the stress in the j-direction exerted on the plane perpendicular to the i-axis.

2.2.3 Energy equation

The energy equation, which describes the first law of thermodynamics, is given by

$$\frac{\partial(\hat{\rho}\hat{E})}{\partial\hat{t}} + \frac{\partial(\hat{\rho}\hat{E}\hat{u}_j)}{\partial\hat{x}_j} = \frac{\partial\hat{u}_i\hat{s}_{ij}}{\partial\hat{x}_j} - \frac{\partial\hat{u}_j\hat{p}}{\partial\hat{x}_j} + \hat{f}_i\hat{u}_i + \hat{\kappa}_f\frac{\partial^2\hat{T}}{\partial\hat{x}_j^2} + \hat{\rho}\hat{q}, \tag{2.5}$$

where $\hat{q}$ denotes the rate of volumetric heating due to absorption of thermal radiation, and $\hat{T}$ the temperature, while $\hat{E}$ stands for the total energy of a moving fluid per unit mass, which is the sum of its internal and kinetic energy.

2.2.4 Modelling of Rayleigh–Bénard convection

Since Rayleigh–Bénard convection is a buoyancy-driven flow, the external force in (2.4) is the buoyancy force

$$\hat{f}_i = -\hat{\rho}\hat{g}\hat{\delta}_{zi} \tag{2.6}$$

acting vertically as indicated by the Kronecker symbol δ_{zi}. Moreover, the governing equations for Rayleigh–Bénard convection are obtained by applying the so-called Oberbeck–Boussinesq approximation to the general form of the governing equations. This approximation implies that the density in (2.6) linearly depends on temperature

$$\hat{\rho}(\hat{T}) = \hat{\rho}(\hat{T}_0)\left(1 - \hat{\beta}(\hat{T} - \hat{T}_0)\right). \tag{2.7}$$

Here, $\hat{T}_0$ is the reference temperature, i.e. the mean bulk temperature. In any other terms of the governing equations, the density as well as all the other material properties, i.e. viscosity, thermal conductivity and specific heat capacity, are constant. Obviously, the latter assumption is valid only when the variations of the thermophysical properties due to temperature and pressure differences are relatively small. According to Gray and Giorgini (1976) the Oberbeck–Boussinesq approximation is applicable when the certain factors, calculated from the thermophysical properties of the fluid with respect to $\hat{T}_0$, are smaller than the requested accuracy. Considering air, which is investigated in the present study, the most restrictive factors are

$$\begin{aligned} F_1 &= \hat{\beta}_{\hat{T}_0}\Delta\hat{T}, \\ F_2 &= \hat{B}_{\hat{T}_0}\hat{\rho}_{\hat{T}_0}\hat{g}\hat{H}, \\ F_3 &= \frac{\hat{\beta}_{\hat{T}_0}\hat{g}\hat{T}_0}{\hat{c}_{p,\hat{T}_0}}\frac{\hat{H}}{\Delta\hat{T}}, \end{aligned} \tag{2.8}$$

where $\hat{B}_{\hat{T}_0}$ is the isothermal bulk modulus and $\hat{c}_{p,\hat{T}_0}$ the specific heat capacity evaluated at $\hat{T}_0$. Furthermore, for $\hat{T}_0 = 40^\circ C$ and the accuracy of 0.1 that was proposed by Gray and Giorgini (1976), the Oberbeck–Boussinesq approximation holds if $\hat{\Delta T} \lesssim 31$ K and $\hat{H} \lesssim 10\hat{\Delta T}$ m/K.

Besides the Oberbeck–Boussinesq approximation, the fluid is considered to be Newtonian, i.e. shear stress is proportional to the velocity gradient, which is the case for most fluids in engineering and especially for air that is investigated in this study.

2.2.5 Dimensionless equations

The considered governing equations, i.e. (2.3)–(2.5), together with the above assumptions are non-dimensionalised using

$$x_i = \frac{\hat{x}_i}{\hat{H}}, \qquad T = \frac{\hat{T} - \hat{T}_0}{\hat{\Delta T}}, \qquad u_i = \frac{\hat{u}_i}{\hat{u}_0}, \qquad p = \frac{\hat{p}}{\hat{\rho}\hat{u}_0^2}, \qquad t = \frac{\hat{t}\hat{u}_0}{\hat{H}}, \tag{2.9}$$

where $\hat{u}_0 = (\hat{\beta}\hat{g}\hat{\Delta T}\hat{H})^{1/2}$ is the buoyant velocity, and $\hat{T}_0$ stands for the mean bulk temperature. The dimensional quantities are denoted with a $\hat{\cdot}$, and the dimensionless, without one.

Finally, the dimensionless form of the governing equations for Rayleigh–Bénard convection is given by

$$\frac{\partial u_j}{\partial x_j} = 0, \tag{2.10}$$

$$\frac{\partial u_i}{\partial t} + u_j\frac{\partial u_i}{\partial x_j} = \nu\frac{\partial^2 u_i}{\partial x_j^2} - \frac{\partial p}{\partial x_i} + T\delta_{zi}, \tag{2.11}$$

$$\frac{\partial T}{\partial t} + u_j\frac{\partial T}{\partial x_j} = \kappa_f\frac{\partial^2 T}{\partial x_j^2}. \tag{2.12}$$

The non-dimensional kinematic viscosity and thermal diffusivity of the fluid are defined by

$$\nu = \left(\frac{Pr}{Ra}\right)^{1/2} \quad \text{and} \tag{2.13}$$

$$\kappa_f = \frac{1}{(RaPr)^{1/2}}, \tag{2.14}$$

respectively.

Besides solving the governing equations for the fluid, i.e. (2.10)–(2.12), the heat transfer through the solid plates is computed by solving the dimensionless

conduction equation

$$\frac{\partial T}{\partial t} = \kappa_s \frac{\partial^2 T}{\partial x_j^2}, \tag{2.15}$$

where κ_s is the dimensionless thermal diffusivity of the considered material of the solid plates

$$\kappa_s = \frac{1}{(RaPr)^{1/2}} \frac{\hat{\kappa}_s}{\hat{\kappa}_f}. \tag{2.16}$$

The ratio of the thermal diffusivities of the solid and fluid layers $\lambda_\kappa = \hat{\kappa}_s/\hat{\kappa}_f$ is an additional control parameter that controls the diffusion and has to be specified as an input parameter when solid plates are employed.

2.3 Effective numbers

When the Rayleigh–Bénard cell is equipped with infinitely thin horizontal plates, the flow quantities which incorporate the temperature or velocity are non-dimensionalised with respect to the temperature difference between the isothermal plates, i.e. $\Delta\hat{T}$. This temperature difference is related to the height of the fluid layer $\hat{H}$, as sketched in Figure 2.1a.

On the other hand, when solid plates are employed, the temperature difference between the solid–fluid interfaces, which is related to the height of the fluid layer, is not known *a priori*. Therefore, the only possible choice of the reference temperature difference is the temperature difference between the outer side of the solid plates, where the temperature is fixed. However, although that temperature difference is still denoted as $\Delta\hat{T}$, it is related to the total height of the cell, i.e. $\hat{H} + 2\hat{h}_s$. The latter is depicted in Figure 2.1b. Such normalisation is used in Chapter 5–8, where the radiation effects on the entire system are examined.

Furthermore, when the influence of various boundary conditions on the development of thermal plumes is investigated in Chapter 9, the effective temperature difference

$$\Delta T_{eff} = \langle T \rangle_{t,S_{z=1}} - \langle T \rangle_{t,S_{z=0}}, \tag{2.17}$$

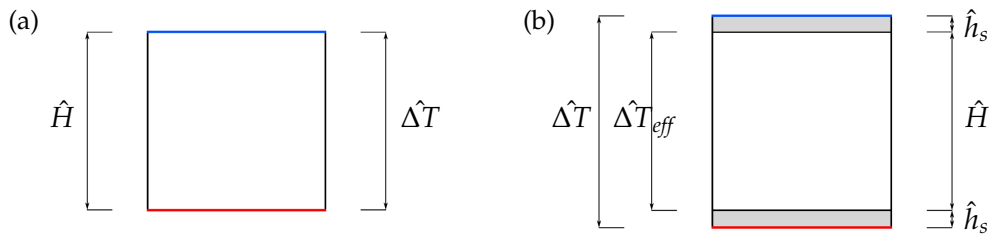

FIGURE 2.1: Sketch of the reference height and temperature difference for the Rayleigh–Bénard cell equipped with the infinitely thin plates (a) and the solid plates (b).

is calculated from the time-averaged temperature fields and used to obtain the effective Rayleigh number

$$Ra_{\mathit{eff}} = Ra\frac{\Delta T_{\mathit{eff}}}{\Delta T}, \tag{2.18}$$

as well as the effective temperature

$$T_{\mathit{eff}} = T\frac{\Delta T}{\Delta T_{\mathit{eff}}} \tag{2.19}$$

and the effective convective Nusselt number

$$Nu_{c,\mathit{eff}} = Nu_c\frac{\Delta T}{\Delta T_{\mathit{eff}}}. \tag{2.20}$$

The effective temperature difference is depicted in Figure 2.1b for clarity.

In (2.17) and in the following, $\langle\cdot\rangle_t$ denotes averaging in time and $\langle\cdot\rangle_{S_z}$ area-averaging over an (x, y)-plane S_z at distance z from the bottom solid–fluid interface. Besides, $\langle\cdot\rangle_y$ denotes line-averaging in the y-direction and $\langle\cdot\rangle_V$ averaging over the entire volume of the cell.

3

FUNDAMENTALS OF THERMAL RADIATION

3.1 Theoretical description

Thermal radiation is a form of energy transfer, which, in contrast to conduction and convection, does not require any matter to take place. According to the electromagnetic wave theory postulated by Maxwell (1863) and demonstrated by Hertz (1887), thermal radiation is an electromagnetic wave which is formed by the vibrations of electric and magnetic fields. In other words, a changing magnetic field causes a changing electric field and vice-versa. These two fields can couple together and form an electromagnetic wave which propagates at the speed of light. On the other hand, from the standpoint of quantum theory introduced by Planck (1900), thermal radiation may be viewed as a propagation of massless energy packets, called photons or quanta.

The electromagnetic waves can be characterised by energy, frequency or wavelength, which are all mathematically related. Such descriptions allow to distinguish different types of electromagnetic radiation: electrical power waves, radio- and microwaves, infrared, visible and ultraviolet rays, as well as X-, gamma- and cosmic-rays. Concerning the wavelength of oscillations, which is the distance between the wave's crests, the latter rays have the wavelength below 10^{-7} micrometers, and the spectrum of electrical power waves starts above 10^{10} micrometers.

Since the most heat is transferred by ultraviolet, visible and infrared radiation, only these three are considered in this study. They all are commonly called thermal radiation, which wavelength ranges from 10^{-2} to 10^{2} micrometers. Interestingly, the radiation emitted by the sun is in half a visible light and the remaining part belongs to ultraviolet and infrared. Moreover, every matter which temperature is above zero Kelvin emits thermal radiation, and bodies at room

temperature such as walls, furniture and humans emit infrared radiation.

3.2 Emissive power

The emissive power of a surface is a thermal energy emitted by a unit area. The model, which approximates such emission was proposed by Stefan (1879) who found the exponential relation between the radiative heat emission and temperature by analysing the existing experimental data. His formula was afterwards confirmed by Boltzmann (1884), who performed a theoretical derivation based on the thermodynamic considerations. Nowadays, this model is known as the Stefan–Boltzmann law

$$\hat{\hat{q}}_i^e = \hat{\sigma}\hat{T}_i^4, \tag{3.1}$$

where $\hat{\hat{q}}_i^e$ denotes the emissive power of a surface element i in W/m^2, $\hat{T}_i$ the absolute temperature in Kelvin, and $\hat{\sigma} = 5.67 \times 10^{-8}$ the Stefan–Boltzmann constant in $W/m^2 \cdot K^4$. It expresses the upper limit of the emissive power, which is reserved for a perfect emitter and absorber of radiation, i.e. a blackbody. This idealized body emits radiation uniformly in all directions over all wavelengths, and it serves as a reference from which the radiative properties of a real surface may be calculated.

When it comes to a real surface, its material and condition determine whether the emission of radiation is mainly directional or nearly diffuse, i.e. having the same intensity in all directions. These two parameters also determine the fraction of the maximum emissive power emitted by a surface, which is called the emissivity ε. Moreover, the surface temperature determines the emission of a specific wavelength. For example, bodies at low temperature, i.e. $\hat{T} \leqslant 800K$, emit almost only infrared radiation and these at higher temperatures emit larger fraction of short wavelengths. Furthermore, a surface is said to be gray if its properties are independent of wavelength.

3.3 Interactions between photons, surfaces and media

Since everything at temperature above absolute zero emits radiation, every body is bombarded by the incoming radiation. The conservation of energy implies that radiation which reaches the surface must be either absorbed, reflected or transmitted. When it comes to absorption the general physics behind this process is viewed as the excitement of electrons from a lower to a higher energy level due to incoming quantum of energy. The radiation property characterising the ability of the surface to absorb the incoming radiation is called the absorptivity α. Moreover, since it is a fraction of the total incoming radiation, its value lies between zero and one. The other radiation properties characterising the ability

of the surface to reflect and transmit the incoming radiation are the reflectivity ϱ and the transmissivity τ, respectively, and their values also range between zero and one. Furthermore, with respect to the first law of thermodynamics,

$$\alpha + \varrho + \tau = 1. \tag{3.2}$$

Considering a semitransparent solid body or the entire volume of medium which reflect, absorb and transmit radiation, such radiation process is considered to be a volumetric phenomenon. Consequently, simulating such radiative heat exchange involves solving a complex radiation transfer equation (Collins 1989).

However, when a transparent fluid that is radiatively non-participating, i.e. neither emits, absorbs, nor scatters, is confined by blackbody walls which are known not to reflect radiation, i.e. $\varrho = 0$, nor transmit one, i.e. $\tau = 0$, the radiative heat transfer is a surface phenomenon for such a system. Then, the total energy transferred by means of radiation from a surface element i to a surface element j expressed in W is

$$\hat{q}^{ir}_{i\to j} = \hat{A}_i \hat{q}^{e}_{i} F_{ij}, \tag{3.3}$$

where $\hat{A}_i$ is the area of the surface element i and F_{ij} the view factor. Then, the radiative heat flux incoming on the surface element j of the area $\hat{A}_j$, or simply irradiation, expressed in W/m^2 yields

$$\hat{\hat{q}}^{ir}_{i\to j} = \hat{q}^{ir}_{i\to j}/\hat{A}_j. \tag{3.4}$$

3.4 Concept of a view factor

The radiative heat transfer between surfaces depends on the geometry of these surfaces and their orientation relative to each other as well as their radiative properties and temperatures. The view factor, also known as the shape factor or the configuration factor, accounts for the geometry and orientation of surfaces including the distance between them, and is completely independent of the surface properties and temperature.

The view factor from the surface element i to the surface element j is denoted as F_{ij} and defined as a fraction of radiation leaving the surface element i that is intercepted by the surface element j. For the complete derivation of F_{ij} the reader is referred to Incropera et al. (2011).

Finally, for the isothermal surface element i that emits and reflects radiation diffusely and is separated from the surface element j by the radiatively non-participating medium, the view factor determined in the far field approximation

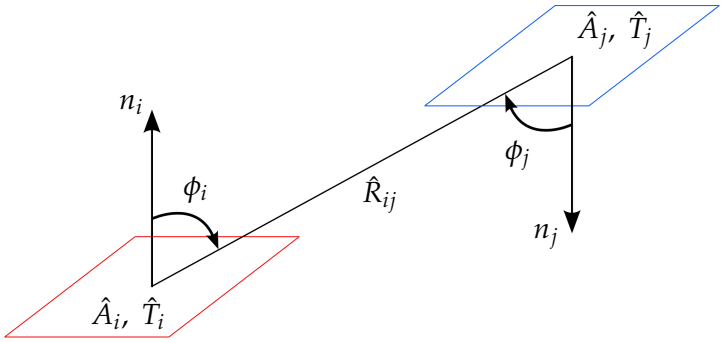

FIGURE 3.1: The concept of the view factor F_{ij} associated with radiative heat transfer from the surface element i to the surface element j and determined by the polar angles ϕ_i and ϕ_j between the line of sight $\hat{R}_{ij}$ and the surface normals n_i and n_j. Note that, $\hat{A}_i$ and $\hat{A}_j$ are the areas of two arbitrarily oriented surface elements.

is given by

$$F_{ij} = \hat{A}_j \frac{\cos\phi_i \cos\phi_j}{\pi \hat{R}_{ij}^2}. \tag{3.5}$$

Here, the polar angles ϕ_i and ϕ_j are formed by the lines of sight between the centres of the surface elements i and j and the surface normals n_i and n_j, respectively, as depicted in Figure 3.1. Then, $\hat{R}_{ij}$ denotes the distance between two arbitrarily oriented surface elements i and j.

Analogously, the view factor F_{ji} defines the fraction of radiation leaving the surface element j that strikes the surface element i. Moreover, F_{ji} as well as F_{ij} are dimensionless quantities which are bounded by zero and one.

Performing the radiation analysis on the enclosure consisting of N surface elements requires the evaluation of N^2 view factors, which is a very time consuming process. However, it is possible to reduce the number of view factors that have to be calculated by utilizing some fundamental relations. The first dependency between the view factors which is utilized in this study is the reciprocity relation

$$\hat{A}_j F_{ji} = \hat{A}_i F_{ij}. \tag{3.6}$$

It allows to determine the counterpart of a view factor from a knowledge of the view factor itself and the areas of the two surface elements.

Another relation, which is applied in this study thanks to the symmetrical geometry, is the symmetry rule. It is applicable if two (or more) identical surface elements i and j possess symmetry about the third surface element k. Then, the view factor

$$F_{ki} = F_{kj}. \tag{3.7}$$

Another useful relation for view factors is the summation rule

$$\sum_{j=1}^{N} F_{ij} = 1, \tag{3.8}$$

which is based on the conservation requirement that entire radiation leaving a surface element i has to reach all the surface elements of the enclosure that interact radiatively with the surface element i.

4

NUMERICAL SETUP AND APPROACH

The code named FLOWSI is used to simulate the flow by means of direct numerical simulations (DNS). This code was originally developed by Schmitt and Friedrich (1982); Schmitt et al. (1986) and further modified by Unger who introduced the cylindrical coordinates and applied modification with respect to the singularity at the pipe axis (Unger 1994). In Wagner et al. (1994) FLOWSI was advanced to simulate Rayleigh–Bénard convection in cylindrical enclosures. Further changes done by Wagner (1996); Shishkina and Wagner (2007b) and Shishkina et al. (2009) included the development of a forth-order finite volume method in cylindrical and rectangular enclosures for non-equidistant meshes dedicated especially to turbulent Rayleigh–Bénard convection. The Neumann stability was analysed for the leapfrog–Euler scheme for solving the convection-diffusion equation by Shishkina and Wagner (2004). Last but not least Kaczorowski et al. (2008) developed and implemented the scheme of separation of variables within the Poisson solver for the rectangular domain and non-equidistant meshes. The code parallelisation was performed by Kaczorowski (2009).

For the purpose of this study, the code is further developed to cope with the finite thickness of the solid plates and surface-to-surface radiation. Since the discretization methods were described in detail by the previous FLOWSI developers, only a brief look is provided in Section 4.2. On the other hand, a closer look at the boundary conditions (Section 4.4), the latest criteria for resolution requirements (Section 4.7) and the optimisation of radiation calculations (Section 4.9) is taken.

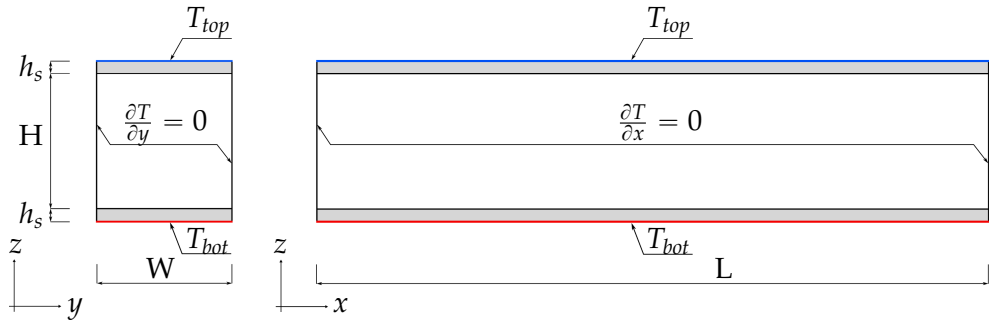

FIGURE 4.1: Side views of the geometry of the convection cell with the temperature boundary conditions.

4.1 Computational domain

The geometry used in this study is shown in Figure 4.1. The DNS are conducted for a cuboidal domain of length $\hat{L} = 5\hat{H}$ and aspect ratio $\Gamma = \hat{W}/\hat{H} = 1$, where $\hat{W}$ and $\hat{H}$ are the width and height of the enclosed fluid, respectively. Further, the non-dimensional length, width and height are $L = 5$, $W = 1$ and $H = 1$, respectively. Moreover, the height of the infinitely thin plates (ITP) is zero, i.e. $h_s = 0$. On the other hand, when solid plates of a finite thickness are employed, their thickness represents the height of the heating and cooling system often used by experimentalists and equals $h_s = 0.065H$.

4.2 Discretization

Spatial discretization.
The incompressible Navier–Stokes equations are discretized following the volume balance procedure by Schumann (1973). The approach involves staggered Cartesian grids, where the scalar variables, i.e. temperature and pressure, are stored in the cell centres of the control volume, whereas the velocity components and momentum variables are located at the cell faces. The divergence theorem is applied to reduce the volume-averaged convective and diffusive terms obtained from volume integration of the differential form of the Navier–Stokes equation to surface integrals in the corresponding finite-volume equation. Moreover, a fourth order polynomial scheme constructed as in Shishkina and Wagner (2007a) is used to approximate any value not defined at the required position.

Time discretization.
The convective terms, i.e. $u_j \partial u_i / \partial x_j$ and $u_j \partial T / \partial x_j$, are discretized with respect to time by using the Leapfrog explicit scheme. On the other hand, for the diffusive

terms, i.e. $\partial^2 u_i/\partial {x_j}^2$ and $\partial^2 T/\partial {x_j}^2$, the Euler-forward explicit scheme is used. Thus, the momentum equation is given by

$$\frac{\mathbf{u}^{n+1} - \mathbf{u}^{n-1}}{2\Delta t} + \mathbf{u}^n \cdot \nabla \mathbf{u}^n + \nabla p^n \quad = \quad \nu \Delta \mathbf{u}^{n-1} + T^n \mathbf{e}_z \tag{4.1}$$

using a second order time accurate explicit leapfrog-Euler scheme, where the subscript n denotes the discrete time level. In general, explicit schemes provide a solution faster than implicit schemes, yet in the case of explicit schemes a smaller time step Δt is required due to numerical stability. In the present study, the time step

$$\Delta t < \left(\frac{3}{2} \sum_{i=1}^{3} \frac{u_i}{\Delta x_i} + \frac{16\nu}{3} \sum_{i=1}^{3} \frac{1}{\Delta x_i^2} \right)^{-1} \tag{4.2}$$

satisfies the von Neumann stability of the leapfrog-Euler scheme (see Shishkina and Wagner 2004). Moreover, since the von Neumann analysis is in principle relevant to linear problems, the time step estimated from (4.2) is multiplied by a safety factor 0.25 in order to avoid nonlinear instabilities.

For more details on the numerical schemes, see Shishkina and Wagner (2007b). Finally, since the spatial and temporal discretizations are of fourth and second order accuracy, respectively, the total order of the solution of the NS equation is determined as in Feldmann and Wagner (2012). In brief, since the time step estimated from (4.2) is proportional to the squared mean mesh, i.e. $\Delta t \propto \Delta x_i^2$, and is around two orders of magnitude smaller than the Kolmogorov time scale for the performed DNS, the final solution is eventually of order four.

Poisson solver.
The pressure–velocity coupling is realised with the help of the Chorin projection method, which is based on the Helmholtz–Hodge decomposition (Chorin 1968). The Poisson equation that arises is decoupled in the y-direction, applying the separation of variables method discussed in detail in Kaczorowski et al. (2008). The remaining linear systems are solved using a 2D cyclic reduction algorithm, which is available as part of the FISHPACK package (Swarztrauber 1974; Swarztrauber and Sweet 1975).

4.3 Radiative properties

In this study, the heat reaching the side walls by radiation is completely transmitted to the surroundings (transmissivity $\tau = 1$). This heat loss is compensated for by the entering radiation, which is determined by the constant temperature outside the cell, $\hat{T}_{out}$. The latter is assumed to equal the mean bulk

temperature, i.e. $\hat{T}_{out} = \hat{T}_0$. These conditions are representative for a Rayleigh–Bénard cell with e.g. Plexiglas side walls used frequently by experimentalists to allow optical measurements, standing in a laboratory room, which temperature T_{out} is maintained constant.

The medium considered in the simulations is dry air that is CO_2 free. Since these molecules are the only asymmetrical molecules that absorb radiation of certain wavelengths in air (Lienhard IV and Lienhard V 2008), it is assumed that the medium is radiatively non-participating. Thus, radiation is a surface phenomenon. The latter is particularly true since the distance between the surfaces is less than a few meters (Lienhard IV and Lienhard V 2008).

In order to capture the maximal effects of radiative heat exchange between radiatively participating surfaces, the surfaces emit and absorb radiation as a blackbody (diffuse and wavelength independent emission for which emissivity $\varepsilon = 1$; absorptivity $\alpha = 1$). These surfaces may represent e.g. any real surfaces painted with Carbon Black Paint NS-7 for which absorption coefficient is very close to one (Pompea and Breault 2004). On the other hand, the minimal effects of surface-to-surface radiation are observed for the minimal emission (emissivity $\varepsilon = 0$). The latter reflects the absence of radiation.

4.4 Boundary conditions

No-slip and impermeability conditions are applied at all solid walls. Therefore, all velocity components vanish at the walls, i.e. $u_i|_{x\in\{0,5\}} = u_i|_{y\cap z\in\{0,1\}} = 0$. Adiabatic lateral walls are realised by applying a zero temperature gradients normal to the walls, i.e. $\partial T/\partial x|_{x\in\{0,5\}} = \partial T/\partial y|_{y\in\{0,1\}} = 0$, what is illustrated in Figure 4.1. Furthermore, the Poisson equation is solved for the pressure with a zero pressure gradient normal to the walls, i.e. $\partial p/\partial x|_{x\in\{0,5\}} = \partial p/\partial y|_{y\in\{0,1\}} = \partial p/\partial z|_{z\in\{0,1\}} = 0$.

When solid plates are employed, i.e. $h_s \neq 0$, the temperatures $T_{bot} = +0.5$ and $T_{top} = -0.5$ are fixed at the outer side of the heating and cooling plate, and the temperatures at the solid–fluid interfaces are calculated according to the interface conditions described in Section 4.5.1 and 4.5.2. When $h_s = 0$, the temperature at the heating and cooling plate does not change in time. Thus, in the case of a homogeneous temperature distribution, the temperature at the bottom and the top horizontal bounding wall equals $T_{bot} = +0.5$ and $T_{top} = -0.5$, respectively. However, when non-homogeneous BCs are applied, the needed temperature distributions are obtained by time-averaging the temperature at the corresponding interface of the low conductivity plates such that the area-averaged temperature at the bottom and top interface equals $T_{bot} = +0.5$ and $T_{top} = -0.5$, respectively.

4.5 Interface conditions

4.5.1 Interface conditions for simulations without radiation modelling

Every time step, the temperature at the interface is obtained from the interface conditions (ICs) that satisfy equal heat flux at both sides of the interface. The sketch in Figure 4.2 shows the components of the heat flux at the bottom and top interface, and the arrows visualise the direction of the heat transfer. The mathematical formulation of the interface conditions can be written in the following form

$$\hat{q}^{cond} = \hat{q}^{diff}. \tag{4.3}$$

The conductive heat flux $\hat{q}^{cond}$ is calculated based on the Fourier law

$$\hat{q}^{cond} = -\hat{k}_s \frac{\partial \hat{T}}{\partial \hat{z}}, \tag{4.4}$$

where $\hat{k}_s$ is the thermal conductivity of the solid plates. The diffusive heat flux $\hat{q}^{diff}$ is calculated also based on the Fourier law, yet the thermal conductivity of the solid plates is replaced by the one of the fluid layer, i.e. $\hat{k}_f$.

When highly conductive plates are considered, the ratio between the thermal conductivity of the solid and the fluid layer equals $\hat{k}_s/\hat{k}_f = 9480$, which corresponds to aluminium (VDI-Gesellschaft Verfahrenstechnik und Chemieingenieurwesen and others 2010). In the case of low conductivity plates, $\hat{k}_s/\hat{k}_f = 7.6$, which corresponds to such materials as Plexiglas, Elastollan or Stimulite, from which the two latter ones are widely used in aircraft seats (Atofina Chemicals, Inc. 2000; BASF SE 2011, 2013). Additionally, the ratio between the thermal diffusivity of the solid and the fluid layer, which is used in the energy equation, equals $\hat{\kappa}_s/\hat{\kappa}_f = 3.8$ and $\hat{\kappa}_s/\hat{\kappa}_f = 0.0034$ for the high and low conductivity plates, respectively.

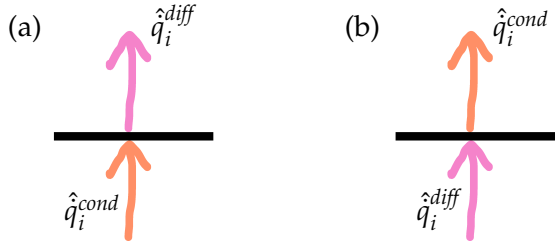

FIGURE 4.2: Heat flux decomposition at the bottom interface (a) and at the top interface (b) in the absence of radiation.

4.5.2 Interface conditions for simulations with radiation modelling

The temperature at the interface is obtained in a similar way as in the absence of radiation, i.e. to satisfy constant heat flux at both sides of the interface. However, in the presence of radiation, additional heat flux components take part in the energy transfer. Moreover, the energy balance at the bottom interface differs from the one at the top interface, and thus the interface conditions at the bottom and top interface are discussed separately. Nevertheless, the detailed derivation is shown only for the interface conditions at the bottom interface. The ICs at the top interface are derived by analogy with the ones at the bottom interface, and hence only the main equations are shown.

Note that since the medium is transparent to radiation, radiation can only interact with the medium by heating or cooling surfaces bounding the fluid (Incropera et al. 2011). Thus, the radiation model is included only to the interface conditions.

Interface conditions at the bottom interface.
The sketch in Figure 4.3 shows the components of the heat flux at a surface element i located at the bottom interface, and the arrows visualise the incoming and outcoming energy. Furthermore, the mathematical form reads

$$\hat{q}_i^{cond} + \sum_{sw=1}^{N} \hat{q}_{sw\to i}^{ir} + \sum_{j=1}^{N} \hat{q}_{j\to i}^{ir} = \hat{q}_i^{e} + \hat{q}_i^{diff} \tag{4.5}$$

and each of its terms is explained below.

The conductive heat flux calculated at the solid side of a surface element i, i.e. $\hat{q}_i^{cond}$, and the diffusive heat flux calculated at the fluid side of a surface element i, i.e. $\hat{q}_i^{diff}$, are determined with the Fourier law according to (4.4).

The total emissive power of a surface element i, i.e. $\hat{q}_i^{e}$, is expressed by the Stefan–Boltzmann law which is recalled here from Section 3.2 of Chapter 3 for clarity. It is

$$\hat{q}_i^{e} = \hat{\sigma}\hat{T}_i^4. \tag{4.6}$$

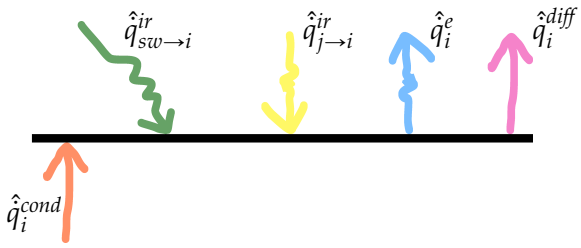

FIGURE 4.3: Heat flux decomposition at the bottom interface in the presence of radiation.

The irradiation originating from a surface element j located at the top interface, i.e. $\hat{\dot{q}}^{ir}_{j\to i}$, is evaluated from the rate of radiant energy leaving a surface element j of an area $\hat{A}_j$

$$\hat{q}^{e}_{j} = \hat{A}_j \hat{\sigma} \hat{T}^4_j \tag{4.7}$$

by calculating the fraction of the radiant energy that is intercepted by a surface element i of an area $\hat{A}_i$, located at the bottom interface

$$\hat{A}_i \hat{\dot{q}}^{ir}_{j\to i} = \hat{A}_j \hat{\sigma} \hat{T}^4_j F_{ji}. \tag{4.8}$$

For the sake of clarity, the view factor

$$F_{ji} = \hat{A}_i \frac{\cos\phi_i \cos\phi_j}{\pi \hat{R}^2_{ij}} \tag{4.9}$$

is recalled from Section 3.4 of Chapter 3.

The irradiation originating from the ambient environment which passes through the transparent side walls, i.e. $\hat{\dot{q}}^{ir}_{sw\to i}$, is evaluated in a similar way as the irradiation originating from the top interface, and hence

$$\hat{A}_i \hat{\dot{q}}^{ir}_{sw\to i} = \hat{A}_{out} \hat{\sigma} \hat{T}^4_{out} F_{sw\to i}. \tag{4.10}$$

Following the assumption of fully transparent side walls, constant temperature of the ambient environment $\hat{T}_{out}$ and constant surface area $\hat{A}_{out}$ that corresponds to this temperature, the total irradiation originating from the ambient environment is

$$\hat{A}_i \sum_{sw=1}^{N} \hat{\dot{q}}^{ir}_{sw\to i} = \hat{A}_{out} \hat{\sigma} \hat{T}^4_{out} \sum_{sw=1}^{N} F_{sw\to i}. \tag{4.11}$$

Utilising the reciprocity relation

$$\hat{A}_{out} \sum_{sw=1}^{N} F_{sw\to i} = \hat{A}_i \sum_{sw=1}^{N} F_{i\to sw} \tag{4.12}$$

and the summation rule

$$\sum_{j=1}^{N} F_{ij} + \sum_{sw=1}^{N} F_{i\to sw} = 1 \tag{4.13}$$

the dependencies between the view factors are built. Substituting (4.12) and (4.13) in (4.11) one obtains

$$\hat{A}_i \sum_{sw=1}^{N} \hat{\dot{q}}^{ir}_{sw\to i} = \hat{A}_i \hat{\sigma} \hat{T}^4_{out} \left(1 - \sum_{j=1}^{N} F_{ij} \right), \tag{4.14}$$

where the view factor

$$F_{ij} = \hat{A}_j \frac{\cos\phi_i \cos\phi_j}{\pi \hat{R}_{ij}^2}. \tag{4.15}$$

With the help of equations (4.4), (4.6), (4.8), (4.9), (4.14), (4.15), equation (4.5) can be expanded to the following

$$\overbrace{-\hat{k}_s \frac{\partial \hat{T}}{\partial \hat{z}}\bigg|_i^s}^{\hat{q}_i^{cond}} + \overbrace{\hat{\sigma}\hat{T}_{out}^4 \left(1 - \sum_{j=1}^{N} \hat{A}_j \frac{\cos\phi_i \cos\phi_j}{\pi \hat{R}_{ij}^2}\right)}^{\sum_{sw=1}^{N} \hat{q}_{sw\to i}^{ir}} + \overbrace{\sum_{j=1}^{N} \hat{\sigma}\hat{T}_j^4 \hat{A}_j \frac{\cos\phi_i \cos\phi_j}{\pi \hat{R}_{ij}^2}}^{\sum_{j=1}^{N} \hat{q}_{j\to i}^{ir}} = \tag{4.16}$$

$$\underbrace{\hat{\sigma}\hat{T}_i^4}_{\hat{q}_i^e} \quad \underbrace{-\hat{k}_f \frac{\partial \hat{T}}{\partial \hat{z}}\bigg|_i^f}_{\hat{q}_i^{diff}}.$$

Nondimensionalization of (4.16) is carried out using the non-dimensional variables from (2.9) yielding

$$\hat{k}_s \frac{\partial\left(T\hat{\Delta T} + \hat{T}_0\right)}{\partial\left(z\hat{H}\right)}\bigg|_i^s - \hat{k}_f \frac{\partial\left(T\hat{\Delta T} + \hat{T}_0\right)}{\partial\left(z\hat{H}\right)}\bigg|_i^f + \hat{\sigma}\left(T_i\hat{\Delta T} + \hat{T}_0\right)^4 = \tag{4.17}$$

$$\hat{\sigma}\sum_{j=1}^{N} A_j\left(T_j\hat{\Delta T} + \hat{T}_0\right)^4 \frac{\cos\phi_i \cos\phi_j}{\pi R_{ij}^2} + \hat{\sigma}\left(T_{out}\hat{\Delta T} + \hat{T}_0\right)^4 \left(1 - \sum_{j=1}^{N} A_j \frac{\cos\phi_i \cos\phi_j}{\pi R_{ij}^2}\right).$$

Applying $\partial\hat{T}_0/\partial z = 0$ and pulling the constant parameters, i.e. $\hat{\Delta}T$ and $\hat{H}$, outside the derivative leads to

$$\hat{k}_s \frac{\hat{\Delta T}}{\hat{H}} \frac{\partial T}{\partial z}\bigg|_i^s - \hat{k}_f \frac{\hat{\Delta T}}{\hat{H}} \frac{\partial T}{\partial z}\bigg|_i^f + \hat{\sigma}\hat{\Delta T}^4 \left(T_i + \frac{\hat{T}_0}{\hat{\Delta T}}\right)^4 = \tag{4.18}$$

$$\hat{\sigma}\sum_{j=1}^{N} A_j \hat{\Delta T}^4 \left(T_j + \frac{\hat{T}_0}{\hat{\Delta T}}\right)^4 \frac{\cos\phi_i \cos\phi_j}{\pi R_{ij}^2}$$

$$+ \hat{\sigma}\hat{\Delta T}^4 \left(T_{out} + \frac{\hat{T}_0}{\hat{\Delta T}}\right)^4 \left(1 - \sum_{j=1}^{N} A_j \frac{\cos\phi_i \cos\phi_j}{\pi R_{ij}^2}\right)$$

and after multiplying by $\hat{H}/\hat{\Delta T}\hat{k}_f$ one obtains

$$\frac{\hat{k}_s}{\hat{k}_f}\frac{\partial T}{\partial z}\bigg|_i^s - \frac{\partial T}{\partial z}\bigg|_i^f + \frac{\hat{\sigma}\hat{\Delta T}^3\hat{H}}{\hat{k}_f}\left(T_i + \frac{\hat{T}_0}{\hat{\Delta T}}\right)^4 = \frac{\hat{\sigma}\hat{\Delta T}^3\hat{H}}{\hat{k}_f}\sum_{j=1}^{N} A_j\left(T_j + \frac{\hat{T}_0}{\hat{\Delta T}}\right)^4 \frac{\cos\phi_i\cos\phi_j}{\pi R_{ij}^2} \tag{4.19}$$
$$+ \frac{\hat{\sigma}\hat{\Delta T}^3\hat{H}}{\hat{k}_f}\left(T_{out} + \frac{\hat{T}_0}{\hat{\Delta T}}\right)^4\left(1 - \sum_{j=1}^{N} A_j\frac{\cos\phi_i\cos\phi_j}{\pi R_{ij}^2}\right).$$

Here, a dimensionless control parameters for radiation, namely the radiation number

$$Nr = \frac{\hat{\sigma}\hat{\Delta T}^3\hat{H}}{\hat{k}_f} \tag{4.20}$$

and the temperature ratio

$$\Theta = \frac{\hat{T}_0}{\hat{\Delta T}} = \frac{0.5\left(\hat{T}_{bot} + \hat{T}_{top}\right)}{\hat{T}_{bot} - \hat{T}_{top}} \tag{4.21}$$

are introduced together with the view factor based on the dimensionless quantities

$$F_{ij} = A_j\frac{\cos\phi_i\cos\phi_j}{\pi R_{ij}^2} \tag{4.22}$$

and the thermal conductivity ratio

$$\lambda_k = \frac{\hat{k}_s}{\hat{k}_f}. \tag{4.23}$$

Applying (4.20)–(4.23) to (4.19) leads to

$$\lambda_k\frac{\partial T}{\partial z}\bigg|_i^s - \frac{\partial T}{\partial z}\bigg|_i^f + Nr(T_i + \Theta)^4 = Nr\sum_{j=1}^{N}\left(T_j + \Theta\right)^4 F_{ij} + Nr(T_{out} + \Theta)^4\left(1 - \sum_{j=1}^{N} F_{ij}\right). \tag{4.24}$$

The temperature gradients at both sides of a surface element i located at the bottom interface are calculated using 4th order polynomials

$$\begin{aligned}\frac{\partial T}{\partial z}\bigg|_i^f &= a_1T_i + a_2T_{i+1} + a_3T_{i+2} + a_4T_{i+3} \\ \frac{\partial T}{\partial z}\bigg|_i^s &= b_1T_i + b_2T_{i-1} + b_3T_{i-2} + b_4T_{i-3},\end{aligned} \tag{4.25}$$

where $(a_1, ..., a_4)$ and $(b_1, ..., b_4)$ are the coefficients calculated at the non-equidistant grid for the fluid and solid layer, respectively. Thus, from equation (4.24) one obtains

$$(\lambda_k b_1 - a_1)\, T_i + Nr(T_i + \Theta)^4 = Nr \sum_{j=1}^{N} \left(T_j + \Theta\right)^4 F_{ij} + Nr(T_{out} + \Theta)^4 \left(1 - \sum_{j=1}^{N} F_{ij}\right) \tag{4.26}$$
$$- \lambda_k(b_2 T_{i-1} + b_3 T_{i-2} + b_4 T_{i-3}) + a_2 T_{i+1} + a_3 T_{i+2} + a_4 T_{i+3}.$$

The interface conditions (4.26) are nonlinear in the temperature, aside from the fact that the radiosity itself is a function of temperature. In order to apply them to radiation simulations and efficiently solve for the temperature, it is necessary to approximate the temperature at the interfaces. To choose the best approximation of $(T + \Theta)^4$, two different approaches are tested.

Firstly, the approximation of $(T_i + \Theta)^4$ is obtained using Taylor series expansion. A function

$$f\,(T_i) = (T_i + \Theta)^4 \tag{4.27}$$

is defined and the temperature at a surface element i located at the bottom interface is evaluated around the heating plate, i.e. $T_i = T_{bot} - \Delta T_s$, where ΔT_s is the temperature difference between the heating plate and a surface element i. This leads to

$$f\,(T_{bot} - \Delta T_s) = (T_i + \Theta)^4 \tag{4.28}$$

for which the Taylor series expansion yields

$$f\,(T_{bot} - \Delta T_s) = f\,(T_{bot}) + \frac{f'\,(T_{bot})\,(-\Delta T_s)^1}{1!} + \frac{f''\,(T_{bot})\,(-\Delta T_s)^2}{2!} + ... \quad . \tag{4.29}$$

Since ΔT_s is small, the second and higher order terms can be neglected. Hence,

$$f\,(T_{bot} - \Delta T_s) = (T_{bot} + \Theta)^4 + 4(T_{bot} + \Theta)^3\,(-\Delta T_s) + \mathcal{R}. \tag{4.30}$$

Taking into account that $\Delta T_s = T_{bot} - T_i$, (4.28) can be written with the help of (4.30) as follows

$$(T_i + \Theta)^4 = (T_{bot} + \Theta)^4 - 4T_{bot}(T_{bot} + \Theta)^3 + 4T_i\,(T_{bot} + \Theta)^3\,. \tag{4.31}$$

Finally, the temperature at a surface element i located at the bottom interface is

given by

$$T_i^{TSE} = \frac{Nr\sum_{j=1}^{N}\left(T_j+\Theta\right)^4 F_{ij} + Nr(T_{out}+\Theta)^4\left(1-\sum_{j=1}^{N}F_{ij}\right)}{\lambda_k b_1 - a_1 + 4Nr\left(T_{bot}+\Theta\right)^3} - \frac{Nr\left((T_{bot}+\Theta)^4 - 4T_{bot}(T_{bot}+\Theta)^3\right)}{\lambda_k b_1 - a_1 + 4Nr\left(T_{bot}+\Theta\right)^3} - \frac{\lambda_k(\sum_{k=1}^{3} b_{k+1}T_{i-k}) - \sum_{k=1}^{3} a_{k+1}T_{i+k}}{\lambda_k b_1 - a_1 + 4Nr(T_i+\Theta)^3}. \tag{4.32}$$

Deriving the temperature at the interface around the heating plate using Taylor series expansion leads to approximation errors of the order 10^{-3}, which is too large.

Secondly, the temperature at the bottom interface is approximated by Newton–Raphson method

$$T_i^{NRM} = T_i - \frac{f\left(T_i\right)}{f'\left(T_i\right)}, \tag{4.33}$$

where

$$\begin{aligned} f\left(T_i\right) = {} & \left(\lambda_k b_1 - a_1\right) T_i + Nr(T_i+\Theta)^4 \\ & - Nr\sum_{j=1}^{N}\left(T_j+\Theta\right)^4 F_{ij} \\ & - Nr(T_{out}+\Theta)^4\left(1-\sum_{j=1}^{N}F_{ij}\right) \\ & + \lambda_k(b_2T_{i-1} + b_3T_{i-2} + b_4T_{i-3}) \\ & - (a_2T_{i+1} + a_3T_{i+2} + a_4T_{i+3}). \end{aligned} \tag{4.34}$$

Finally, the heat flux is constant at both sides of the interface when the tempera-

ture at a surface element i located at the bottom interface is

$$T_i^{NRM} = T_i - \frac{(\lambda_k b_1 - a_1)\, T_i + Nr(T_i + \Theta)^4}{\lambda_k b_1 - a_1 + 4Nr(T_i + \Theta)^3} \tag{4.35}$$
$$- \frac{-Nr \sum_{j=1}^{N} (T_j + \Theta)^4 F_{ij} - Nr(T_{out} + \Theta)^4 \left(1 - \sum_{j=1}^{N} F_{ij}\right)}{\lambda_k b_1 - a_1 + 4Nr(T_i + \Theta)^3}$$
$$- \frac{\lambda_k (\sum_{k=1}^{3} b_{k+1} T_{i-k}) - \sum_{k=1}^{3} a_{k+1} T_{i+k}}{\lambda_k b_1 - a_1 + 4Nr(T_i + \Theta)^3}.$$

This allows decreasing the approximation error to 10^{-11} after few iterations. Thus, the latter approach is used for the simulations discussed in this study.

Interface conditions at the top interface.
The sketch of the heat gain and loss is shown in Figure 4.4, and the balance equation for the heat flux at a surface element j reads

$$\hat{q}_j^{diff} + \sum_{sw=1}^{N} \hat{q}_{sw\to j}^{ir} + \sum_{i=1}^{N} \hat{q}_{i\to j}^{ir} = \hat{q}_j^{e} + \hat{q}_j^{cond}, \tag{4.36}$$

where $\hat{q}_j^{diff}$ is the diffusive heat flux calculated at the fluid side of the top interface and $\hat{q}_j^{cond}$ is the conductive heat flux calculated at the solid side of the top interface, $\hat{q}_j^{e}$ represents the total heat emission from the interface, while $\hat{q}_{i\to j}^{ir}$ and $\hat{q}_{sw\to j}^{ir}$ stand for the irradiative heat flux from the bottom interface and the ambient environment, respectively. With the help of equa-

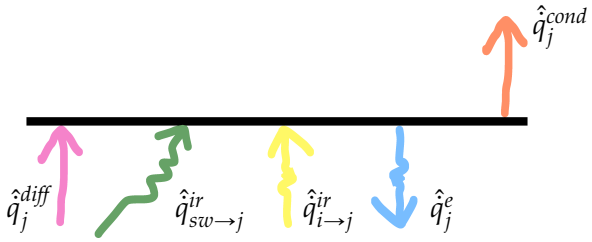

FIGURE 4.4: Heat flux decomposition at the top interface in the presence of radiation.

tions (4.4), (4.6), (4.8), (4.9), (4.14), (4.15), equation (4.36) can be expanded to

$$\overbrace{-\hat{k}_f \frac{\partial \hat{T}}{\partial \hat{z}}\bigg|_j^f}^{\hat{q}_j^{diff}} + \overbrace{\hat{\sigma}\hat{T}_{out}^4 \left(1 - \sum_{i=1}^{N} \hat{A}_i \frac{\cos\phi_i \cos\phi_j}{\pi \hat{R}_{ij}^2}\right)}^{\sum_{sw=1}^{N} \hat{q}_{sw\to j}^{ir}} + \overbrace{\sum_{i=1}^{N} \hat{\sigma}\hat{T}_i^4 \hat{A}_i \frac{\cos\phi_i \cos\phi_j}{\pi \hat{R}_{ij}^2}}^{\sum_{i=1}^{N} \hat{q}_{i\to j}^{ir}} = \underbrace{\hat{\sigma}\hat{T}_j^4}_{\hat{q}_j^e} \underbrace{-\hat{k}_s \frac{\partial \hat{T}}{\partial \hat{z}}\bigg|_j^s}_{\hat{q}_j^{cond}} \tag{4.37}$$

which, after applying the Newton–Raphson method, leads to the temperature at the top interface

$$\begin{aligned} T_j^{NRM} = T_j &- \frac{(c_1 - \lambda_k d_1)\, T_j + Nr\big(T_j + \Theta\big)^4}{c_1 - \lambda_k d_1 + 4Nr\big(T_j + \Theta\big)^3} \\ &- \frac{-Nr \sum_{i=1}^{N} (T_i + \Theta)^4 F_{ji} - Nr(T_{out} + \Theta)^4 \left(1 - \sum_{i=1}^{N} F_{ji}\right)}{c_1 - \lambda_k d_1 + 4Nr\big(T_j + \Theta\big)^3} \\ &+ \frac{c_2 T_{j-1} + c_3 T_{j-2} + c_4 T_{j-3} - \lambda_k (d_2 T_{i+j} + d_3 T_{j+2} + d_4 T_{j+3})}{c_1 - \lambda_k d_1 + 4Nr\big(T_j + \Theta\big)^3}, \end{aligned} \tag{4.38}$$

where $(c_1, ..., c_4)$ and $(d_1, ..., d_4)$ are the coefficients calculated at the non-equidistant grid for the fluid and solid layers, respectively.

4.6 Initial conditions

The first simulation is performed for the Rayleigh number $Ra = 3.5 \times 10^5$ in a cell with infinitely thin isothermal walls. It is initialised from the quiescent flow where all the velocity components inside the computational domain are zero, and a linear temperature distribution between the heating and cooling plates. Additionally, the temperature field is pointwise disturbed to trigger the onset of convection. After around 100 time units, a fully developed flow is obtained. DNS for higher Ra are initialised with a flow field produced by a DNS for the closest Rayleigh number. Whenever required, the flow field is interpolated to a finer mesh.

In principal, fully developed turbulent Rayleigh–Bénard convection is independent of the initial conditions. However, the better the initial conditions are, the less time is needed to reach the fully developed state. Optimal initial fields

reflect such effective Nusselt and Rayleigh numbers, which are as close as possible to the target ones. Since the computational time strongly depends on the complexity of the model, knowing the optimal initial conditions is particularly important when the fluid is bounded by solid plates of a certain thickness, and even more critical when radiative heat transfer is taken into account. However, when solid plates are employed, the effective Nusselt and Rayleigh numbers are not known *a priori*. Thus, in order to initialise the flow in a RB cell with solid plates, the fields obtained from the simulations without the plates reflecting the closest Ra are used instead of the ones reflecting the closest Ra_{eff}. Furthermore, since the temperatures at the interfaces are also unknown, the initial temperatures within the bottom and top plates are set to $T_{bot} = +0.5$ and $T_{top} = -0.5$, respectively.

The simulations performed in the presence of radiation are initialised from the corresponding ones in the absence of radiation.

4.7 Resolution requirements

The grid resolution requirements are discussed with respect to the fluid of a Prandtl number $Pr = 0.7$, which is used in this study.

In Section 4.7.1, the meshing criteria for the DNS performed for the cell with infinitely thin plates are discussed. The discussion includes the grid resolution study conducted for the moderate Rayleigh number, i.e. $Ra = 1.05 \times 10^6$, and for the highest Rayleigh number considered in this research, i.e. $Ra = 6.3 \times 10^7$.

Further, in Section 4.7.2 the resolution for the simulations in the cell with solid plates of a finite thickness is shortly discussed. In addition, the meshing of the solid plates and the influence of plates' conductivity and radiation on the resolution requirements of the fluid layer is addressed.

4.7.1 Grid resolution for simulations in the cell with infinitely thin plates.

In a perfect direct numerical simulations all the small-scale motions have to be resolved. This implies a sufficiently small grid which is able to capture them. Otherwise, the small eddies that are responsible for energy dissipation are ignored, which leads to e.g. excessive heat transfer estimations. In the case of isotropic turbulence, the Kolmogorov microscales (Kolmogorov 1941)

$$\eta_K(x,y,z,t) = \left(\frac{\nu^3}{\epsilon_u(x,y,z,t)}\right)^{1/4}, \tag{4.39}$$

in which ϵ_u denotes the turbulent dissipation rate, and the Batchelor length scale (Batchelor et al. 1959)

$$\eta_B(x,y,z,t) = \eta_K(x,y,z,t)Pr^{-1/2} \tag{4.40}$$

characterise the smallest flow structures. In the present study, all simulations are performed for $Pr < 1$. Thus, assuming that isotropic turbulence holds at least locally, the Kolmogorov scales are the most crucial and the smallest scales of turbulence. Kunnen et al. (2008) show that the local Kolmogorov scales η_K are smaller close to the walls than in the bulk. Therefore, in order to properly resolve the boundary layers, non-equidistant grid spacing is employed for the fluid layer, based on a hyperbolic tangent function as described in Shishkina and Wagner (2007a).

Boundary layer resolution.
The maximum mesh size in the boundary layers

$$h^{BL} \leqslant \eta_K^{BL} = 2^{-3/2}a^{-1}Nu^{-3/2}Pr^{0.5355-0.033logPr}H \tag{4.41}$$

and the minimum number of nodes in the thermal and kinetic BL

$$\tilde{n}_{T,BL} \geqslant \sqrt{2}aNu^{1/2}Pr^{-0.5355+0.033logPr} \tag{4.42}$$

$$\tilde{n}_{u,BL} \geqslant \sqrt{2}aNu^{1/2}Pr^{-0.1785+0.011logPr} \tag{4.43}$$

are estimated according to the criterion by Shishkina et al. (2010) for $3 \times 10^{-4} \leqslant Pr \leqslant 1$ and empirically obtained constant $a \approx 0.482$. This approach provides the needed grid spacing assuming a laminar Prandtl–Blasius type BL. The obtained estimations are afterwards adjusted to be valid for more complex BL type by following Shishkina et al. (2014) who introduced the correction factor that eventually decreases the maximum mesh size in the BL. The Nusselt number in (4.42)–(4.43) is estimated from $Nu \sim Ra^{0.284}$ obtained by Kaczorowski and Wagner (2007) for the same Rayleigh–Bénard cell. The resulting estimations of the minimum number of nodes in the BLs are listed in Table 4.1. For $Ra = 3.5 \times 10^5$ five and four nodes are located in the thermal and kinetic BL, respectively. For $Ra = 6.3 \times 10^7$ there are eight and seven nodes.

Moreover, a grid resolution study for the BL was performed by Kaczorowski (2009); Kaczorowski and Wagner (2010) in a similar Rayleigh–Bénard cell with periodic boundary conditions. They found that for $Ra = 3.5 \times 10^5$ it is sufficient to cluster eight grid points in the BL. Furthermore, for $Ra = 3.5 \times 10^7$ increasing the number of points from five to ten did not significantly change neither the volume-averaged Nusselt number nor the time- and area-averaged temperature profiles. However, the differences in the higher order moments like skewness and kurtosis were noticed.

	N_x	N_y	N_z	n_T	$\tilde{n}_T$	n_u	$\tilde{n}_u$	$\langle Nu \rangle_{t,V} \pm \delta$
$Ra = 1.05 \times 10^6$	128	64	64	12	5	10	4	8.616 ± 0.012
	320	64	64	12	5	10	4	8.613 ± 0.012
	320	96	96	15	5	13	4	8.616 ± 0.005
	448	96	96	15	5	13	4	8.602 ± 0.007
	448	128	128	17	5	15	4	8.604 ± 0.005
$Ra = 6.3 \times 10^7$	128	64	64	6	8	5	7	32.753 ± 0.085
	128	96	96	6	8	5	7	31.922 ± 0.031
	320	96	96	6	8	5	7	27.967 ± 0.034
	320	160	160	7	8	6	7	27.201 ± 0.011
	576	160	160	7	8	6	7	27.201 ± 0.011
	576	192	192	7	8	6	7	27.180 ± 0.011
	576	256	256	8	8	7	7	27.164 ± 0.024
	1024	256	256	8	8	7	7	27.114 ± 0.024
	1216	256	256	8	8	7	7	27.128 ± 0.026

TABLE 4.1: Parameters and results of the grid resolution studies for the cell with ITP: number of mesh nodes in i-direction N_i ($i = x, y, z$), number of nodes in thermal/viscous boundary layer n_T/n_u, number of nodes required for proper accuracy in thermal/viscous boundary layer $\tilde{n}_T/\tilde{n}_u$ (including the correction factor from Shishkina et al. 2014), time- and volume-averaged Nusselt number $\langle Nu \rangle_{t,V}$ and its deviation δ.

It can be concluded that for moderate Rayleigh number, the required number of nodes reported by Kaczorowski (2009); Kaczorowski and Wagner (2010) is slightly higher than estimated by Shishkina et al. (2010, 2014) but for higher Ra the values are similar.

However, to be on the safe side, the mesh is checked with respect to capturing the time- and area-averaged Kolmogorov length scale $\langle \eta_K \rangle_{t,S_z}$ in the near-wall region. Since the predicted Kolmogorov length scale decreases with increasing mesh resolution (similarly to the Nusselt number), $\langle \eta_K \rangle_{t,S_z}$ is plotted in Figures 4.5 and 4.6 for the finest mesh, namely $448 \times 128 \times 128$ and $1216 \times 256 \times 256$ for $Ra = 1.05 \times 10^6$ (Figure 4.5) and $Ra = 6.3 \times 10^7$ (Figure 4.6), respectively.

In principle, the mesh resolution is considered to be sufficient if the mean grid width is smaller than $\langle \eta_K \rangle_{t,S_z}$. In various studies, different definitions of the mean grid width are used (Clark et al. (1979); Horn et al. (2013); Spalart et al. (1997); Deardorff (1973) or Shi et al. (2012) for cylindrical coordinates). In the present study, the geometric mean grid width defined by Clark et al. (1979)

$$h_{g.m.} = \frac{1}{3}\sqrt{\Delta_x^2 + \Delta_y^2 + \Delta_z^2} \tag{4.44}$$

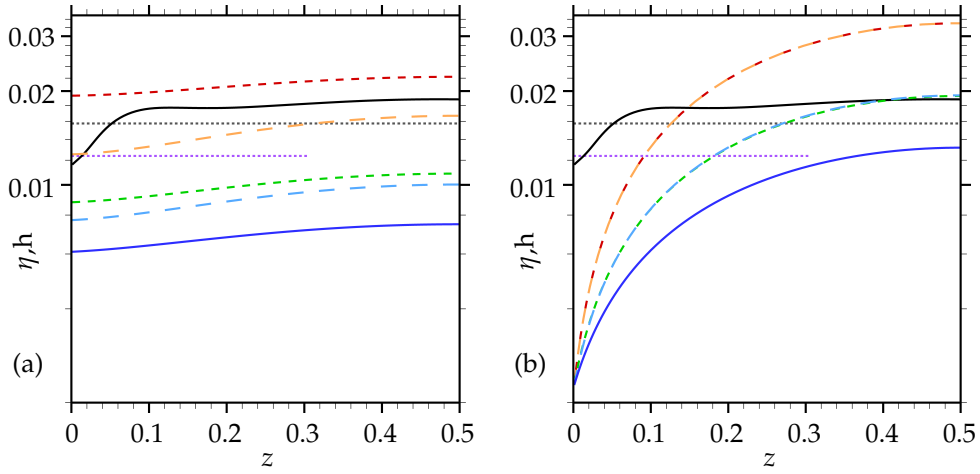

FIGURE 4.5: The time- and area-averaged Kolmogorov length scale $\langle \eta_K \rangle_{t,S_z}$ (—) and the theoretical estimates of the maximum mesh size in the BLs h^{BL} (· · ·) and the bulk h^{bulk} (· · ·) in comparison with the mesh spacing $h_{g.m.}$ (a) and h_z (b) for $Ra = 1.05 \times 10^6$ and grid resolutions: $64 \times 64 \times 128$ (- - -), $64 \times 64 \times 320$ (– –), $96 \times 96 \times 320$ (- - -), $96 \times 96 \times 448$ (– –), $128 \times 128 \times 448$ (—).

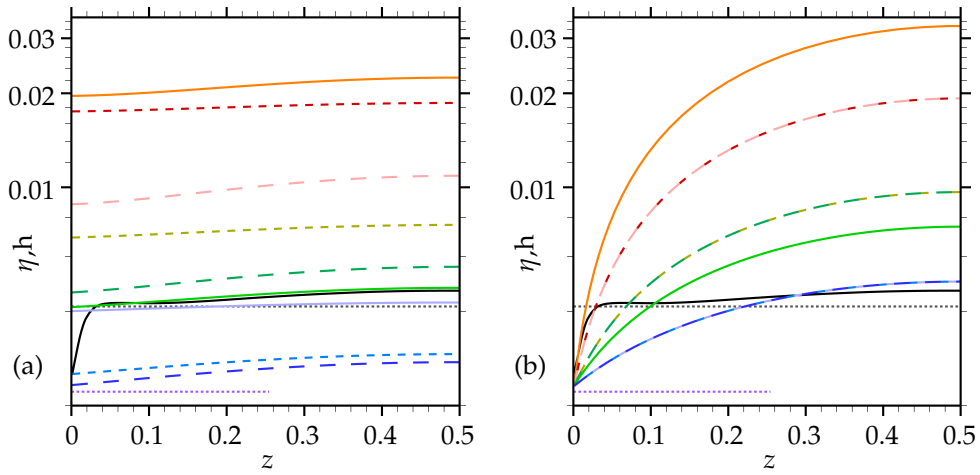

FIGURE 4.6: The time- and area-averaged Kolmogorov length scale $\langle \eta_K \rangle_{t,S_z}$ (—) and the theoretical estimates of the maximum mesh size in the BLs h^{BL} (· · ·) and the bulk h^{bulk} (· · ·) in comparison with the mesh spacing $h_{g.m.}$ (a) and h_z (b) for $Ra = 6.3 \times 10^7$ and grid resolutions: $64 \times 64 \times 128$ (—), $96 \times 96 \times 128$ (- - -), $96 \times 96 \times 320$ (– –), $160 \times 160 \times 320$ (- - -), $160 \times 160 \times 576$ (– –), $192 \times 192 \times 576$ (—), $256 \times 256 \times 576$ (—), $256 \times 256 \times 1024$ (- - -), $256 \times 256 \times 1216$ (– –).

and the vertical grid spacing

$$h_z = \Delta_z \tag{4.45}$$

are both considered. Additionally, $h_{g.m.}$ is plotted in Figures 4.5a and 4.6a and h_z is plotted in Figures 4.5b and 4.6b.

These Figures clearly show that in the BL region and for a certain mesh $h_{g.m.} < h_z$. Thus, the requirements for the grid resolution are more restrictive for $h_{g.m.}$. This happens because the cells in the BL are usually wide with respect to widthwise and lengthwise directions, but they are not that high. In this respect, the BL is well resolved if at least 96 and 256 grid points are clustered in the vertical direction for $Ra = 1.05 \times 10^6$ and $Ra = 6.3 \times 10^7$, respectively. According to Table 4.1, which shows the number of grid points clustered in the BL for all simulations included in Figures 4.5–4.6, this amount of grid nodes corresponds to at least 15 and 13 cells in the thermal and viscous BLs for $Ra = 1.05 \times 10^6$. Further, it also corresponds to at least eight and seven cells for $Ra = 6.3 \times 10^7$.

Figures 4.5–4.6 further show the estimations of the maximum size of the grid spacing in the boundary layer according to (4.41) with the correction factor by Shishkina et al. (2014). Comparing these values with $\langle \eta_K \rangle_{t,S_z}$ reveals that the estimations are about 7% greater than the Kolmogorov length scale for $Ra = 1.05 \times 10^6$ (Figure 4.5) and about 12% lower for $Ra = 6.3 \times 10^7$ (Figure 4.6). Thus, they are too weak for $Ra = 1.05 \times 10^6$ and too restrictive for $Ra = 6.3 \times 10^7$.

Bulk resolution.

In order to determine the necessary grid spacing in the core region, the grid resolution study have been performed for $Ra = 1.05 \times 10^6$ and $Ra = 6.3 \times 10^7$. The resolution is considered to be sufficient if the global Nusselt number does not significantly drop with further grid refinement. The time- and volume-averaged Nusselt numbers $\langle Nu \rangle_{t,V}$ and their standard deviations obtained for the simulations used in the grid resolution study are listed in Table 4.1. They reveal that 96 grid points in the vertical and widthwise directions and 320 grid points in the lengthwise direction are sufficient for $Ra = 1.05 \times 10^6$. For the higher Rayleigh number, i.e. $Ra = 6.3 \times 10^7$, the Nusselt number significantly decreases with an increasing number of grid points, up to $160 \times 160 \times 320$. Further refinements lead only to a slight change of $\langle Nu \rangle_{t,V}$.

However, to be on the safe side, the mesh is checked with respect to capturing the time- and area-averaged Kolmogorov length scale $\langle \eta_K \rangle_{t,S_z}$ in the core region. The verification process is the same as the one taken for the near-wall region. In this respect, the mesh resolution is considered to be sufficient if the mean grid width defined by (4.44) and (4.45) is smaller than $\langle \eta_K \rangle_{t,S_z}$.

The presented profiles of $h_{g.m.}$, h_z and $\langle \eta_K \rangle_{t,S_z}$ for $Ra = 1.05 \times 10^6$ in Figure 4.5 reveal that the bulk region is underresolved for the grids which comprise 64 grid cells in the vertical and widthwise directions. On the other hand, 96 grid points

in the vertical and widthwise directions are just sufficient to properly resolve the bulk region, while 128 cells lead to an unnecessarily fine resolution there. Analogously, the profiles of $h_{g.m.}$, h_z and $\langle \eta_K \rangle_{t,S_z}$ for $Ra = 6.3 \times 10^7$ in Figure 4.6 reveal that 256 cells are needed in the vertical and widthwise directions as well as 1024 cells in the lengthwise direction to guarantee a proper grid resolution in the bulk.

Furthermore, the maximum mesh size in the core region

$$h^{bulk} \leqslant \eta_K^{bulk} = \frac{Pr^{1/2}}{(Nu-1)^{1/4} Ra^{1/4}} H \tag{4.46}$$

is estimated according to the criterion by Shishkina et al. (2010) and plotted in Figures 4.5–4.6. This requirement is the alternative for the π times less restrictive, but still widely used, estimation proposed by Grötzbach (1983) and determines a computationally expensive upper limit. Comparing the estimations obtained from (4.46) with $\langle \eta_K \rangle_{t,S_z}$ reveals that the bulk resolution criterion by Shishkina et al. (2010) is just accurate for $Ra = 6.3 \times 10^7$ but too restrictive for $Ra = 1.05 \times 10^6$.

Taking into account the above discussion, the bulk and the the boundary layer is properly resolved if a grid with 1216 cells in the lengthwise direction and 256 cells in the remaining two directions is selected for $Ra = 6.3 \times 10^7$. For $1.05 \times 10^6 < Ra < 6.3 \times 10^7$ a slightly coarser grid with 1024 cells in the lengthwise direction is used. Nevertheless, for any Rayleigh number from this region, the Kolmogorov length scale is still slightly smaller than the mean grid width. Finally, for $Ra \leqslant 1.05 \times 10^6$, it turned out to be sufficient to use 96 grid points in the vertical and widthwise directions and 320 grid points in the lengthwise direction.

4.7.2 Grid resolution for simulations in the cell with solid plates of a finite thickness

Resolving the solid layer.
In two horizontal directions, the grid resolution follows the one of the fluid layer. In the vertical direction, an arbitrary number of 20 equally distributed computational mesh nodes is elected, which is verified to be large enough to ensure a smooth local temperature profiles through the low conductivity plates for the Rayleigh number $Ra = 6.3 \times 10^7$ (the highest considered in this study).

Furthermore, owing to the selected numerical method for calculation of the temperature at the solid–fluid interface, the number of nodes in the solid plates can not be significantly reduced although, it might be preferable when highly conductive plates are employed and/or the solution for lower Rayleigh number

is computed. Thus, 20 grid points are used in all simulations.

Resolving the fluid layer bounded with highly conductive plates (HCP). The results obtained by Czarnota and Wagner (2011a) show that the process of heat conduction through highly conductive plates is much faster than the process of removing the heat by convection, and hence a minor influence of highly conductive plates on the local temperature at the interfaces is observed. Due to above effects, the effective Rayleigh number defined by (2.18) is similar to the one obtained when infinitely thin plates are employed. All in all, the grid resolution for simulations in the cell equipped with HCP is the same as the one for ITP.

Resolving a fluid layer bounded with low conductivity plates (LCP). Czarnota and Wagner (2013) reported that the temperature distribution at the interface significantly differs from the one at the outer side of the plate when low conductivity plates are employed. It was also noted that the latter leads to a lower effective Rayleigh number, especially for $Ra = 3.5 \times 10^7$. Therefore, the grid resolution can be coarser for plates of low conductivity than for those with high conductivity. Finally, the number of grid points in the lengthwise and in the remaining two directions equals respectively 1024 and 256 for $Ra = 6.3 \times 10^7$, and 320 and 96 for $Ra = 1.84 \times 10^6$. However, for another Rayleigh numbers, the same amount of grid cells is used in order to secure more efficient domain decomposition.

Resolving the fluid layer in the presence of radiation. When HCP are employed, the effective Rayleigh number is weakly changed by radiation (Czarnota and Wagner 2011a). On the contrary, for LCP the Ra_{eff} strongly depends on the control parameters for radiation (Czarnota and Wagner 2014) and is not known *a priori*. Thus, in order to provide a sufficient grid resolution, which is independent of the control parameters for radiation, the resolution for all simulations with radiation modelling is the same as the one used for their representatives where radiation is absent.

4.8 Code validation

The verification of the radiation model is done by checking if the following relations are satisfied:

$$\hat{q}_{e,i} = \hat{q}_{b\to sw} + \hat{q}_{b\to t} \tag{4.47}$$

$$\hat{q}_{e,j} = \hat{q}_{t\to sw} + \hat{q}_{t\to b}. \tag{4.48}$$

The above relations are satisfied to the same order as the approximation of the interface temperature. Thus, it can be concluded that the numerical method

solves the radiation model adequately. Moreover, the verification and validation of the convection model was performed by Kaczorowski (2009). Note that the discrete radiation equations are solved in the same discrete space as the momentum and energy equations (i.e. identical mesh).

4.9 Parallelisation

The communication and synchronisation between the processes is made with the use of Message Passing Interface (MPI). The code was compiled using Intel Fortran Compiler, and all the computations were performed in Simulation Center of Aerodynamic Research In Transportation (SCART) on *Höchstleistungsrechner Kabine Göttingen* (HKG) computer cluster. This cluster consists of 2×2.67 GHz Intel(R) Xeon(R) X5650 processors and each processor comprises 6 cores and 24 GB RAM.

Decomposition of the fluid layer.
A one dimensional (1D) domain decomposition in z-direction is employed in such way that horizontal slices, consisting of similar number of elements, are constructed. This ensures that the total number of the required arithmetic operations is equally distributed between all the cores, and thus the time spent for synchronisation is the shortest. In order to use the 4th-order spatial discretization scheme, each subdomain is equipped with two horizontal layers of the ghost cells located at the boundary between neighbouring subdomains. Their values are calculated on neighbouring cores and exchanged using MPI interface. The number of cores that are used for the domain decomposition ($NCORE$) has to be a power of two, i.e. 2^n ($n = 1, 2, 3, ...$). This is required by the method used for efficient transformation when solving the Poisson equation for the pressure.

Decomposition of the solid layer.
The entire bottom solid layer is computed by the first core and the top one is computed by the last core. In this way, the subdomain that is assigned to the first or the last core consists of slightly more elements than the subdomain assigned to the other cores. Nevertheless, when HCP are employed, the parallelisation speedup

$$S_{par} = \frac{WCT_{NCORE=1}}{WCT_{NCORE}} \tag{4.49}$$

differs only up to 4% from the one calculated when ITP are employed (see Figure 4.7a, data points for the absence of radiation and $Ra = 6.3 \times 10^7$). WCT, in (4.49), stays for Wall Clock Time and represents real time in seconds used for computing one time step (ts). Such a similar speedup indicates low cost of synchronisation when the present decomposition of the solid layer is used. This

is due to low number of arithmetic operations that are performed for the solid plates, and hence low time spent for computing the plates. Actually, analysing the *WCT* for the simulations in the cell with ITP and HCP from Figure 4.7b in case of sequentially run simulations ($NCORE = 1$), it turned out that the calculations of the heat diffusion through the solid plates takes only 0.4 s/ts.

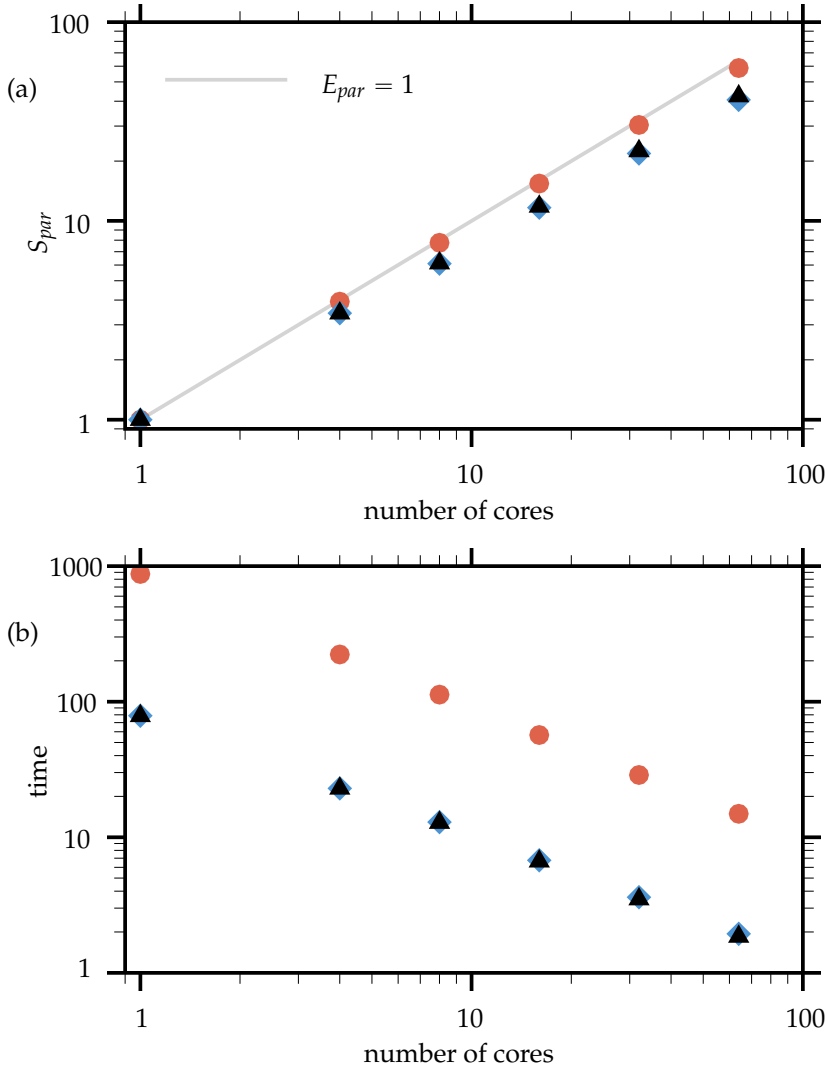

FIGURE 4.7: Parallelisation speedup (a) and the Wall Clock Time (b) versus the number of cores for $Ra = 6.3 \times 10^7$. Simulation with ITP (▲), simulation with HCP in the absence of radiation (◆) and in the presence of radiation for $Nr = 0.0008$ and $\Theta = 29$ (●).

Decomposition of the irradiation calculations.
The calculation of the irradiation implies the summation over the elements that contribute to the radiative heat exchange. Although, the assumption of trans-

parent side walls and constant temperature outside the cell allows to treat the irradiation originating from the side walls as one energy beam, there are still $N_x^2 \times N_y^2$ radiatively participating cells at the top and bottom interface. The last determines a high number of arithmetic operations which significantly increases the *WCT*. For $Ra = 6.3 \times 10^7$ and $256 \times 256 \times 1216$ volume elements, the *WCT* for the simulation in the cell with HCP equals 78.82 s/*ts*, while the *WCT* for the same simulation including radiation modelling rises to 874.87 s/*ts* (see Figure 4.7b, $NCORE = 1$). This means that irradiation calculations may slow down the entire simulation time even by a factor of 11. Therefore, it is clear that optimisation of the irradiation calculations is highly important. For this reason, spacial and temporal decomposition are employed.

Spatial decomposition. A solid–fluid interface which emits the radiation towards another interface is decomposed in y-direction into *NCORE* number of straps, i.e. slices of zero thickness. In this way, each core calculates a part of the total incoming radiation and sends this value to the core that does the remaining operations, namely the summation of the partial irradiation sums and finally the calculation of the temperature at the interface. Figure 4.7b reveals that the *WCT* decreases constantly with increasing number of cores. For example, for $NCORE = 1$ the simulation without radiation modelling is a factor of 11 faster, while the same simulation is faster by a factor of eight when 64 cores are used. Additionally, spatial decomposition of the irradiation calculations provides nearly linear speedup which is represented in Figure 4.7a as parallelisation efficiency $E_{par} = S_{par}/NCORE = 1$. This is because all the cores perform the same number of arithmetic operations which means short synchronisation time, and the communication is confined to sending only two real numbers.

Temporal decomposition. In order to calculate the temperature at the solid–fluid interface, the actual value of the radiative heat flux is needed for every time step. Due to numerical stability, the time step Δt is smaller than the Kolmogorov time scale τ_{η_K} by a factor of $\sim$100 for $Ra = 6.3 \times 10^7$. Since τ_{η_K} determines the shortest time associated with a physical process of scales motion, the radiative heat flux is calculated every 100 time steps. Furthermore, the latest value is used for the temperature calculations at every time step until the next recalculation is performed. In principle, by increasing the value of *TIR*, i.e. the number of elapsed time steps between the irradiation update, the irradiation calculations are conducted less frequently, and hence the entire simulation is performed faster. In order to quantify the time gain, simulations for different *TIR* values were conducted in the cell with HCP for $Ra = 6.3 \times 10^7$, $Nr = 0.0008$ and $\Theta = 29$. Table 4.2 shows the *WCT* and the parallelisation efficiency E_{par} when 64 cores were used. By increasing *TIR* from one to ten, the *WCT* is reduced by a factor of 4.3 while the efficiency drops from 0.92 to 0.72. Further enlargement of *TIR* does not considerably speed up the simulation, though it does not significantly decrease the parallelisation efficiency either. Moreover, it is important to realise that when the simulation is running for months, even a small time gained per time step

	$TIR = 1$	$TIR = 10$	$TIR = 20$	$TIR = 50$	$TIR = 100$
WCT	14.89	3.43	2.80	2.42	2.29
E_{par}	0.92	0.72	0.66	0.63	0.59
$MAE_{Nu_r}^{TIR}$	0.0	3×10^{-7}	5×10^{-7}	1×10^{-6}	2×10^{-6}

TABLE 4.2: The comparison of the Wall Clock Time [s], parallelisation efficiency [-] and relative mean absolute error [%] versus the number of elapsed time steps between the irradiation update [ts] for the simulation in the cell with HCP performed on 64 cores for $Ra = 6.3 \times 10^7$, $Nr = 0.0008$ and $\Theta = 29$.

significantly decreases the total simulation time. Finally, when irradiation is recalculated every 100 time steps and 64 cores are used, the simulation without radiation modelling runs about 18% faster compared to the one with radiation modelling. In order to quantify the influence of temporal decomposition on the results accuracy, the relative mean absolute error

$$MAE_{Nu_r}^{TIR} = 1/N \sum_{i=1}^{N} \frac{Nu_r^{TIR=1} - Nu_r^{TIR}}{Nu_r^{TIR}} \times 100\% \tag{4.50}$$

between the radiative Nusselt number, obtained for various values of TIR, is calculated. When the irradiation calculations are recalculated every ten time steps the error is 3×10^{-7}% (Table 4.2). However, the error does not significantly grow when TIR is increased up to 100, for which $MAE_{Nu_r}^{TIR} = 2 \times 10^{-6}$%. Thus, in the present study, all the simulations which account for radiation calculations are performed for $TIR = 100$. Moreover, all the simulations for $Ra > 10^7$ are performed on 64 cores, and simulations for $Ra < 10^7$ run on 16 cores.

5

RADIATION EFFECTS ON THE BULK DYNAMICS

5.1 Large-scale flow structures

In buoyancy driven flows, thermal plumes are generated close to the heated and cooled walls due to the high temperature gradients. These plumes are thermal whirls, which constantly rise and descend and interact with each other. In addition, they form large-scale flow structures, whose size and number depend on the geometry of the container and the working fluid (Kaczorowski and Wagner 2009; Horn et al. 2013; Wagner and Shishkina 2013; Wagner et al. 2012). However, little is known about the influence of radiative heat exchange on these structures, especially for the considered cuboidal geometry and the Prandtl number $Pr = 0.7$.

The instantaneous temperature isosurfaces obtained for $Ra = 6.3 \times 10^7$ and $\hat{\kappa}_s/\hat{\kappa}_f = 0.003$ in the absence and presence of radiation are plotted in Figure 5.1. They reveal that the thermal plumes are not significantly altered by surface radiation. Only the smallest plumes, particularly the ones which rise close to the widthwise walls, are less pronounced in the presence of radiation. The time-averaged temperature distributions with superimposed velocity vectors are shown in Figures 5.2a and 5.2b in the vertical cross-section S_y located at $y = 0.5$ and $\hat{\kappa}_s/\hat{\kappa}_f = 0.003$. They depict four counter rotating convection rolls of similar shape in similar locations independently of the radiation scenario.

Similar large-scale circulations are formed when the thermal diffusivity ratio is high, i.e. $\hat{\kappa}_s/\hat{\kappa}_f = 3.8$. Here, the time scales associated with heat conduction through high conductivity plates are much smaller than those induced by convection and radiation (Czarnota and Wagner 2011a). Hence, the interface

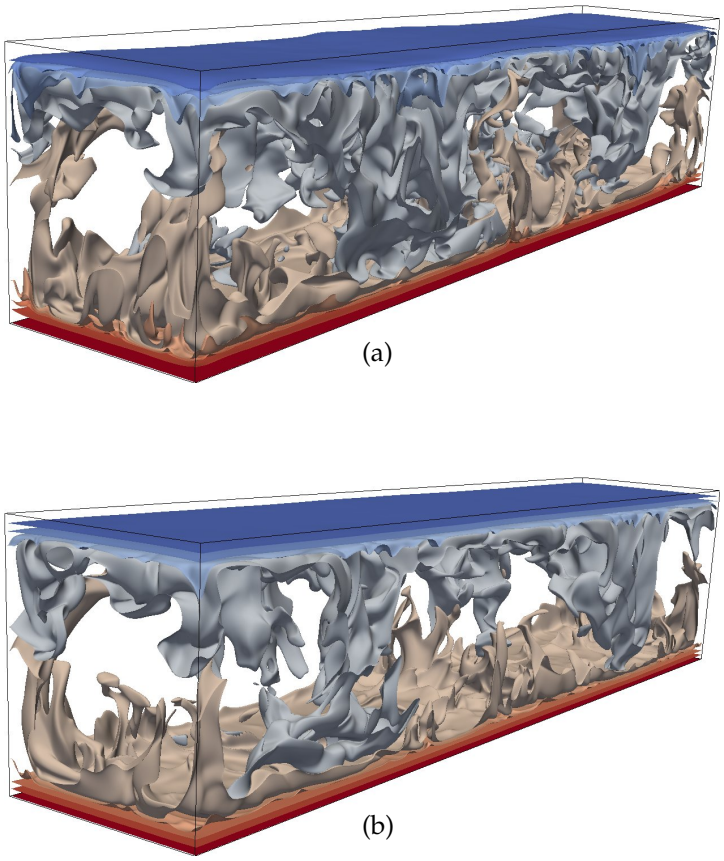

FIGURE 5.1: Ten instantaneous isosurfaces of temperature equidistantly distributed between $T = -0.5$ (blue) and $T = 0.5$ (red) in the absence of radiation (a) and in the presence of radiation (b) for $Ra = 6.3 \times 10^7$ and $\hat{\kappa}_s/\hat{\kappa}_f = 0.003$.

conditions resemble isothermal ones, and the obtained LSC are similar to those obtained by Kaczorowski and Wagner (2009) in the same geometry for isothermal boundary conditions and in the absence of radiation.

Recently, Saravanan and Sivaraj (2013) performed 2D simulations for a square cavity cooled from left and right with a horizontal heating plate located in the centre of the bulk. Although the top and bottom walls were adiabatic and the active walls were infinitely thin, they also found that radiation does not change the flow patterns. Furthermore, a weak effect of internal radiation on the velocity profiles was noticed by Xu et al. (2007) in an open vertical cylinder heated through its side wall and cooled at the top surface by radiation for $Ra = 2000$ and $Pr = 0.02$.

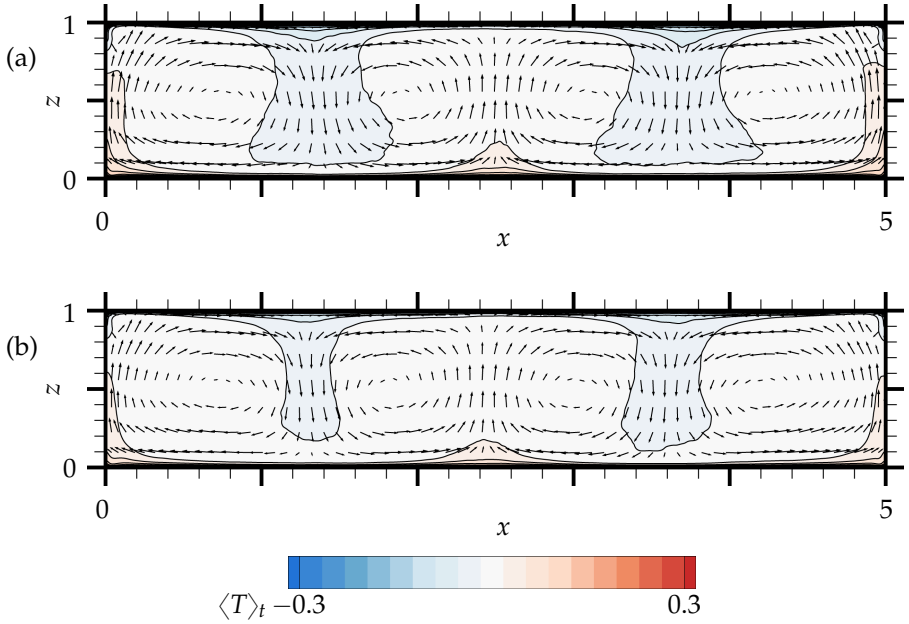

FIGURE 5.2: A vertical cross-section showing the distribution of $\langle T \rangle_t$ and $\langle u_i \rangle_t$ at $y = 0.5$ in the absence of radiation (a) and in the presence of radiation (b); $Ra = 6.3 \times 10^7$, $\hat{\kappa}_s/\hat{\kappa}_f = 0.003$. Note that, for the sake of clarity, only a reduced temperature range is presented.

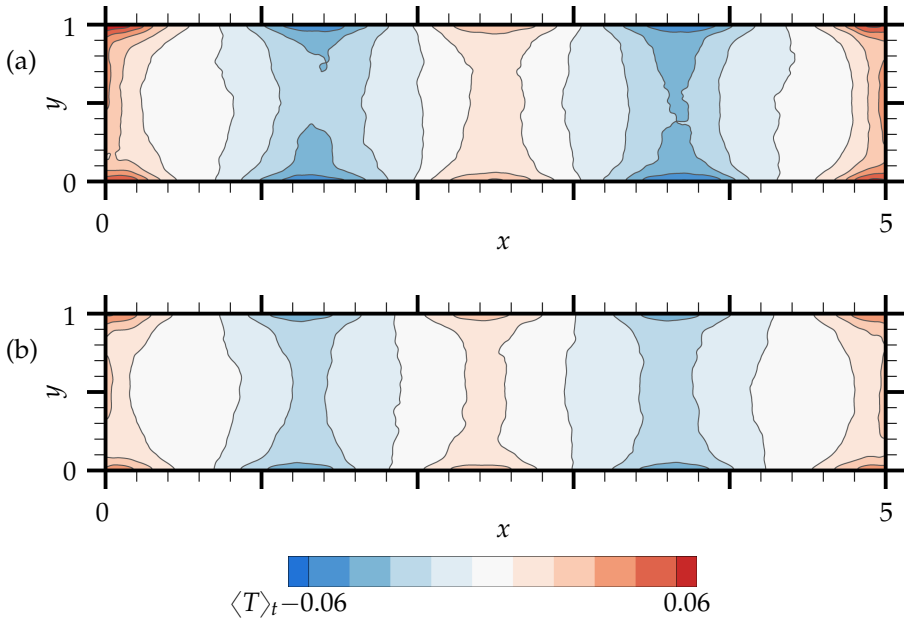

FIGURE 5.3: A horizontal cross-section showing the distribution of $\langle T \rangle_t$ at $z = 0.5$ in the absence of radiation (a) and in the presence of radiation (b); $Ra = 6.3 \times 10^7$, $\hat{\kappa}_s/\hat{\kappa}_f = 0.003$. Note that, for the sake of clarity, only a reduced temperature range is presented.

5.2 Homogeneity of the bulk temperatures

Despite the similar flow structures, Figure 5.1 clearly shows less instantaneous temperature isosurfaces in the bulk region in the presence of radiation than in its absence. Thus, radiation renders the bulk more uniform if low conductivity plates are employed. To quantify the level of homogeneity of the bulk temperatures, the volume probability density function (PDF) of the time-averaged temperatures is introduced and plotted in Figure 5.4 for both radiation scenarios and $Ra = 6.3 \times 10^7$. The peaks of the PDFs at $\langle T \rangle_t = 0$ reflect the probability of finding temperature values in the complete volume equal to the bulk temperature. Thus, any PDF peak value can be interpreted as a measure of the homogeneity of the temperature distribution in the bulk, which will be referred to as the bulk homogeneity. In this respect, the peak values of the PDFs extracted from Figure 5.4 reveal that radiation increases the homogeneity of the bulk by 45%. The transport mechanism responsible is revealed by following the plumes from the interfaces, where they are formed, to the bulk. In this respect, the span of the PDFs in Figure 5.4 reveals that the highest and lowest temperatures, which are associated with the temperatures of the generated plumes, are decreased and increased, respectively, due to radiation. Thus, the temperatures of rising/descending plumes are lower/higher in the presence of radiation than in its absence. Finally, the contours of the time-averaged temperatures plotted in the horizontal cross-section S_z at $z = 0.5$ in Figures 5.3a and 5.3b reflect plumes reaching the centre of the bulk. In these figures the warm and cold regions are thinner in the presence of radiation than in its absence. Thus, the regions with rising and descending plumes are also thinner. Thanks to the latter, the bulk's

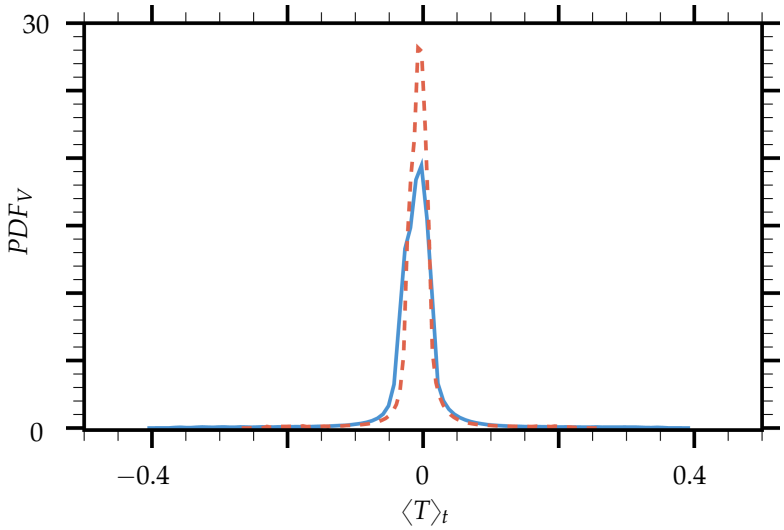

FIGURE 5.4: The volume probability density function (PDF_V) of $\langle T \rangle_t$ in the absence of radiation (—) and in the presence of radiation (- - -) for $Ra = 6.3 \times 10^7$ and $\hat{\kappa}_s/\hat{\kappa}_f = 0.003$.

regions formed between rising and descending plumes characterised by temperature values close to T_0 are larger in the presence of radiation, and hence a temperature distribution obtained in the bulk is more uniform.

To sum up, the homogeneity of the bulk is increased by radiation due to wider LSC which are driven by colder rising and warmer descending plumes in the presence of radiation than in its absence.

This radiation-induced increase in the bulk homogeneity was also observed by Ridouane et al. (2004), who considered a square Rayleigh–Bénard cell filled with a radiatively non-participating medium ($Pr = 0.71$) for a similar temperature ratio $\Theta = 29.35$ but lower Rayleigh- and radiation numbers than those in the present study. However, since they considered isothermal horizontal and adiabatic vertical walls, the mechanism was different.

In order to study how the bulk homogeneity changes with the Rayleigh number and the thermal diffusivity ratio, the values of the PDFs' peaks $PDF_{V,T=0}$ are plotted in Figure 5.5 for various Ra and both considered $\hat{\kappa}_s/\hat{\kappa}_f$.

For the considered radiation scenarios and thermal diffusivity ratios, the probability density at $\langle T \rangle_t = 0$ grows linearly with the logarithm of the Rayleigh number. This dependence justifies the least squares fitting $\xi(Ra) = a \cdot \ln(Ra) + b$ shown in Figure 5.5. Considering the case with low conductivity plates, radiation leads to an increase in the slope of the function ξ from $a = 2.22$ to

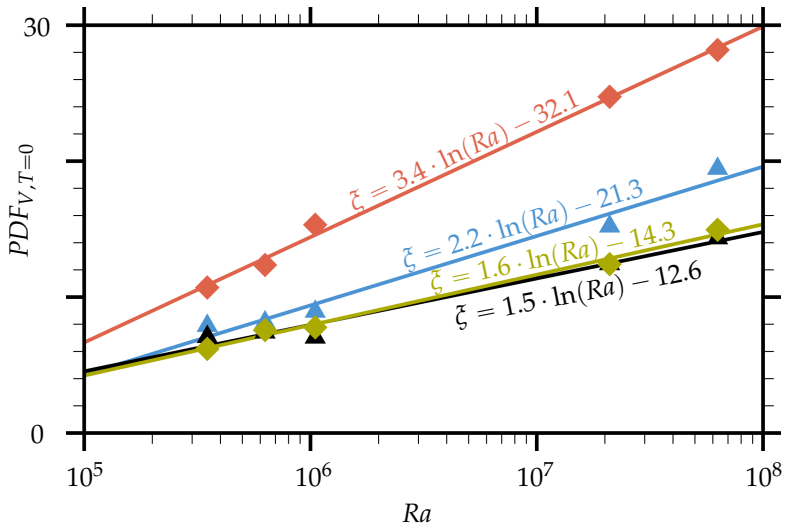

FIGURE 5.5: The magnitude of the volume probability density function (PDF_V) for $\langle T \rangle_t = 0$ in the absence of radiation, $\hat{\kappa}_s/\hat{\kappa}_f = 0.003$ (blue) and $\hat{\kappa}_s/\hat{\kappa}_f = 3.8$ (black) and in the presence of radiation, $\hat{\kappa}_s/\hat{\kappa}_f = 0.003$ (red) and $\hat{\kappa}_s/\hat{\kappa}_f = 3.8$ (green). The solid lines represent the least squares fittings $\xi(Ra) = a \cdot \ln(Ra) + b$, for which the standard deviation (fitting error) is below 0.51, and the symbols indicate the corresponding data.

$a = 3.36$. The corresponding fitting errors equal 0.9% and 0.4% in the absence and presence of radiation, respectively. Since the slopes of ξ are positive, the bulk homogeneity increases with *Ra* independently of the radiation scenario. The reason is that the turbulence and mixing process in the bulk are intensified for larger Rayleigh numbers. Nevertheless, in the presence of radiation, the slope is steeper by a factor of 1.52 than it is in the absence of radiation. Thus, the increase in the bulk homogeneity with *Ra* is 52% greater in the presence of radiation.

Figure 5.5 further reveals that the slope of ξ increases from $a = 1.48$ to $a = 1.61$ due to radiation for $\hat{\kappa}_s/\hat{\kappa}_f = 3.8$, and the corresponding fitting errors are 0.8% and 0.4%, respectively. Hence, when high conductivity plates are employed, the increase in the bulk homogeneity with *Ra* is 9% stronger in the presence of radiation than in its absence. Furthermore, comparing the slopes of ξ obtained for $\hat{\kappa}_s/\hat{\kappa}_f = 0.003$ and $\hat{\kappa}_s/\hat{\kappa}_f = 3.8$ in the presence of radiation reveals that the bulk homogeneity increases with *Ra* 2.09 times faster, for low conductivity plates. Thus, the influence of radiation on the bulk homogeneity significantly grows for the lower thermal diffusivity ratio. The reason is that the temperature values at the interfaces are only marginally affected by radiation for high $\hat{\kappa}_s/\hat{\kappa}_f$ in contrast to low $\hat{\kappa}_s/\hat{\kappa}_f$.

5.3 Turbulence intensities in the bulk

To analyse how radiation affects the turbulence intensities, the vertical profiles of the area-averaged root mean square (rms) velocity fluctuations

$$u_{z,rms} = \sqrt{\langle (u_z - \langle u_z \rangle_t)^2 \rangle_t} \tag{5.1}$$

and rms temperature fluctuations

$$T_{rms} = \sqrt{\langle (T - \langle T \rangle_t)^2 \rangle_t} \tag{5.2}$$

are presented in Figure 5.6 for $Ra = 6.3 \times 10^7$ and $\hat{\kappa}_s/\hat{\kappa}_f = 0.003$. They reveal that thermal radiation damps the temperature and velocity fluctuations in the entire convection cell. The latter is explained with the help of Figure 5.7, which displays the effective temperature difference between the interfaces for both radiation scenarios. It shows that ΔT_{eff} decreases due to radiation. Consequently, the buoyancy force is smaller, thermal plumes decelerate, and hence the temporal velocity and temperature fluctuations decrease.

The stabilising effect of surface radiation on Rayleigh–Bénard convection was also observed in steady 2D (Ridouane et al. 2004; Gad and Balaji 2010) and 3D (Lan et al. 2003; Xu et al. 2007) flow simulations. Since the cited papers focused on the influence of thermal radiation on the onset of convection, they

referred the stabilising effect of radiation to the growth of the critical Rayleigh number. Furthermore, Lan et al. (2003) scaled this growth with the increase in the optical thickness of the radiatively participating fluid, while Ridouane et al. (2004) noticed that an increase in the walls' emissivity increases the side walls' temperature, and hence the critical *Ra*. All in all, the present study reveals an-

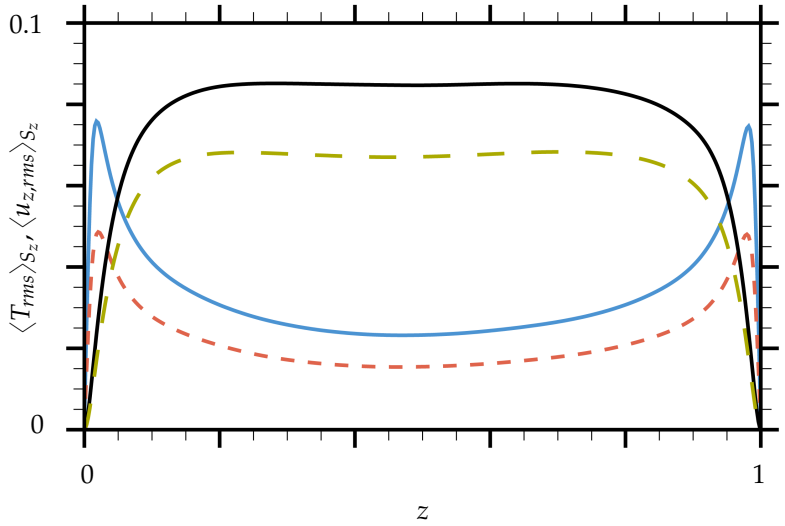

FIGURE 5.6: The vertical profile of $\langle T_{rms}\rangle_{S_z}$ (—, - - -) and $\langle u_{z,rms}\rangle_{S_z}$ (—, - - -) in the absence of radiation (solid lines) and in the presence of radiation (dashed lines) for $Ra = 6.3 \times 10^7$ and $\hat{\kappa}_s/\hat{\kappa}_f = 0.003$.

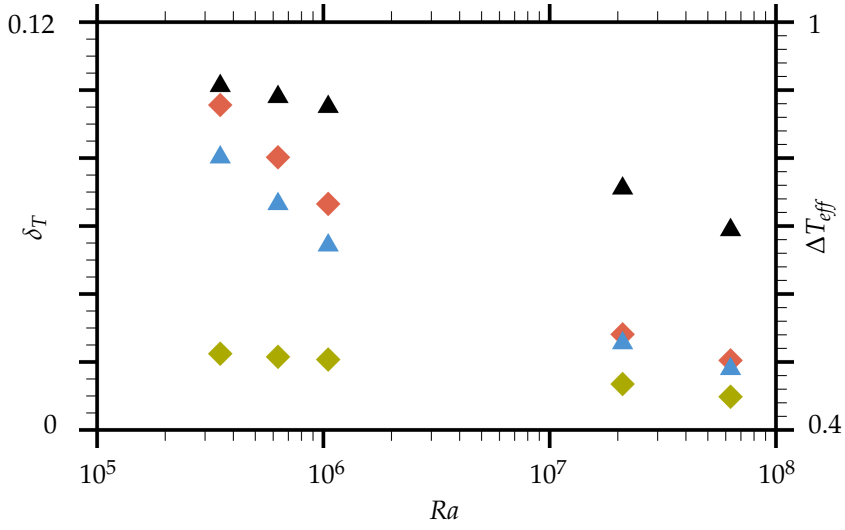

FIGURE 5.7: Thermal boundary layer thickness δ_T in the absence of radiation (▲) and in the presence of radiation (◆) for $\hat{\kappa}_s/\hat{\kappa}_f = 0.003$ versus *Ra*. Additionally, the effective temperature difference ΔT_{eff} in the absence of radiation (▲) and in the presence of radiation (◆) for $\hat{\kappa}_s/\hat{\kappa}_f = 0.003$ versus *Ra*.

other possible stabilising mechanism, namely, a decrease in ΔT_{eff} evoked by the change of the temperatures at the interfaces.

Figure 5.6 further reveals that the radiation-induced differences of T_{rms} are greater at the edge of the BL than in the bulk. Moreover, the differences between $u_{z,rms}$ obtained in the two radiation scenarios are greater in the bulk region than close to the walls, where they eventually vanish. In other words, radiation most alters the turbulent fluctuations at their maxima. There, the temperature fluctuations are caused by the detaching thermal plumes, and the velocity fluctuations are caused by intense mixing.

In order to study how the intensity of the turbulent fluctuations in the bulk change with the Rayleigh number, the area-averaged values of T_{rms} and $u_{z,rms}$ evaluated at $z = 0.5H$ for various Ra and both radiation scenarios are presented in Figure 5.8.

Putting $\hat{\kappa}_s/\hat{\kappa}_f = 0.003$, the difference between the $\langle T_{rms} \rangle_{S_{z=0.5H}}$ obtained in the two radiation scenarios decreases by a factor of 2.44 if the Rayleigh number is increased from $Ra = 3.5 \times 10^5$ to $Ra = 6.3 \times 10^7$. Analogously, the difference between $\langle u_{z,rms} \rangle_{S_{z=0.5H}}$ decreases by a factor of 1.51. The above can be interpreted with the help of Figure 5.7, which reveals that the difference between ΔT_{eff} in the absence and presence of radiation also decreases with increasing Ra. Thus, the effective Rayleigh numbers calculated for each radiation scenario are closer to each other for higher Rayleigh numbers. Since Ra_{eff} determines the convective motion, the turbulent fluctuations in the bulk are also closer to each other for both radiation scenarios and higher Rayleigh numbers.

Moreover, Figure 5.8a discloses that the temperature fluctuations are almost constant for both radiation scenarios up to $Ra = 1.05 \times 10^6$. A further increase in Ra leads to a decrease in $\langle T_{rms} \rangle_{S_{z=0.5H}}$. This reduction is observed because the increased turbulence level improves mixing of the fluid in the bulk, and consequently the temperatures in the bulk are more uniform in time and space. This is in agreement with Verzicco and Sreenivasan (2008), who found that T_{rms} decreases in the bulk with increasing Ra for isothermal or constant heat flux BCs.

Figure 5.8 can be further used to examine the influence of the thermal diffusivity ratio on the turbulent fluctuations in the bulk. It can be seen that the temperature and velocity fluctuations predicted for $\hat{\kappa}_s/\hat{\kappa}_f = 3.8$ and any considered Ra in the absence of radiation coincide with the corresponding ones obtained in the presence of radiation. Thus, when high conductivity plates are employed, the turbulent fluctuations are not affected by radiation for any considered Ra. Nevertheless, increasing the thermal diffusivity ratio from $\hat{\kappa}_s/\hat{\kappa}_f = 0.003$ to $\hat{\kappa}_s/\hat{\kappa}_f = 3.8$ increases the turbulence intensities independently of Ra and of the radiation scenario. For example, the temperature fluctuations $\langle T_{rms} \rangle_{S_{z=0.5H}}$ increase in the presence of radiation by a factor of 2.08 for $Ra = 6.3 \times 10^7$, while $\langle u_{z,rms} \rangle_{S_{z=0.5H}}$ increases by 54%. This behaviour is in contrast to the findings

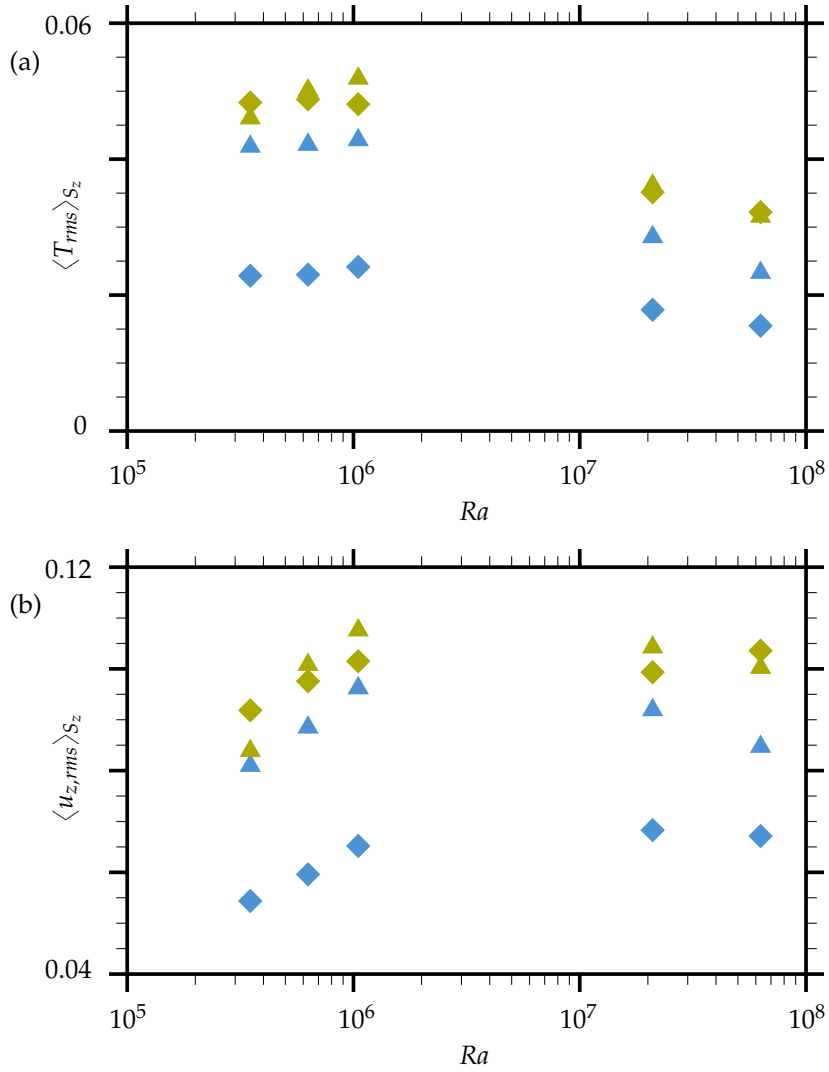

FIGURE 5.8: Rms fluctuations of the temperature $\langle T_{rms} \rangle_{S_z}$ (a) and the vertical velocity component $\langle u_{z,rms} \rangle_{S_z}$ (b) in the absence of radiation (delta symbols) and in the presence of radiation (diamond symbols) for $\hat{\kappa}_s/\hat{\kappa}_f = 0.003$, $z = 0.5H$ (blue symbols) and $\hat{\kappa}_s/\hat{\kappa}_f = 3.8$, $z = 0.5H$ (green symbols).

of Hunt et al. (2003), who found no clear dependence of the u_z variations in the bulk on the thermal diffusivity ratio.

5.4 Boundary layer thickness

When low conductivity plates are employed, the decrease in ΔT_{eff} due to radiation not only reduces the intensity of the turbulent fluctuations but also decreases the effective Rayleigh number Ra_{eff}. Since it is well known that in

the absence of radiation the decrease of the Rayleigh number is associated with a retreat of the convective bulk and the growth of the thermal boundary layer thickness δ_T (see, e.g. Kaczorowski and Wagner 2009), it is of interest to examine how the radiation-induced drop in Ra_{eff} affects δ_T. To this end, the thermal boundary layer thickness determined according to Belmonte et al. (1994) by extracting the position of the peak of $\langle T_{rms} \rangle_{S_z}$ is plotted in Figure 5.7. Since the drop in Ra_{eff} is proportional to the drop in ΔT_{eff}, the latter is used in the analysis and is also shown in Figure 5.7.

Considering $Ra = 3.5 \times 10^5$, the thermal BL thickness grows due to radiation by 19% while the effective temperature difference decreases by 77%. Moreover, the decrease in ΔT_{eff} and the resulting increase in δ_T is reduced for higher Rayleigh numbers. Eventually, for $Ra = 6.3 \times 10^7$, radiation increases δ_T by 14% while ΔT_{eff} drops by 55%.

The radiation-induced increase in δ_T was also reported for $Ra \leqslant 10^6$ by Akiyama and Chong (1997), who performed 2D simulations of a square enclosure heated from the left and cooled from the right assuming all the walls to be grey bodies. However, while in their study the growth of the BL thickness was caused by the change of the temperature at the adiabatic horizontal walls, in the present research these walls are modelled with finite diffusivity.

6

RADIATION EFFECTS ON THE TEMPERATURE AT THE ACTIVE WALLS

6.1 Alteration of the temperature distributions at the solid–fluid interfaces

Studying turbulent convection in a cylindrical Rayleigh–Bénard cell with isothermally heated and cooled walls, Wagner and Shishkina (2013) observed that the large-scale circulation leaves its footprints on the adiabatic side wall. Examining the flow in a rectangular box with plates with a small diffusivity, Hunt et al. (2003) found that in regions where small scale structures (puffs) are formed, the spatial variation of the surface temperature is of the order of the scale of the puffs. In the present study, the temperature distributions evaluated at the interfaces for $Ra = 6.3 \times 10^7$ and $\hat{\kappa}_s/\hat{\kappa}_f = 0.003$ in Figure 6.1 also show that the LSC leave their footprints on the solid–fluid interfaces. The same holds true for high conductivity plates, though the horizontal temperature gradients are very small.

Although the differences resulting from different BCs, such as constant heat flux, isothermal or conductive plates, have been studied in the past (Hunt et al. 2003; Brown et al. 2005; Verzicco 2004; Verzicco and Sreenivasan 2008; Johnston and Doering 2009; Wittenberg 2010; Czarnota and Wagner 2011b, 2013), the influence of convection and radiation on the active plates has not been addressed so far. To do so, the areal probability density function PDF_{S_z} of the temperature, which corresponds to the time-averaged temperature distribution at the interfaces (Figure 6.1), is plotted in Figure 6.2. Considering the bottom interface in the absence of radiation, the $PDF_{S_{z=0}}$ is characterised by a double peak with equal maximum values. But in the presence of radiation, a triple peak is obtained.

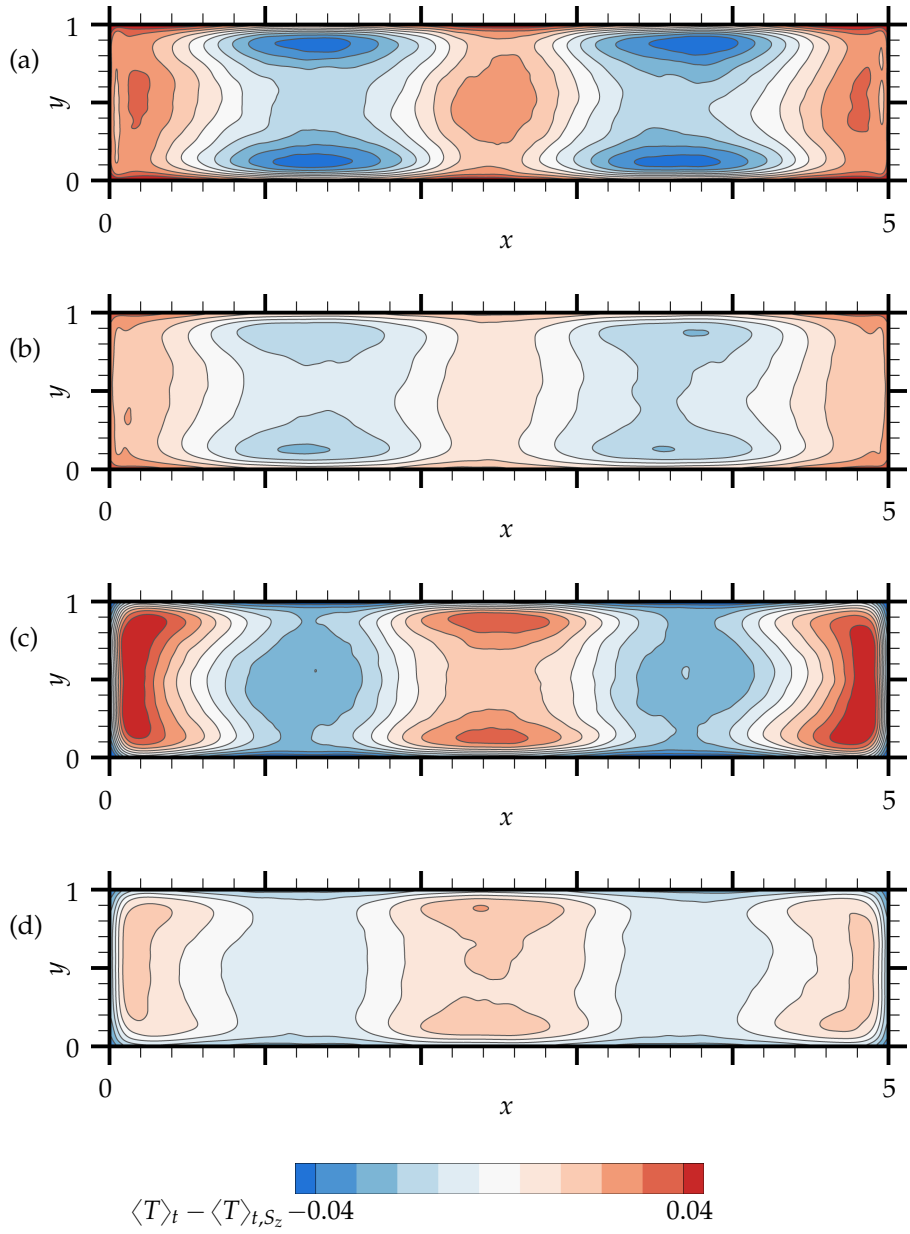

FIGURE 6.1: A horizontal cross-section showing the distribution of $\left(\langle T\rangle_t - \langle T\rangle_{t,S_z}\right)$ for $Ra = 6.3 \times 10^7$ and $\hat{\kappa}_s/\hat{\kappa}_f = 0.003$ at $z = 0$ (a, b) and $z = 1$ (c, d) in the absence of radiation (a, c) and in the presence of radiation (b, d).

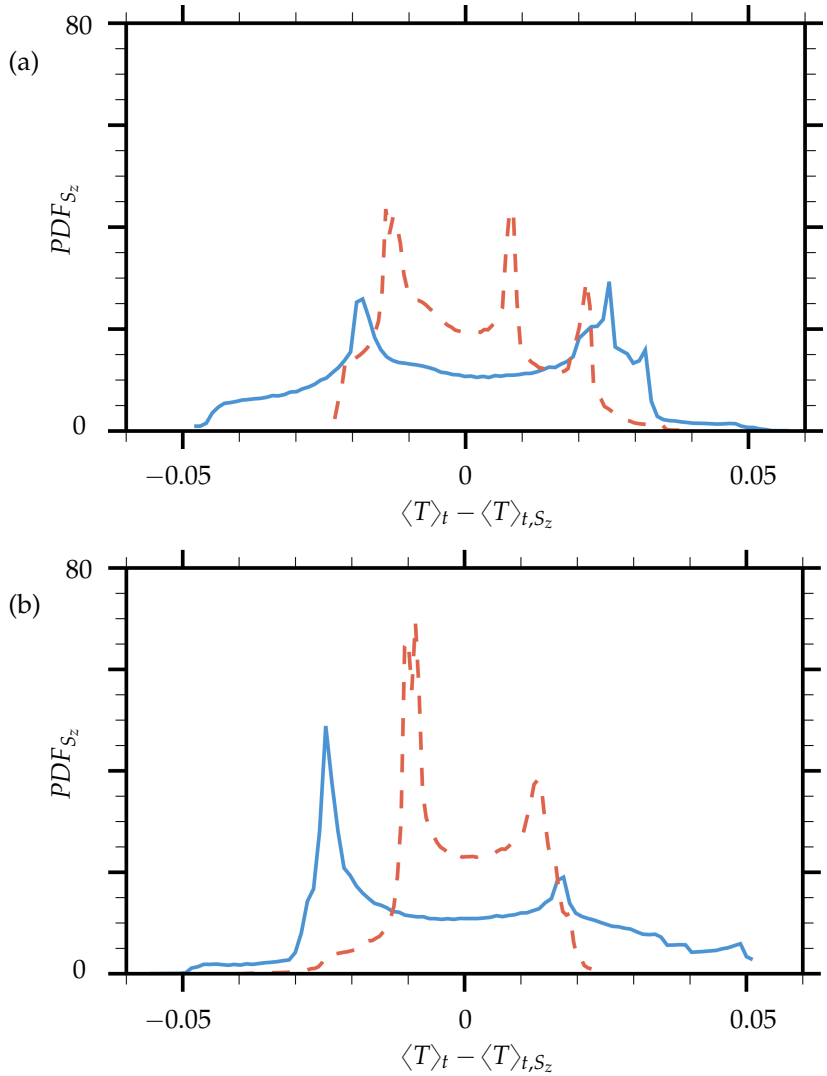

FIGURE 6.2: The areal probability density function (PDF_{S_z}) of $\left(\langle T\rangle_t - \langle T\rangle_{t,S_z}\right)$ for $Ra = 6.3 \times 10^7$ and $\hat{\kappa}_s/\hat{\kappa}_f = 0.003$ at $z = 0$ (a) and $z = 1$ (b) in the absence of radiation (—) and in the presence of radiation (- - -).

To relate each peak of $PDF_{S_{z=0}}$ to a region at the bottom interface, it is helpful to take a look at the distributions of the temperature at the interface in the absence and presence of radiation (Figures 6.1a–6.1b) and relate the differences between these distributions, which occur in certain temperature ranges, to the temperature of the PDF's peaks (Figure 6.2a). In the absence of radiation there is only one peak in the range of positive temperature variations, which reflects the temperature variations of all hot regions at the bottom interface. On the other hand, in the presence of radiation there are two peaks in the range of positive temperature variations. The higher one, for temperature variations

slightly above $\langle T \rangle_{t,S_{z=0}}$, is linked to the centre of the bottom interface. There, the temperature variations are reduced most by radiation. The lower peak reflects the warmest plumes and is related to the high temperatures close to the lateral widthwise walls, where the temperature drop due to radiation is moderate. Thus, the temperatures at the bottom interface, and hence the flow structures, are not uniformly affected by radiation. On the contrary, there is only one peak in the range of negative temperature variations in the absence and presence of radiation. This shows that radiation affects equally all regions in which cold plumes reach the bottom interface.

The same analysis is performed for the top interface. Here, in the absence and presence of radiation, the temperature density distribution, shown in Figure 6.2b, has two peaks with different maximum values. In both radiation scenarios, the higher peak of the $PDF_{S_{z=1}}$ profiles is associated with cold plumes generated in two large cold regions. Thus, the coldest regions at the top interface, and hence the cold flow structures, are uniformly altered by radiation. On the other hand, although each radiation scenario discloses a lower peak, which represents the hot plumes arriving at the top plate, the tail of $PDF_{S_{z=1}}$, which reflects the temperature values far above $\langle T \rangle_{t,S_{z=1}}$, disappears in the presence of radiation. This happens because warm regions close to the side walls receive less radiant heat than colder (although still warm) regions in the centre of the top interface. Hence, the temperature of every hot spot at the top interface has a similar temperature.

In order to examine whether this is also true for smaller Ra and $\hat{\kappa}_s/\hat{\kappa}_f = 3.8$, the horizontal profiles of the temperature evaluated at the bottom interface for $Ra < 6.3 \times 10^7$ are plotted in Figure 6.3 for both thermal diffusivity ratios. They reveal that in the absence of radiation, the peak values which correspond to the positive temperature variations are similar, while in the presence of radiation the temperatures close to the side walls are always higher than the ones in the centre. In contrast, the peak values which correspond to the negative temperature variations are similar, regardless of which radiation scenario holds.

Based upon the above analysis, it can be concluded that the temperatures of the cold regions, and hence the cold plumes which leave their footprints on the interfaces, are equally altered by radiation. In contrast, the change of the temperatures of the hot regions and the hot plumes varies with their position, i.e. there is a stronger influence in the centre than close to the widthwise side walls. Moreover, this behaviour holds true for any of the Rayleigh numbers and thermal diffusivity ratios studied here.

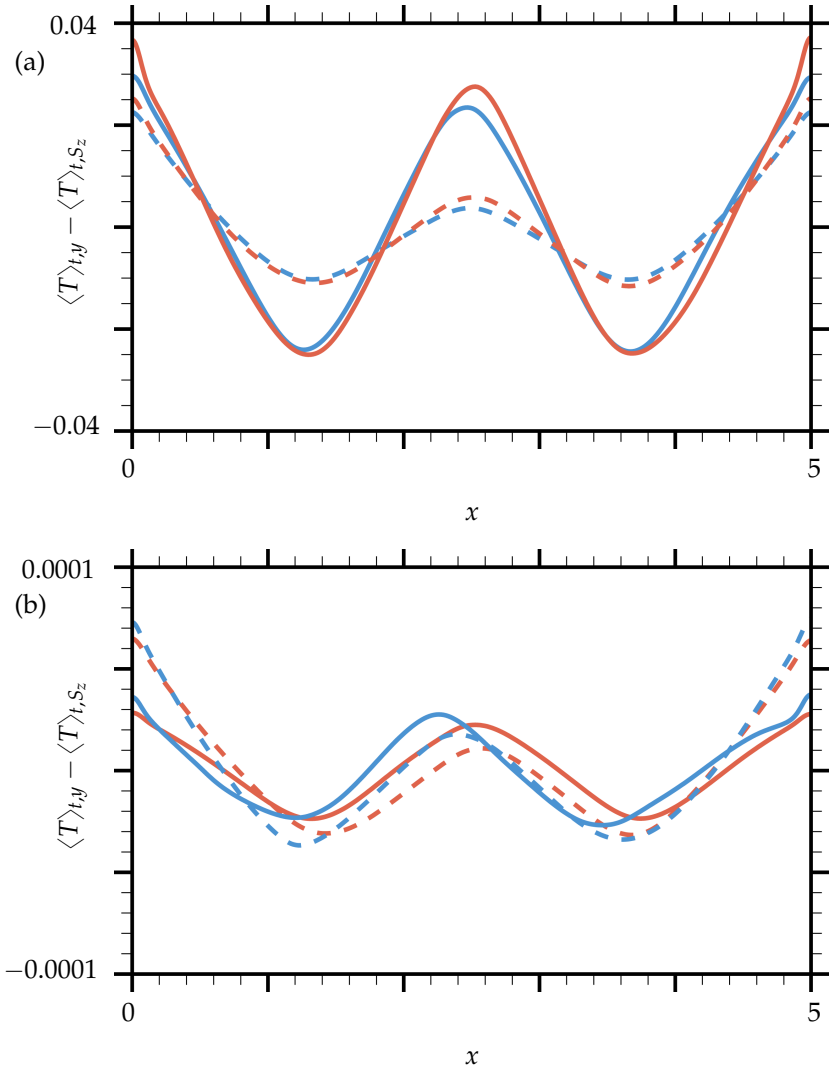

FIGURE 6.3: The time- and line-averaged profiles of the temperatures at $z = 0$ for $\hat{\kappa}_s/\hat{\kappa}_f = 0.003$ (a) and $\hat{\kappa}_s/\hat{\kappa}_f = 3.8$ (b) in the absence of radiation (solid lines) and in the presence of radiation (dashed lines); $Ra = 3.5 \times 10^5$ (blue lines), $Ra = 1.05 \times 10^6$ (red lines).

6.2 Mean temperatures at the solid–fluid interfaces

In order to extend the analysis to higher thermal diffusivity ratios and lower Rayleigh numbers, the time- and area-averaged temperatures $\langle T\rangle_{t,S_z}$ evaluated at both interfaces are plotted in Figure 6.4.

Considering low conductivity plates, $\langle T\rangle_{t,S_z}$ at the bottom interface drops due to radiation by 43% for $Ra = 3.5 \times 10^5$ and rises at the top interface by 43% as well. These temperature changes increase the temperature gradients across

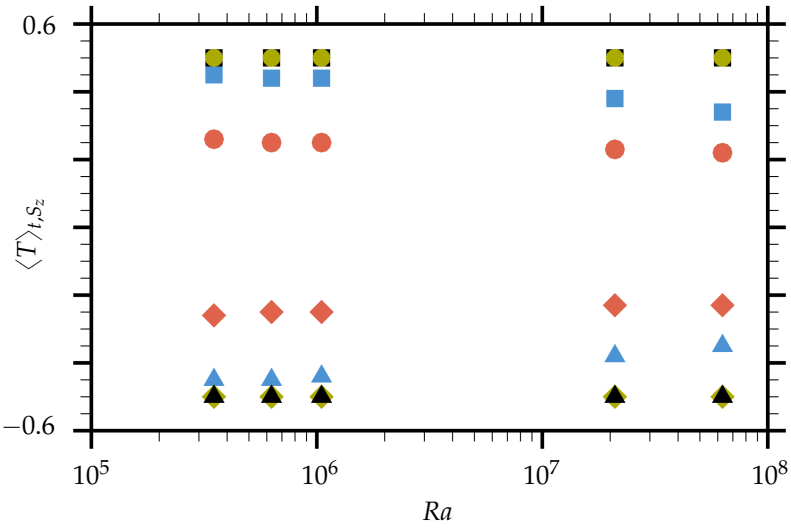

FIGURE 6.4: The time- and area-averaged temperatures $\langle T \rangle_{t,S_z}$ in the absence of radiation at $z = 0$ for $\hat{\kappa}_s/\hat{\kappa}_f = 0.003$ (■), $\hat{\kappa}_s/\hat{\kappa}_f = 3.8$ (■) and at $z = 1$ for $\hat{\kappa}_s/\hat{\kappa}_f = 0.003$ (▲), $\hat{\kappa}_s/\hat{\kappa}_f = 3.8$ (▲) and in the presence of radiation at $z = 0$ for $\hat{\kappa}_s/\hat{\kappa}_f = 0.003$ (●), $\hat{\kappa}_s/\hat{\kappa}_f = 3.8$ (●) and at $z = 1$ for $\hat{\kappa}_s/\hat{\kappa}_f = 0.003$ (◆), $\hat{\kappa}_s/\hat{\kappa}_f = 3.8$ (◆).

the plates, and hence provide the heat for radiation.

Furthermore, for $Ra = 6.3 \times 10^7$, the mean temperatures $\langle T \rangle_{t,S_z}$ are 35% lower (higher) at the bottom (top) interface in the presence of radiation than they are in the absence of radiation. Thus, the change in $\langle T \rangle_{t,S_z}$ induced by radiation decreases with increasing Rayleigh number. The reason is that the temperatures at the bottom interface decrease much faster with increasing Rayleigh number in the absence of radiation than in its presence. The latter is subject to different scaling relations of the total heat transfer with Ra for both radiation scenarios. In the absence of radiation, the temperatures at the interfaces determine the convective Nusselt number, which is proportional to $Ra^{\mathscr{B}}$. Thus, the temperatures at the interfaces change significantly. On the other hand, in the presence of radiation the total heat transfer grows with Ra moderately (discussed in detail in Chapter 7), and hence the changes of the temperatures at the interfaces are small.

Considering high conductivity plates, Figure 6.4 shows that radiation does not substantially alter $\langle T \rangle_{t,S_z}$ at any interfaces, independently of the Rayleigh number. The reason is the very high conductivity of the solid plates, which supports a high conductive heat transport through the plates even when the temperature change at the interfaces is negligibly small.

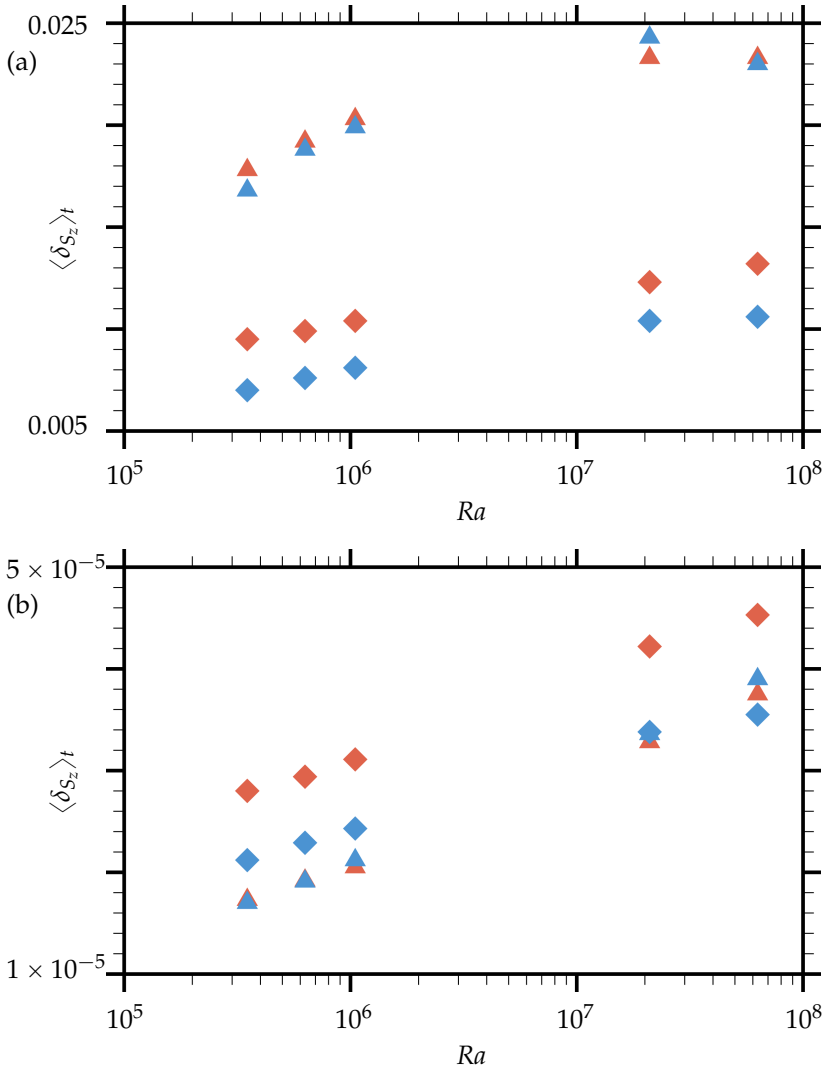

FIGURE 6.5: The time-averaged areal deviations of the temperature $\langle \delta_{S_z} \rangle_t$ for $\hat{\kappa}_s/\hat{\kappa}_f = 0.003$ (a) and $\hat{\kappa}_s/\hat{\kappa}_f = 3.8$ (b); in the absence of radiation (delta symbols) and in the presence of radiation (diamond symbols) at $z = 0$ (red symbols) and $z = 1$ (blue symbols).

6.3 Spatial temperature variations at the solid–fluid interfaces

An important quantity, which differentiates between the different types of interface conditions, is the time-averaged areal deviation of the temperature

$$\langle \delta_{S_z} \rangle_t = \left\langle \sqrt{\langle (T - \langle T \rangle_{S_z})^2 \rangle_{S_z}} \right\rangle_t . \tag{6.1}$$

Figure 6.5a shows the values of $\langle \delta_{S_z} \rangle_t$ evaluated at both interfaces for low

conductivity plates, both in the absence and presence of radiation. It is visible that radiation decreases $\langle \delta_{S_z} \rangle_t$ at the bottom interface by 47% for $Ra = 3.5 \times 10^5$. Thus, radiation renders the temperature at the interface more uniform. The reason is that the hottest regions, e.g. in the centre of the interface, are colder due to radiative heat loss. Additionally, the cold regions are warmer thanks to the descending plumes which are warmed by the radiation at the top interface.

Figure 6.5a further reveals that in the presence of radiation and $Ra = 3.5 \times 10^5$, $\langle \delta_{S_z} \rangle_t$ is 26% smaller at the top interface than at the bottom one, although in the absence of radiation the values of $\langle \delta_{S_z} \rangle_t$ are similar at the interfaces. Thus, radiation leads to a different homogeneity of the temperature distribution at the top and bottom interfaces. Considering that the PDF of the temperature in Figure 6.2 is multimodal at $z = 0$ and bimodal at $z = 1$, it can be concluded that the symmetry breaking emanates from the hot interface. Moreover, especially the temperatures above $\langle T \rangle_{S_{z=0}}$ are responsible for this event, as they significantly vary along the bottom interface. Finally, the above indicates that the hot plumes generated at the bottom interface are less homogeneous than the cold plumes generated at the top interface.

The dependence of $\langle \delta_{S_z} \rangle_t$ on the Rayleigh number can be extracted from Figure 6.5a. In the presence of radiation, $\langle \delta_{S_z} \rangle_t$ increases at the bottom interface by a factor of 1.4 between $Ra = 3.5 \times 10^5$ and $Ra = 6.3 \times 10^7$. Moreover, an analogous behaviour is observed at the top interface, revealing that the temperature distributions at both interfaces become less homogeneous with increasing Ra. The explanation is that the heat transfer is more convective and less radiative for the higher Ra (as discussed in detail in Section 7.1 of Chapter 7), and consequently hot regions become even hotter in order to produce warmer, more energetic plumes. Analogously, the cold regions become colder, which as a result increases the range of temperatures at the interfaces and hence $\langle \delta_{S_z} \rangle_t$.

In order to study how the homogeneity of the temperature distribution depends on the thermal diffusivity ratio, the temperature deviation $\langle \delta_{S_z} \rangle_t$ obtained at both interfaces for $\hat{\kappa}_s/\hat{\kappa}_f = 3.8$ and $\hat{\kappa}_s/\hat{\kappa}_f = 0.003$ are presented in Figures 6.5b and 6.5a, respectively. If the plates are highly conductive, radiation increases $\langle \delta_{S_z} \rangle_t$ at the bottom interface by 62% for $Ra = 3.5 \times 10^5$. On the other hand, as previously discussed, if the plates have low conductivity, radiation decreases $\langle \delta_{S_z} \rangle_t$ by 47%. Thus, the opposite behaviour is observed for low and high thermal diffusivity ratios. The reason this occurs is because of the non-elliptical and elliptical-like distributions of the radiative heat flux for low and high $\hat{\kappa}_s/\hat{\kappa}_f$, respectively, in combination with the narrow and wide range of the radiative heat flux for low and high $\hat{\kappa}_s/\hat{\kappa}_f$, respectively (discussed in detail in Chapter 7). Consequently, in the case of highly conductive plates, more heat is removed from the

hot regions in the centre of the bottom interface than from the hot regions close to the side walls. This leads to great disproportions between the temperatures of the hot regions at the bottom interface. On the other hand, at the bottom interface of low conductivity plates, nearly the same amount of heat is transferred from any hot spot.

Likewise for $\hat{\kappa}_s/\hat{\kappa}_f = 0.003$, the temperature distribution at the top interface evaluated for $\hat{\kappa}_s/\hat{\kappa}_f = 3.8$ is also more homogeneous than the one at the bottom interface. This is true for any Rayleigh number treated here.

Nevertheless, it is noteworthy that for $\hat{\kappa}_s/\hat{\kappa}_f = 3.8$, the plates are nearly isothermal, since $\langle \delta_{S_z} \rangle_t$ is of the order of 10^{-5}.

6.4 Temporal temperature fluctuations at the solid–fluid interfaces

In order to analyse the time response of the temperature distribution at the interface, the area-averaged rms temperature fluctuations

$$\langle T_{rms} \rangle_{S_z} = \left\langle \sqrt{\langle (T - \langle T \rangle_t)^2 \rangle_t} \right\rangle_{S_z} \tag{6.2}$$

are presented in Figure 6.6a, which shows profiles evaluated at both interfaces for low conductivity plates both in the absence and presence of radiation.

A comparison reveals that radiation decreases the temporal fluctuations at both interfaces by a factor of 1.8 for $Ra = 2.1 \times 10^7$. In order to relate this to the plumes, the $\langle T_{rms} \rangle_{S_z}$ distributions at the interfaces are shown in Figure 6.7 for the same configurations. In the presence of radiation, the rms temperature fluctuations are lower in the centre of the bottom interface and close to its side walls, i.e. where the thermal plumes are formed, than in its absence. There, radiation is responsible for a decrease in the convective heat flux, and hence it takes more time before enough heat is transferred to the fluid. This indicates that plumes emerge more slowly in the presence of radiation than in its absence, which explains why $\langle T_{rms} \rangle_{S_z}$ is lower. Additionally, Figure 6.7 shows that radiation damps the temperature fluctuations in the regions where hot and cold plumes reach the top and bottom interface, respectively. This behaviour is also associated with a lower convective heat transfer in these regions. However, the lower temperatures of the rising plumes, and higher temperatures of the falling plumes, also contribute to this effect.

In order to examine the influence of the thermal diffusivity ratio on $\langle T_{rms} \rangle_{S_z}$, the latter is plotted in Figure 6.6b for $\hat{\kappa}_s/\hat{\kappa}_f = 3.8$ and both radiation scenarios. It is clearly visible that $\langle T_{rms} \rangle_{S_z}$ is not affected by the radiative heat transfer for any of the Rayleigh numbers considered. This is in agreement with Gauthier and

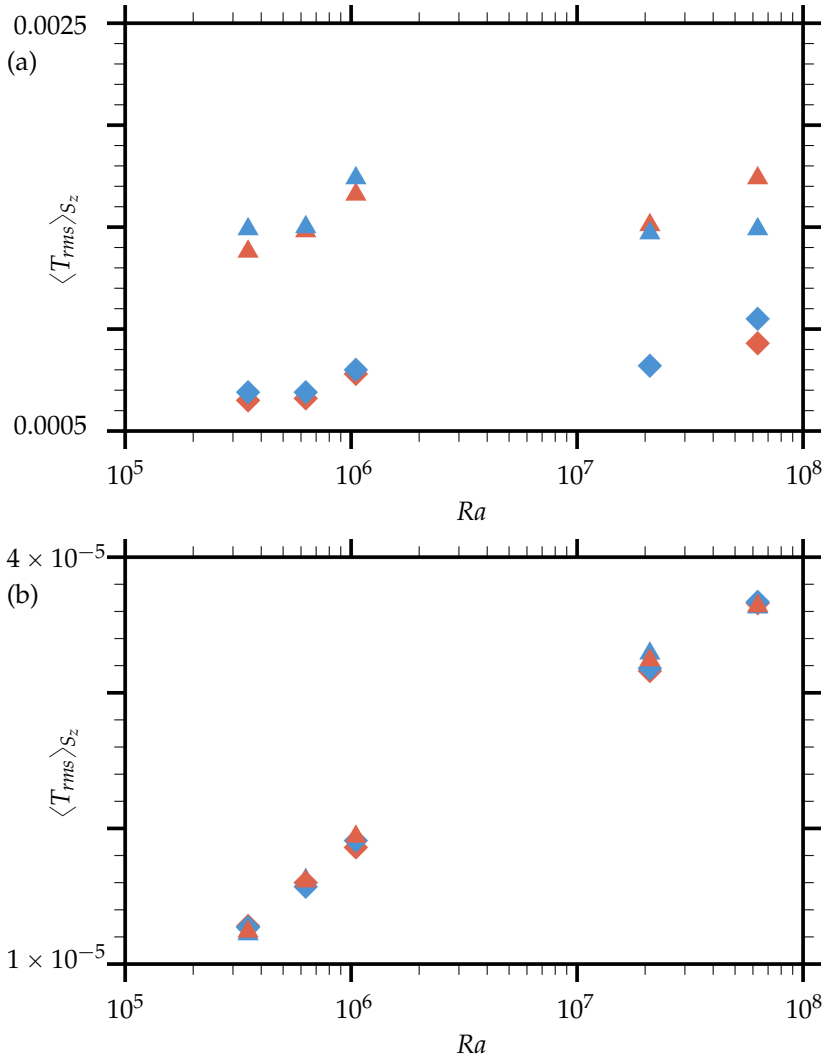

FIGURE 6.6: The area-averaged temperature fluctuations $\langle T_{rms} \rangle_{S_z}$ for $\hat{\kappa}_s/\hat{\kappa}_f = 0.003$ (a) and $\hat{\kappa}_s/\hat{\kappa}_f = 3.8$ (b); in the absence of radiation (delta symbols) and in the presence of radiation (diamond symbols) at $z = 0$ (red symbols) and $z = 1$ (blue symbols).

Roche (2008), who performed experiments with a cylindrical RB cell bounded by highly conductive copper plates. They conjectured that below $Ra \simeq 10^{12}$, the temperature variations at the interfaces resemble a negligible noise.

On the other hand, comparing these values with the ones obtained for $\hat{\kappa}_s/\hat{\kappa}_f = 0.003$ in the presence of radiation (Figure 6.6a) reveals that the temporal fluctuations are two orders of magnitude larger for the lower thermal diffusivity ratio and $Ra = 6.3 \times 10^7$. This holds true also for lower Rayleigh numbers, yet the order of magnitude decreases to one for $Ra = 3.5 \times 10^5$. This is in agreement with Hunt et al. (2003), who studied the influence of various thermal diffusiv-

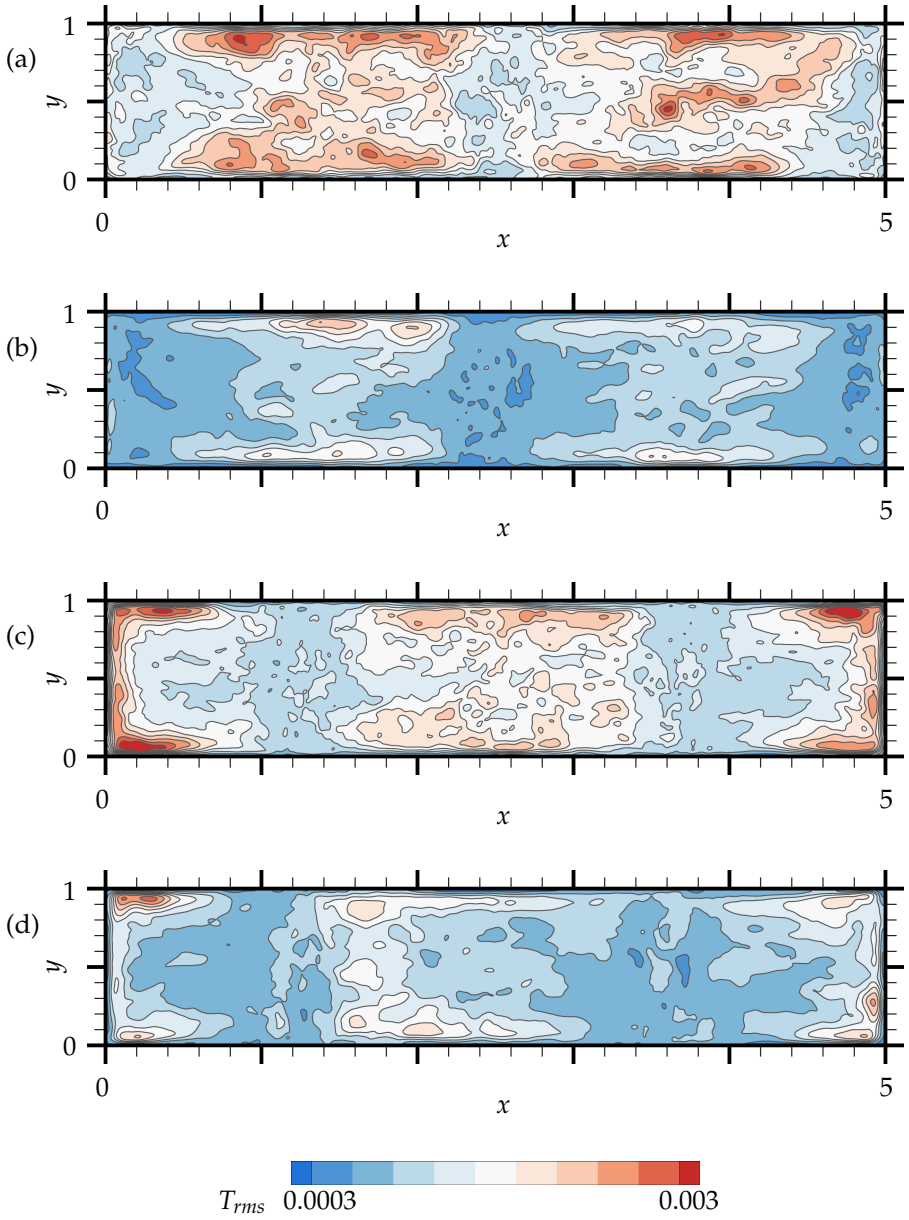

FIGURE 6.7: The distribution of T_{rms} for $Ra = 2.1 \times 10^7$ and $\hat{\kappa}_s/\hat{\kappa}_f = 0.003$ at $z = 0$ (a, b) and $z = 1$ (c, d) in the absence of radiation (a, c) and in the presence of radiation (b, d).

ities of the bottom solid base on the fluid layer under adiabatic BCs at the top plate and periodic ones in the horizontal directions.

7

RADIATION EFFECTS ON THE HEAT TRANSFER

In order to quantify the contributions of convection and radiation to the total heat transfer, which is characterised by the Nusselt number Nu, the latter is split into a convective and radiative contribution:

$$Nu = Nu_c + Nu_r. \tag{7.1}$$

The convective Nusselt number Nu_c is

$$Nu_c = \frac{q_c}{q_{c,f}} = \frac{\hat{u}_z \hat{T} - \hat{\kappa}_f \frac{\partial \hat{T}}{\partial \hat{x}_z}}{\hat{\kappa}_f \hat{\Delta T}/\hat{H}} = \sqrt{RaPr}\, u_z T - \frac{\partial T}{\partial x_z} \tag{7.2}$$

and the radiative Nusselt number

$$Nu_r = Nu_e + Nu_{ir} \tag{7.3}$$

is decomposed into the heat transport due to emission

$$Nu_e = \frac{q_e}{q_{c,f}} = Nr\,(T + \Theta)^4 \tag{7.4}$$

and irradiation

$$Nu_{ir} = \frac{q_{ir}}{q_{c,f}} = Nr\,(T_{out} + \Theta)^4 \left(1 - \sum_{S_j} F_{ij}\right) + Nr \sum_{S_j} \left(T_j + \Theta\right)^4 F_{ij}. \tag{7.5}$$

The first term on the right hand side of (7.5) represents the irradiation originating from the ambient environment which passes through the side walls and

reaches either the bottom interface $Nu_{sw\to b}$ or the top one $Nu_{sw\to t}$. The second term reflects the heat transport due to irradiation originating from either the bottom interface $Nu_{b\to t}$ or the top one $Nu_{t\to b}$. The range of any 2D distribution of the Nusselt number contributions presented in this section will be normalised to obtain a common scale, ranging from 0 to 1. In the case of the convective Nusselt number, it is

$$Nu_c^{norm} = \frac{Nu_c - Nu_c^{min}}{\left| Nu_c^{max} - Nu_c^{min} \right|} \tag{7.6}$$

where c denotes the convective contribution of the Nusselt number and Nu_c^{min} and Nu_c^{max} are the extreme values of Nu_c.

7.1 The total heat transfer and its contributions

In order to study how the total heat transfer is affected by radiation, the total Nusselt numbers obtained in the absence and presence of radiation and for various Rayleigh numbers and low and high thermal diffusivity ratios are plotted in Figure 7.1. It is clearly visible that radiation increases the total Nusselt number for any Rayleigh number and both thermal diffusivity ratios. The growth of the total Nusselt number is induced by the appearance of the radiative heat flux, which, in addition to the convective heat flux, removes heat from the fluid

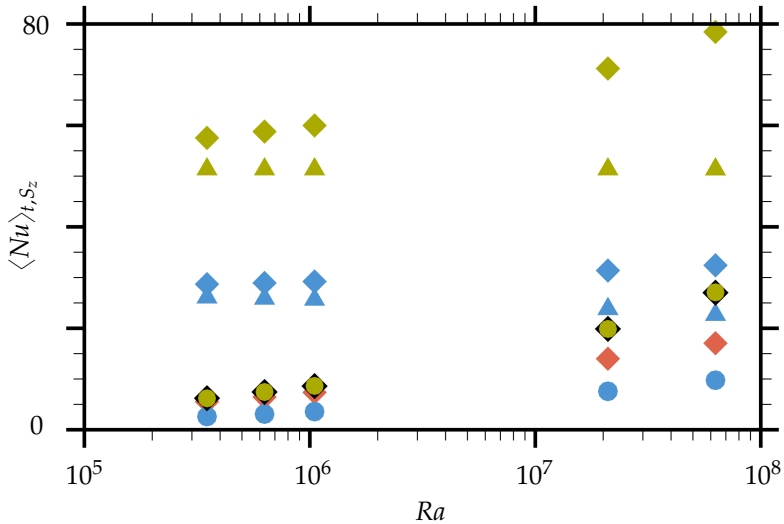

FIGURE 7.1: The time- and area-averaged Nusselt number $\langle Nu \rangle_{t,S_z}$ at $z = 0$ in the absence of radiation, $\hat{\kappa}_s/\hat{\kappa}_f = 0.003$ (◆), $\hat{\kappa}_s/\hat{\kappa}_f = 3.8$ (◆) and in the presence of radiation, $\hat{\kappa}_s/\hat{\kappa}_f = 0.003$ (◆), $\hat{\kappa}_s/\hat{\kappa}_f = 3.8$ (◆) together with its radiative component $\langle Nu_r \rangle_{t,S_z}$ for $\hat{\kappa}_s/\hat{\kappa}_f = 0.003$ (▲) and $\hat{\kappa}_s/\hat{\kappa}_f = 3.8$ (▲), and the convective component $\langle Nu_c \rangle_{t,S_z}$ for $\hat{\kappa}_s/\hat{\kappa}_f = 0.003$ (●) and $\hat{\kappa}_s/\hat{\kappa}_f = 3.8$ (●).

side of the bottom interface. Additionally, heat is conducted from the isothermal outer side of the solid plate towards the bottom interface in accordance with (4.5) and (4.36). Since the heat fluxes at both sides of the solid–fluid interface are equal, the increased heat flux (convective plus radiative) at the fluid side of the bottom interface increases the conductive heat flux in the solid plates. Finally, since the conductive heat flux determines the total Nusselt number, the latter also increases.

7.1.1 Dependence on the thermal diffusivity ratio

Further, in order to investigate how the total heat transfer changes with the control parameter for diffusion $\hat{\kappa}_s/\hat{\kappa}_f$, the time- and area-averaged Nusselt numbers are extracted from Figure 7.1.

In the absence of radiation, the total Nusselt number, which is equal to Nu_c, is 58% lower for $Ra = 6.3 \times 10^7$ when the thermal diffusivity ratio is decreased from $\hat{\kappa}_s/\hat{\kappa}_f = 3.8$ to $\hat{\kappa}_s/\hat{\kappa}_f = 0.003$. When the high conductivity solid plates are replaced by low conductivity ones, the demand for the present total heat flux obeys the Fourier law. Thus, the decrease in the thermal conductivity of the solid plates causes an increase in the temperature difference across the solid plates. This large temperature difference is realised by a large drop in the temperature values at the bottom interface, and vice versa, a large growth of the temperature values at the top interface. As a result ΔT_{eff} is decreased, leading to a lower demand for the total heat flux, and hence Nu_c.

A similar process takes place in the presence of radiation. The total Nusselt number is lower by a factor of 2.4 for a lower thermal diffusivity ratio and $Ra = 6.3 \times 10^7$. Here, the interaction between the conductive plates and the fluid layer causes not only a drop in Nu_c with decreasing $\hat{\kappa}_s/\hat{\kappa}_f$ but also a drop in Nu_r since the total heat flux is the sum of Nu_c and Nu_r (see (7.1)). Moreover, the change of the mean temperature at the interfaces significantly reduces the radiative heat flux, as it depends on the fourth power of the temperature and finally leads to a large reduction of the total heat flux.

7.1.2 Dependence on the Rayleigh number

Likewise, the total heat transfer also depends on the Rayleigh number. In order to better understand this dependence in the presence of radiation, it is necessary to examine the convective and radiative contributions to the total Nu plotted in Figure 7.1. For $Ra = 3.5 \times 10^5$, the radiative heat flux dominates the total heat transfer since Nu_r contributes 89% and 91% to the total Nu for $\hat{\kappa}_s/\hat{\kappa}_f = 3.8$ and $\hat{\kappa}_s/\hat{\kappa}_f = 0.003$, respectively. For higher Ra, the higher buoyancy forces enhance the contribution of Nu_c. Additionally, a decrease in the temperature at the bottom interface damps the contribution of Nu_r since the latter depends on

the fourth power of the temperature, see (7.3)–(7.5). Thus, for $Ra = 6.3 \times 10^7$, the contribution of Nu_r to the total Nu drops to 65% for $\hat{\kappa}_s/\hat{\kappa}_f = 3.8$ and 70% for $\hat{\kappa}_s/\hat{\kappa}_f = 0.003$. All in all, the magnitude of the total heat transfer increases with increasing Ra because a gentle drop in Nu_r is overcompensated for by the increase in Nu_c. However, it is important to understand that the total heat transfer only increases with the Rayleigh number to a certain limit. The reason lies in the fact that by fixing one set of the dimensionless control parameters for radiation and convection, all dimensional quantities are determined. In this respect, Table A1, which collects the dimensional and dimensionless control parameters for simulations with radiation modelling, reveals that an increase in Ra while keeping all the other control parameters constant implies that the height of the RB cell $\hat{H}$ increases, while the dimensional mean bulk temperature $\hat{T}_0$ and the temperature difference between the plates $\Delta\hat{T}$ decreases. Because $\Delta\hat{T}$ and $\hat{T}_0$ have lower limits, Ra has an upper limit, for which the maximal Nu is obtained. For example, for the simulation considered in this section, i.e. for $\Theta = 29$, $Nr = 0.0008$, $Pr = 0.7$ and $\hat{\kappa}_s/\hat{\kappa}_f = 0.003$, Ra can only increase up to $Ra \sim 10^{15}$.

7.2 Interactions between the radiative and convective heat flux

Since radiation renders the convective bulk uniform, as described in Chapter 5, it is clear that there is an interaction between radiation and convection. Moreover, in this research, the fluid is radiatively non-participating, and hence this interaction must originate from the interfaces. Additionally, it is to be expected that the effects of this interaction are only visible when low conductivity plates are employed since, as described in Chapter 5 and 6, a radiation effect on the temperature distribution in the bulk and at the interfaces was only observed for $\hat{\kappa}_s/\hat{\kappa}_f = 0.003$. Thus, the analysis presented below is performed at the interfaces of the low conductivity plates.

7.2.1 Convective drop

The interactions can be identified by analysing the change of the distribution of the convective Nusselt number due to radiation. For this reason, the distribution of the time-averaged Nu_c obtained in the presence of radiation is subtracted from the one obtained in the absence of radiation, and the result is plotted in Figure 7.2. The resulting distribution represents the so-called local convective drop Nu_c^{drop} at the bottom and top interfaces for $Ra = 6.3 \times 10^7$. It can be seen that the local convective drop varies mainly in the lengthwise direction. Therefore, for the quantitative evaluation of Nu_c^{drop}, its time- and widthwise-averaged values are extracted from Figure 7.2. They reveal that the local convective drop varies

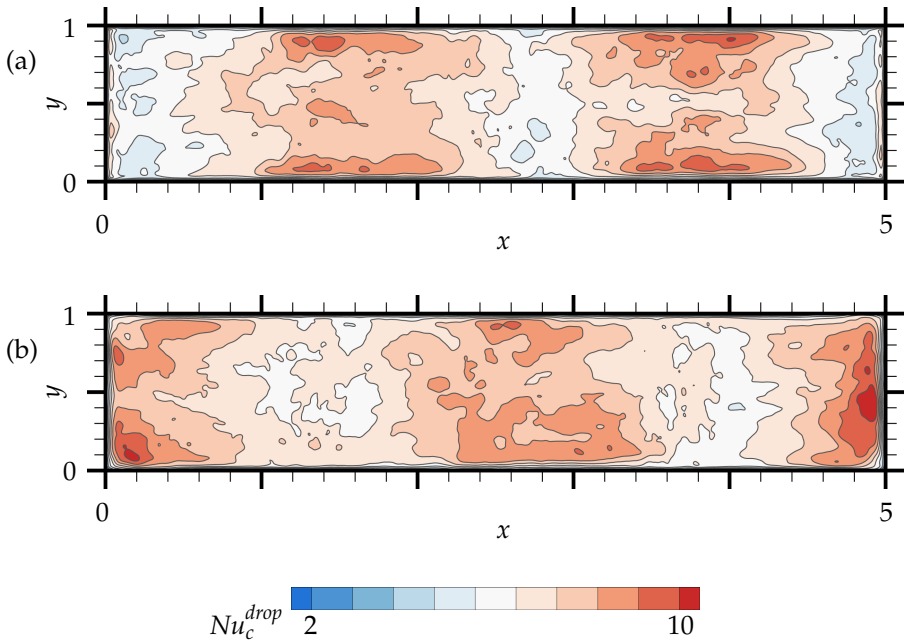

FIGURE 7.2: The distribution of the convective drop obtained from time-averaged Nu_c in the absence and presence of radiation for $Ra = 6.3 \times 10^7$ and $\hat{\kappa}_s/\hat{\kappa}_f = 0.003$ at $z = 0$ (a) and $z = 1$ (b).

along the interfaces up to a factor of 2.5. Furthermore, since radiation does not change the topology of the flow, as discussed in Chapter 5, it is possible to relate the lengthwise variations of the convective drop to the rising and descending plumes by superimposing the temperature distributions from Figure 6.1 on the distributions of the local convective drop in Figure 7.2. This shows that the local convective drop is smaller in regions where plumes develop than in those where plumes arrive at the interfaces. This is due to a combination of two mechanisms.

The first one is directly related to those thermal plumes which arrive at the interfaces, thereby transporting heat (Shang et al. 2003). Thus, the convective heat flux drops at locations where they impinge. For the sake of clarity, the explanation is limited only to hot plumes, which rise from the centre of the bottom interface and reach the centre of the top one. Since the temperature at the bottom interface is decreased by radiation (see Chapter 6), the rising plumes are colder and less energetic. Therefore, plumes which arrive at the top interface carry less heat and decrease the convective heat flux there compared to what it would be in the absence of radiation.

The second mechanism is directly related to the distribution of the radiative heat flux plotted in Figures 7.3b and 7.3d. Due to the radiative heat flux, the temperature at the entire bottom interface decreases and increases at the top

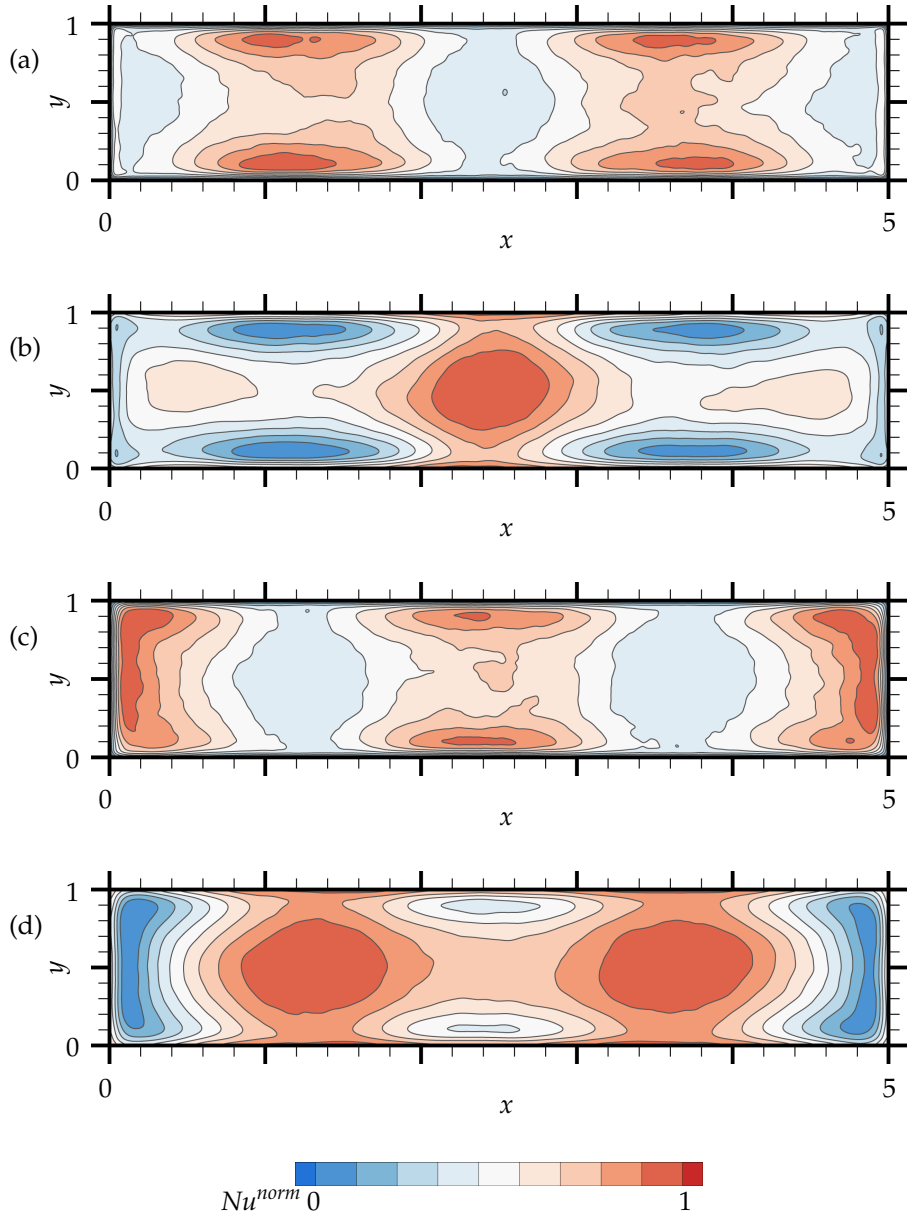

FIGURE 7.3: The distribution of the normalised time-averaged Nusselt number components in the presence of radiation for $Ra = 6.3 \times 10^7$ and $\hat{\kappa}_s/\hat{\kappa}_f = 0.003$ at $z = 0$ (a, b) and $z = 1$ (c, d). Nu_c^{norm} (a, c), Nu_r^{norm} (b, d). Normalisation obtained from $Nu_c^{min} = 2.98$, $Nu_c^{max} = 15.04$, $Nu_r^{min} = 20.92$, $Nu_r^{max} = 24.43$ at $z = 0$ and $Nu_c^{min} = 2.59$, $Nu_c^{max} = 15.15$, $Nu_r^{min} = 19.74$, $Nu_r^{max} = 24.44$ at $z = 1$.

interface. Consequently, the temperature difference between the interface and the impinging plumes as well as between the interface and the emerging ones decreases. Therefore, the local convective drop occurs along the entire bottom and top interfaces. Additionally, Figure 7.2a reveals that Nu_c^{drop} is greater in the centre of the bottom interface than close to the widthwise walls, although thermal plumes are formed in both regions. Hence, the first mechanism, i.e. the descending cold plumes, can not be responsible for this variation in Nu_c^{drop}. In order to explain this, the distribution of Nu_r (Figure 7.3b) is superimposed on the distribution of Nu_c^{drop} in Figure 7.2a, and it turns out that the local convective drop changes with the value (intensity) of the radiative heat flux. Quantitatively speaking, for $Ra = 6.3 \times 10^7$, the radiative heat flux, which is 8% greater in the centre of the bottom interface than close to the widthwise walls, leads to a 16% greater convective drop in the centre than close to the walls.

To sum up, in regions where plumes emerge, only the second mechanism, i.e. the radiative heat flux and its intensity, is responsible for the local convective drop, while in regions where plumes impinge, the first mechanism, i.e. the convective heat transported by arriving plumes, contributes as well. Furthermore, the local convective drop is smaller in regions where only the second mechanism takes place than in regions where both mechanisms contribute.

This analysis provides new insight into the physical interpretation of the spatially dependent interactions between radiation and convection since other studies (Akiyama and Chong 1997; Balaji and Venkateshan 1993; Gad and Balaji 2010; Ridouane et al. 2004) address no more than the role of the radiative heat flux in the mean convective drop.

Thanks to the local convective drop, which depends on the location, the spatial variations in the convective heat flux are approximately 31% smaller in the presence of radiation than in its absence. Therefore, the distribution of Nu_c is levelled, and hence the vertical temperature gradient at the interfaces better resembles the constant heat flux boundary conditions in the presence of radiation than in its absence.

In order to investigate how the convective drop depends on the Rayleigh number, it is convenient to work with the mean convective drop instead of the local one. Thus, $\langle Nu_c^{drop} \rangle_{t,S_z}$ is extracted from the data of Figure 7.1 for all considered Rayleigh numbers, by subtracting the time- and area-averaged convective Nusselt number in the presence of radiation from the one in the absence of radiation. As expected, for high conductivity plates, i.e. $\hat{\kappa}_s/\hat{\kappa}_f = 3.8$, the magnitude of the mean convective drop is close to zero independently of the Rayleigh number. On the other hand, for low conductivity plates, i.e. $\hat{\kappa}_s/\hat{\kappa}_f = 0.003$, the mean convective drop increases logarithmically from 2.9 for $Ra = 3.5 \times 10^5$ to 7.3 for $Ra = 6.3 \times 10^7$. The logarithmic shape, which represents the decreas-

ing increment of $\langle Nu_c^{drop} \rangle_{t,S_z}$, is obtained because Nu_r and ΔT_{eff}, which drive the convective drop, decrease with increasing Ra. On the other hand, the magnitude of the mean convective drop continuously grows with Ra because Nu_c grows enormously with Ra, and hence even a little decrease in ΔT_{eff} still leads to a significant drop in the convective heat flux.

Since the mean convective drop was also found in a square RB cell (Gad and Balaji 2010) and a square cavity heated and cooled from the sides (Akiyama and Chong 1997), it is of interest to examine whether the one obtained in the present study for $\hat{\kappa}_s/\hat{\kappa}_f = 0.003$ is of a similar order. While a mean convective drop $\langle Nu_c^{drop} \rangle_{t,S_z} = 0.5$ was reported by Gad and Balaji (2010) for $Ra = 1.05 \times 10^5$ and wall emissivity $\varepsilon = 0.85$, Akiyama and Chong (1997) obtained $\langle Nu_c^{drop} \rangle_{t,S_z} = 0.3$ for $Ra = 1 \times 10^6$, $\Theta = 29.35$ and blackbody walls ($\varepsilon = 1$). In the present study, a higher drop in the convective heat flux $\langle Nu_c^{drop} \rangle_{t,S_z} = 3.8$ is observed for a Rayleigh number $Ra = 1.1 \times 10^6$ and low conductivity plates. The reason for this higher value is that the Nusselt number calculation is based on the temperature difference between the outer sides of the solid plates, i.e. ΔT, (see (7.2)), while in the literature, the temperature difference between the isothermal walls, i.e. ΔT_{eff}, is used. Therefore, renormalizing Nu according to $Nu_{eff} = Nu\Delta T/\Delta T_{eff}$ decreases the mean convective drop from 3.8 to 1.3. The obtained value is similar to the one reported in previous studies, although Gad and Balaji (2010) and Akiyama and Chong (1997) used different BCs.

7.2.2 Correlation between the convective and radiative Nusselt number

Owing to the increase in the local convective drop with increasing intensity of the radiative heat flux, it is to be expected that Nu_c and Nu_r are correlated in time and space for $\hat{\kappa}_s/\hat{\kappa}_f = 0.003$. Although for $\hat{\kappa}_s/\hat{\kappa}_f = 3.8$ the magnitude of the mean convective drop is close to zero, the radiation and convection can still be correlated. Thus, the correlation between Nu_c and Nu_r, obtained from the same simulation, is analysed in time and space for $\hat{\kappa}_s/\hat{\kappa}_f = 0.003$ and $\hat{\kappa}_s/\hat{\kappa}_f = 3.8$. For the sake of simplicity, the correlation is analysed only for $Ra = 6.3 \times 10^7$, but the discussion is extended to another Ra in Chapter 8.

Correlation in time.
In order to measure the correlation in time, the correlation coefficient r is calculated from the entire time history of the area-averaged convective and radiative Nusselt number evaluated at the bottom interface. Time frames of these signals are plotted in Figure 7.4. Since the correlation coefficient

$$r = \frac{n\sum Nu_c Nu_r - (\sum Nu_c)(\sum Nu_r)}{\sqrt{n(\sum Nu_c^2) - (\sum Nu_c)^2}\sqrt{n(\sum Nu_r^2) - (\sum Nu_r)^2}} \tag{7.7}$$

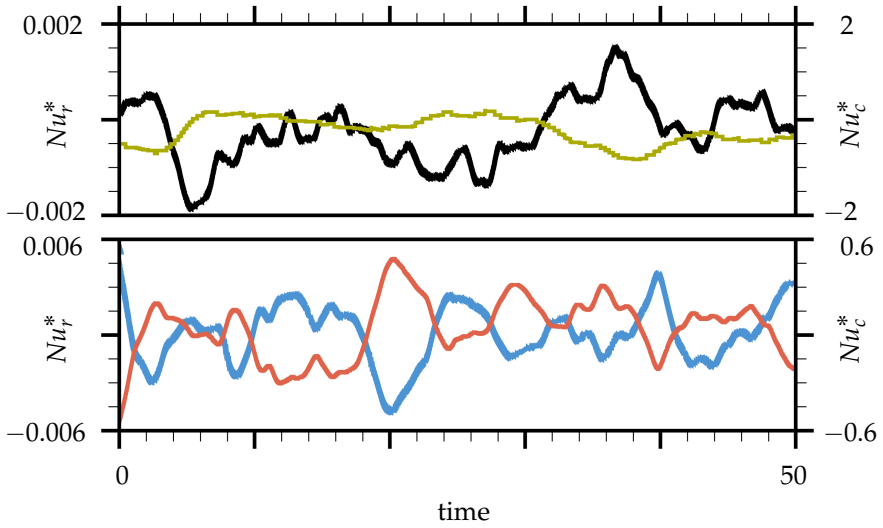

FIGURE 7.4: The time history of the Nusselt number components in the presence of radiation at $z = 0$ for $Ra = 6.3 \times 10^7$; $Nu_c^* = \langle Nu_c \rangle_{S_z} - \langle Nu_c \rangle_{t,S_z}$ and $\hat{\kappa}_s/\hat{\kappa}_f = 0.003$ (—), $\hat{\kappa}_s/\hat{\kappa}_f = 3.8$ (—); $Nu_r^* = \langle Nu_r \rangle_{S_z} - \langle Nu_r \rangle_{t,S_z}$ and $\hat{\kappa}_s/\hat{\kappa}_f = 0.003$ (—), $\hat{\kappa}_s/\hat{\kappa}_f = 3.8$ (—). Note that only a part of the entire signal is plotted.

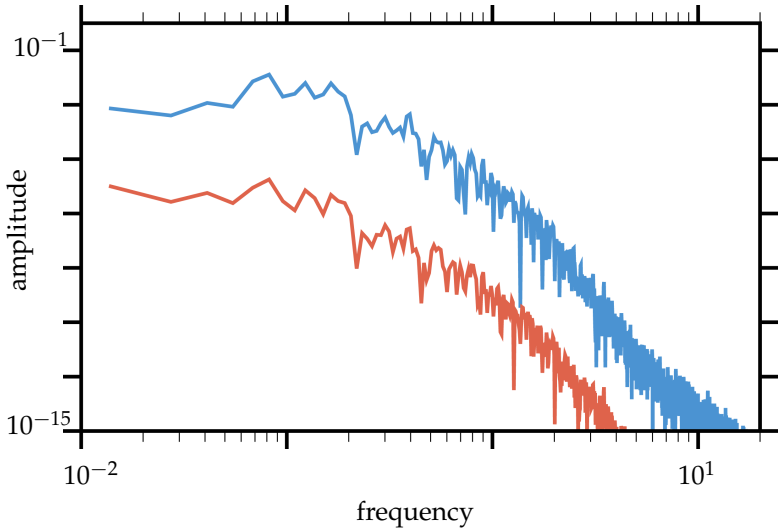

FIGURE 7.5: The power spectrum of the Nusselt number components in the presence of radiation at $z = 0$ for $Ra = 6.3 \times 10^7$ and $\hat{\kappa}_s/\hat{\kappa}_f = 0.003$; convective part $\langle Nu_c \rangle_{S_z}$ (—), radiative part $\langle Nu_r \rangle_{S_z}$ (—).

is $r = -0.79$ for $\hat{\kappa}_s/\hat{\kappa}_f = 0.003$ and $r = -0.77$ for $\hat{\kappa}_s/\hat{\kappa}_f = 3.8$, it is concluded that Nu_c and Nu_r are strongly anti-correlated in time, though the correlation is slightly stronger for $\hat{\kappa}_s/\hat{\kappa}_f = 0.003$. This is understandable because, as depicted in Figure 7.4, whenever the radiative heat flux increases, the convective one decreases. It can also be seen that this behaviour is more pronounced for

$\hat{\kappa}_s/\hat{\kappa}_f = 0.003$ than for $\hat{\kappa}_s/\hat{\kappa}_f = 3.8$. Furthermore, the time fluctuations of Nu_c and Nu_r are explained with the help of Figure 7.5, where the power spectrum of the area-averaged convective and radiative Nusselt numbers evaluated at the bottom interface for $\hat{\kappa}_s/\hat{\kappa}_f = 0.003$ are plotted. In the low frequency region, the peaks appear for the same frequency, which means that the cycle of the large-scale circulations has equal impact on the fluctuations of the convective and radiative Nusselt number. Thus, this pronounced anti-correlation reflects the fact that the considered processes take place on similar time scales.

Correlation in space.
In order to measure the correlation in space, the correlation coefficient r is calculated from the time-averaged distribution of the convective and radiative Nusselt number evaluated at both interfaces. The distributions for $\hat{\kappa}_s/\hat{\kappa}_f = 0.003$ are shown in Figures 7.3a–7.3d, and the corresponding correlation coefficients are $r = -0.65$ at $z = 0$ and $r = -0.80$ at $z = 1$. The fact that they are both negative shows that radiation and convection are anti-correlated in space at both interfaces. The reason is that the radiative heat flux is high if the convective one is low, and vice versa, which is especially visible in the centre of the bottom interface and close to the widthwise walls at the top interface.

Furthermore, the dependence of the correlation in space on the thermal diffusivity ratio is examined by calculating the correlation coefficient for $\hat{\kappa}_s/\hat{\kappa}_f = 3.8$ obtained from the distribution of Nu_c and Nu_r plotted in Figures 7.6a–7.6d. They are $r = 0.48$ at $z = 0$ and $r = -0.18$ at $z = 1$, showing that the correlation in space is a lot weaker for $\hat{\kappa}_s/\hat{\kappa}_f = 3.8$ than $\hat{\kappa}_s/\hat{\kappa}_f = 0.003$. This happens because the distribution of Nu_r changes considerably at both interfaces, from a non-elliptical one for $\hat{\kappa}_s/\hat{\kappa}_f = 0.003$ to an elliptical-like distribution for $\hat{\kappa}_s/\hat{\kappa}_f = 3.8$, while the distribution of Nu_c remains nearly unchanged. Finally, it is necessary to add that since the distribution of Nu_c strongly depends on the large-scale circulations, which do not considerably vary with $\hat{\kappa}_s/\hat{\kappa}_f$, the topology of Nu_c does not change much with $\hat{\kappa}_s/\hat{\kappa}_f$ either. On the contrary, since all the contributors to Nu_r depend on the temperature, which varies with $\hat{\kappa}_s/\hat{\kappa}_f$, the distribution of Nu_r also changes with $\hat{\kappa}_s/\hat{\kappa}_f$. This is discussed in detail in Section 7.3.

7.3 Mean emissive and irradiative heat transfer

In order to better understand the consequences of the radiation model used in this research, all the radiative heat flux contributors, i.e. the emissive and irradiative heat fluxes, are described, and their dependencies on the thermal diffusivity ratio and the Rayleigh number, will be discussed. Then the influence of the magnitude and non-homogeneity of the temperature distribution at the interface on the irradiation originating from the interface will be examined, and the interaction of the radiation with the ambient environment through the trans-

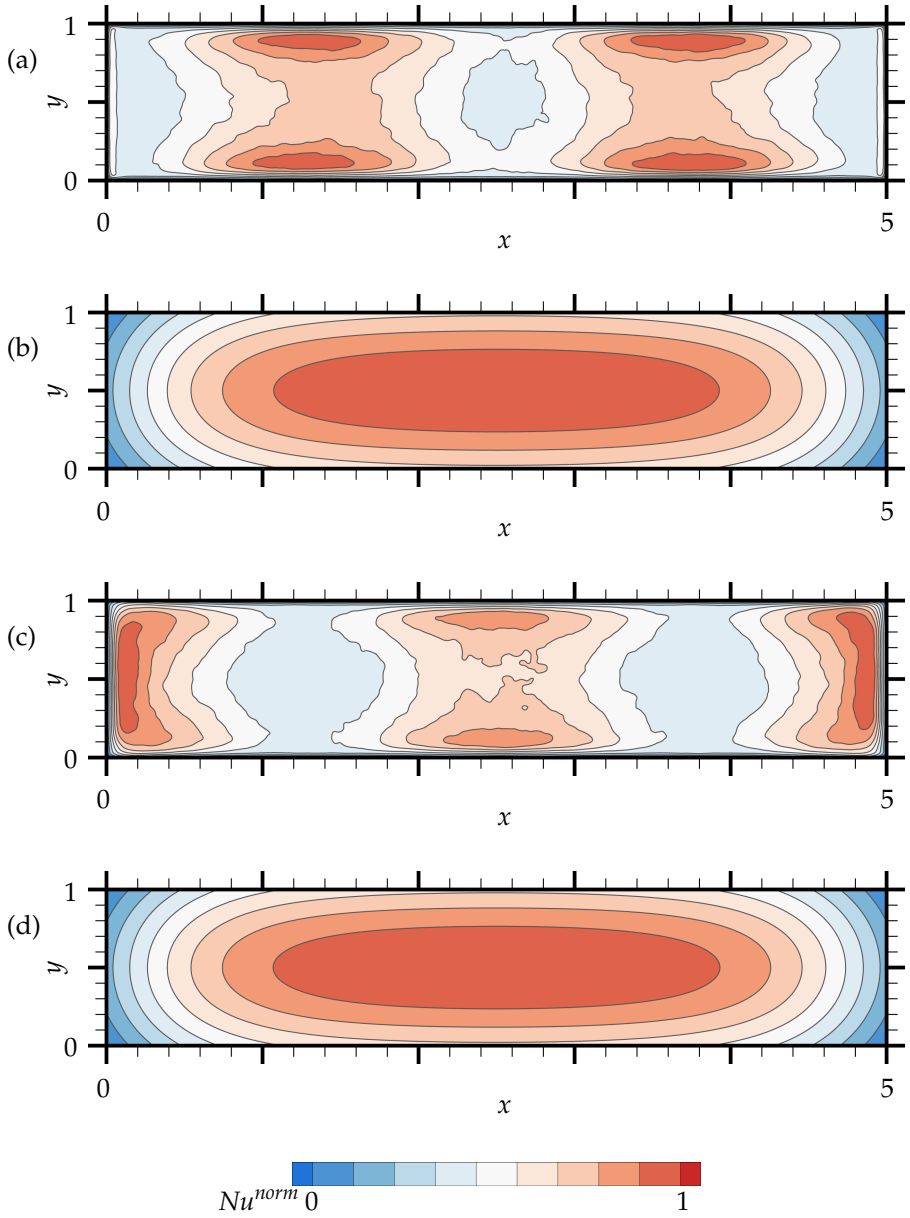

FIGURE 7.6: The distribution of the normalised time-averaged Nusselt number components in the presence of radiation for $Ra = 6.3 \times 10^7$ and $\hat{\kappa}_s/\hat{\kappa}_f = 3.8$ at $z = 0$ (a, b) and $z = 1$ (c, d). Nu_c^{norm} (a, c), Nu_r^{norm} (b, d). Normalisation obtained from $Nu_c^{min} = 6.36$, $Nu_c^{max} = 42.17$, $Nu_r^{min} = 44.71$, $Nu_r^{max} = 54.13$ at $z = 0$ and $Nu_c^{min} = 6.53$, $Nu_c^{max} = 43.59$, $Nu_r^{min} = 43.10$, $Nu_r^{max} = 53.03$ at $z = 1$.

parent side walls will also be addressed, as well as the different contributions to the irradiative Nusselt number Nu_{ir}. Finally, the dependence of the radiative heat flux on the thermal diffusivity ratio, which was left open in the previous section, will be analysed.

7.3.1 Mean emissive heat transfer

Considering the emissive heat flux Nu_e evaluated for $Ra = 6.3 \times 10^7$ and $\hat{\kappa}_s/\hat{\kappa}_f = 0.003$, the contours of the time-averaged distributions at the bottom and top interfaces resemble the isotherms presented in Figures 6.1b and 6.1d, respectively. The reason is that the emissive heat flux depends only on the temperature at the interface, since the control parameters for radiation are constant (see (7.4)). Considering that the temperatures at the interfaces (see Chapter 6) are affected by changes in the thermal diffusivity ratio and the Rayleigh number, it is to be expected that the distribution and the intensity of the emissive heat flux changes with $\hat{\kappa}_s/\hat{\kappa}_f$ and Ra.

Variations in the distribution of Nu_e are analysed in terms of its relative standard deviation, which is defined analogously to (6.1). When low conductivity plates are employed, i.e. $\hat{\kappa}_s/\hat{\kappa}_f = 0.003$, $\langle Nu_e \rangle_t$ varies in space by 0.2% for $Ra = 6.3 \times 10^7$. The fact that the corresponding relative spatial variations of the temperatures at the interfaces are $\langle \delta_{S_z} \rangle_t = 6\%$ (Chapter 6) shows that the former are significantly smaller. Something similar is true when high conductivity plates are employed: the marginal $\langle \delta_{S_z} \rangle_t$ leads to even smaller spatial variations of $\langle Nu_e \rangle_t$, i.e. 0.0006%.

Figure 7.7 presents the time- and area-averaged emissive Nusselt number $\langle Nu_e \rangle_{t,S_z}$ evaluated at both interfaces, for low and high thermal diffusivity ratios and various Ra. Their absolute values reflect the emission intensity. At the bottom interface, the emission intensity obtained for the higher thermal diffusivity ratio $\hat{\kappa}_s/\hat{\kappa}_f = 3.8$ is 3.9% larger for $Ra = 6.3 \times 10^7$ than for the lower thermal diffusivity ratio $\hat{\kappa}_s/\hat{\kappa}_f = 0.003$. Since a further increase in 0.002% is obtained by decreasing the Rayleigh number from $Ra = 6.3 \times 10^7$ to $Ra = 3.5 \times 10^5$, it is concluded that the variations of the emission intensity are more sensitive to the changes of $\hat{\kappa}_s/\hat{\kappa}_f$ than to Ra.

7.3.2 Mean irradiative heat transfer through the side walls

The time-averaged distributions of irradiation which originates from the ambient environment and reaches the bottom and top interfaces through the transparent side walls are plotted in Figures 7.8a and 7.9a, respectively, for $Ra = 6.3 \times 10^7$ and $\hat{\kappa}_s/\hat{\kappa}_f = 0.003$. They are the same at both interfaces and resemble an elliptical-like shape with a minimum in the centre and a maximum at the widthwise walls. The shape of these distributions follows that of the view

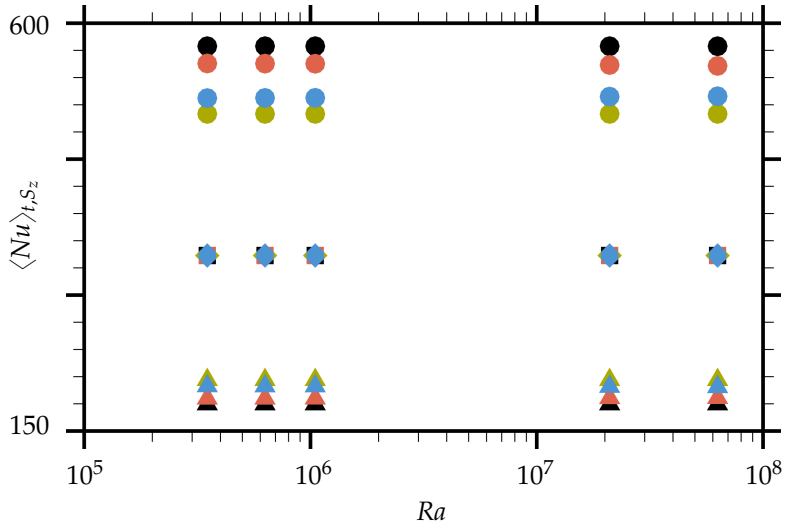

FIGURE 7.7: Absolute values of the time- and area-averaged Nusselt number components in the presence of radiation; $\langle Nu_e \rangle_{t,S_z}$ (circle symbols), Nu_{ir}^{sw} (square symbols), Nu_{ir}^{i} (delta symbols) evaluated at $z = 0$ for $\hat{\kappa}_s/\hat{\kappa}_f = 0.003$ (red symbols) and $\hat{\kappa}_s/\hat{\kappa}_f = 3.8$ (black symbols), and at $z = 1$ for $\hat{\kappa}_s/\hat{\kappa}_f = 0.003$ (blue symbols) and $\hat{\kappa}_s/\hat{\kappa}_f = 3.8$ (green symbols). Note that for all Rayleigh number the square symbols coincide.

factors. Thus, since the cuboidal domain is symmetrical, these distributions are the same at the top and bottom interfaces. Additionally, the magnitude of the maximum is determined by the ambient temperature and the control parameters for radiation.

In order to study the dependence of the irradiation through the side walls on the Rayleigh number and the thermal diffusivity ratio, the time- and area-averaged $Nu_{sw\to b}$ and $Nu_{sw\to t}$ are plotted in Figure 7.7 (square symbols) versus Ra for low and high $\hat{\kappa}_s/\hat{\kappa}_f$. The fact that the values remain constant reflects the fact that the strength of the irradiation is independent of the Rayleigh number and the thermal diffusivity ratio. The reason is that the control parameters for radiation and the ambient temperature do not vary with Ra or $\hat{\kappa}_s/\hat{\kappa}_f$.

7.3.3 Mean irradiative heat transfer from the interface

The mean intensities of $Nu_{t\to b}$ and $Nu_{b\to t}$ are determined analogously to those for $Nu_{sw\to b}$. They are plotted in Figure 7.7 for various Ra and $\hat{\kappa}_s/\hat{\kappa}_f$. Since they vary less than 0.5% for $\hat{\kappa}_s/\hat{\kappa}_f = 0.003$ and even two orders of magnitude less for $\hat{\kappa}_s/\hat{\kappa}_f = 3.8$, they are nearly independent of the Rayleigh number. Thus, the irradiation originating from the interface is nearly independent of the turbulent flow for any conductivity of the plates.

The time-averaged distribution of the irradiation which originates from the interface and is absorbed by the opposite plate is plotted in Figures 7.8b and 7.9b

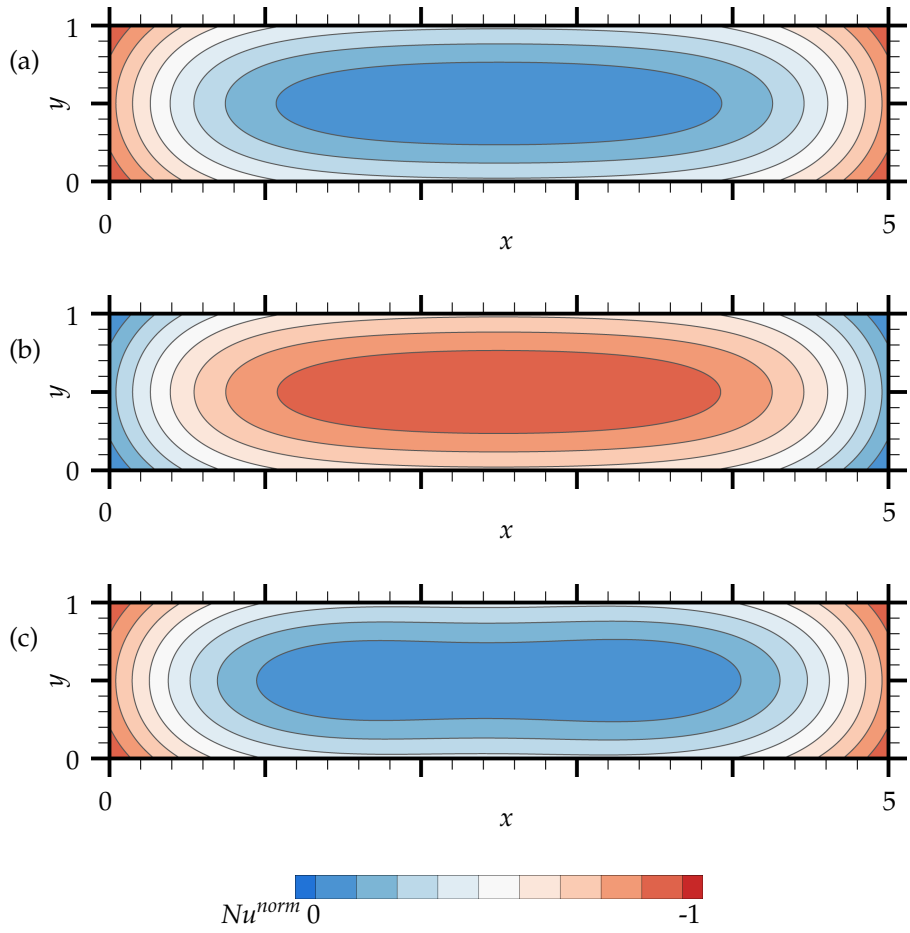

FIGURE 7.8: The distribution of the Nusselt number components for $Ra = 6.3 \times 10^7$ and $\hat{\kappa}_s/\hat{\kappa}_f = 0.003$ at $z = 0$ in the presence of radiation. $Nu^{norm}_{sw\to b}$ (a), $Nu^{norm}_{t\to b}$ (b), $Nu^{norm}_{ir,z=0}$ (c). Normalisation obtained from $Nu^{min}_{sw\to b} = -302.45$, $Nu^{max}_{sw\to b} = -441.67$, $Nu^{min}_{t\to b} = -91.62$, $Nu^{max}_{t\to b} = -226.60$, $Nu^{min}_{ir} = 528.97$, $Nu^{max}_{ir} = 533.31$. Note that the negative sign of Nu^{norm} represents the normal vector, which points against the z-direction.

for $Ra = 6.3 \times 10^7$ and $\hat{\kappa}_s/\hat{\kappa}_f = 0.003$, which shows that irradiation leads to an elliptical-like distribution of $Nu_{t\to b}$ and $Nu_{b\to t}$ with a maximum in the centre of the interface. It is important to note that this shape is obtained from the non-homogeneous temperature distribution at the interface of the opposite plate (see Figure 6.1). Moreover, as discussed above, a similar shape of the distributions of $Nu_{sw\to b}$ and $Nu_{sw\to t}$ is obtained due to irradiation through the side walls even though the ambient temperature T_{out} is constant. Thus, it is to be expected that the spatial temperature variations at the interfaces do not considerably affect the irradiative Nusselt numbers evaluated at the interface of the opposite plate, i.e. $Nu_{t\to b}$ and $Nu_{b\to t}$. The latter is verified and discussed in Section 9.2 of Chapter 9.

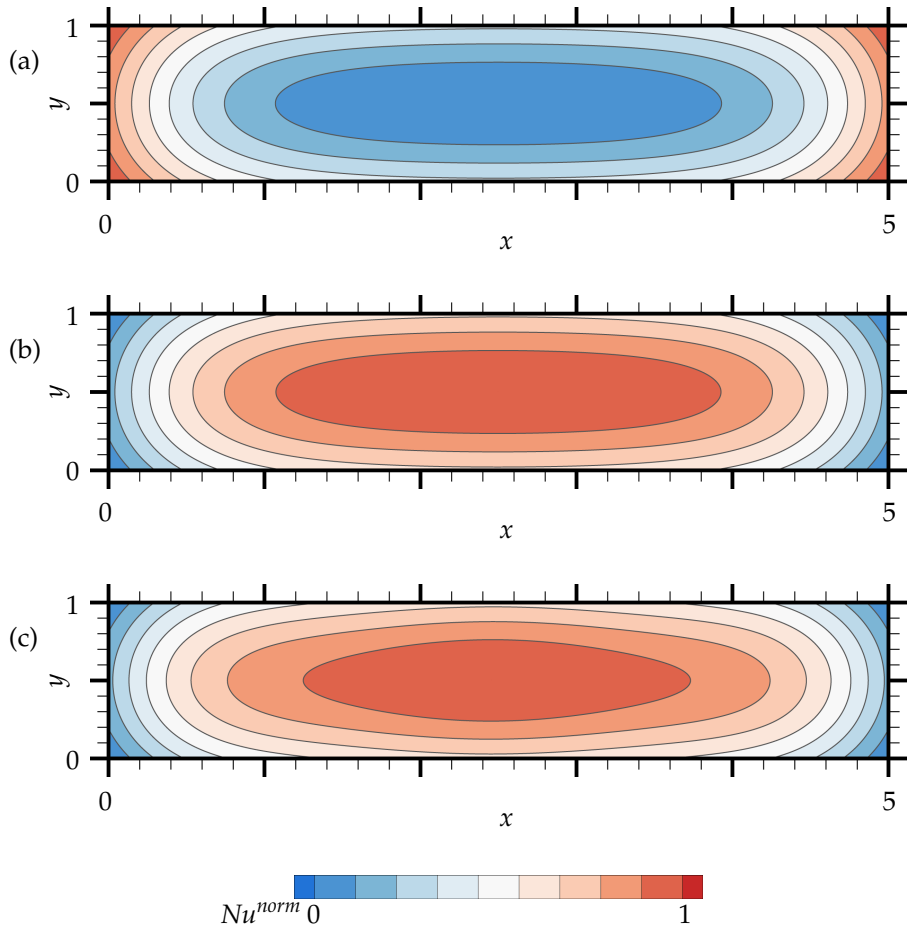

FIGURE 7.9: The distribution of the Nusselt number components for $Ra = 6.3 \times 10^7$ and $\hat{\kappa}_s/\hat{\kappa}_f = 0.003$ at $z = 1$ in the presence of radiation. $Nu^{norm}_{sw\to t}$ (a), $Nu^{norm}_{b\to t}$ (b), $Nu^{norm}_{ir,z=1}$ (c). Normalisation obtained from $Nu^{min}_{sw\to t} = 302.45$, $Nu^{max}_{sw\to t} = 441.67$, $Nu^{min}_{b\to t} = 97.62$, $Nu^{max}_{b\to t} = 241.04$, $Nu^{min}_{ir} = 539.30$, $Nu^{max}_{ir} = 543.49$.

Furthermore, in order to describe how the irradiation originating from the interface changes with the magnitude of the mean interface temperature $\langle T\rangle_{S_z}$, the widthwise-averaged profiles of $Nu_{b\to t}$ obtained from low and high temperature at the interface are plotted in Figure 7.10. These profiles are obtained from the instantaneous temperature fields for $Ra = 6.3 \times 10^7$, $\hat{\kappa}_s/\hat{\kappa}_f = 0.003$ and $\hat{\kappa}_s/\hat{\kappa}_f = 3.8$, for which $\langle T\rangle_{S_{z=0}} = 0.220$ and $\langle T\rangle_{S_{z=0}} = 0.499$, respectively. They nearly collapse in the regions close to the widthwise walls, yet they definitely do not in the centre of the top interface. There, $\langle Nu_{b\to t}\rangle_y$ increases by a factor of 1.04. Thus, the dependence of the irradiation originating from the bottom interface on the magnitude of $\langle T\rangle_{S_{z=0}}$ varies in space with the maximal difference in the centre of the top interface and the minimal one close to the widthwise walls. The difference

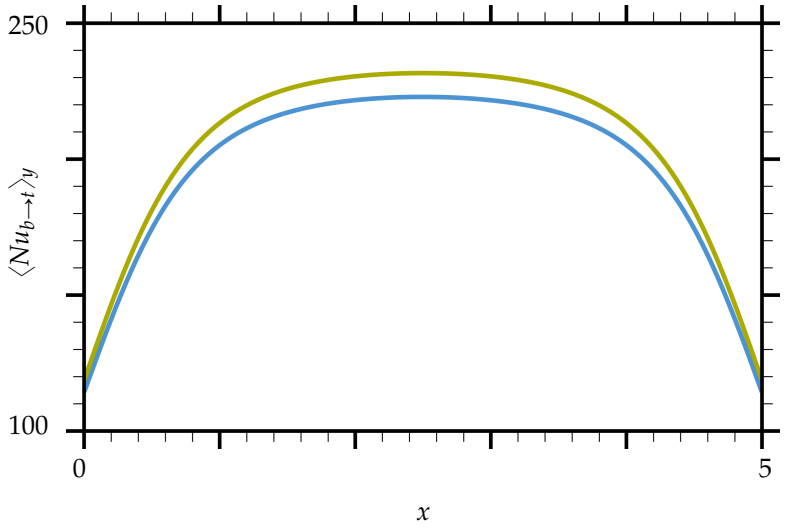

FIGURE 7.10: Profiles of line-averaged $Nu_{b\to t}$ in the presence of radiation for $Ra = 6.3 \times 10^7$, $\hat{\kappa}_s/\hat{\kappa}_f = 0.003$ (—) and $\hat{\kappa}_s/\hat{\kappa}_f = 3.8$ (—).

in $\langle Nu_{b\to t}\rangle_y$ observed in the centre comes from the fact that $\langle T\rangle_{S_z} + \Theta$ is two orders of magnitude bigger than the difference between the interface temperatures, which finally is big enough to cause a visible increase in $\langle Nu_{b\to t}\rangle_y$. On the other hand, the neglectable difference in $\langle Nu_{b\to t}\rangle_y$ observed close to the widthwise walls is due to the small values of the view factors in this region. Hence, even the major effect caused by different interface temperatures diminishes close to the widthwise walls.

7.3.4 Radiative interaction with the ambient environment

Since the transparent side walls allow heat to enter and leave the cell, it is of interest to analyse how the radiation through the side walls affects the heat balance in the convection cell considered. The total heat flux entering the RB cell through the transparent side walls, i.e. $\langle Nu_{sw\to b}\rangle_{t,S_{z=0}} + \langle Nu_{sw\to t}\rangle_{t,S_{z=1}}$ plotted in Figure 7.7, contributes 64% to the total heat flux emitted by both interfaces, i.e. $\langle Nu_e\rangle_{t,S_{z=0}} + \langle Nu_e\rangle_{t,S_{z=1}}$. On the other hand, evaluating the heat transmitted from the inside of the cell to the ambient environment from

$$\langle Nu_{b\to sw}\rangle_{t,S_{z=0}} = \langle Nu_e\rangle_{t,S_{z=0}} - \langle Nu_{b\to t}\rangle_{t,S_{z=0}}, \tag{7.8}$$

$$\langle Nu_{t\to sw}\rangle_{t,S_{z=1}} = \langle Nu_e\rangle_{t,S_{z=1}} - \langle Nu_{t\to b}\rangle_{t,S_{z=1}} \tag{7.9}$$

reveals that 64% of the total emissive energy leaves the cell through the transparent side walls. Thus, the heat radiation through the transparent side walls does not affect the energy balance. This is true as long as the constant ambient temperature equals the mean cell temperature T_0.

However, since $\langle Nu_{b\to sw}\rangle_{t,S_{z=0}} > \langle Nu_{sw\to b}\rangle_{t,S_{z=0}}$, more heat is transferred from the bottom interface through the side walls than the same way back. Additionally, since $\langle Nu_{t\to sw}\rangle_{t,S_{z=0}} < \langle Nu_{sw\to t}\rangle_{t,S_{z=0}}$, more heat is transferred from the ambient environment to the top interface than in the other direction. Thus, the transparent side walls enhance the radiative heat transfer from the hot to the cold interface since the ambient temperature is lower than the temperature at the bottom interface and higher than the temperature at the top interface.

7.3.5 Mean total irradiative heat transfer

Figures 7.8c and 7.9c show the distributions of the irradiative Nusselt number at the bottom and top interface, respectively, obtained for $Ra = 6.3 \times 10^7$ and $\hat{\kappa}_s/\hat{\kappa}_f = 0.003$. It can be seen that at $z = 0$ (the bottom interface), the total irradiative Nusselt number is minimal in the centre of the interface and maximal close to the lateral widthwise walls. The opposite is true at the top interface, where the total Nu_{ir} is maximal in the centre and minimal close to the lateral widthwise walls. The reason for this is related to the different contributions of the Nu_{ir} contributors to the total irradiation. At $z = 0$, the main source is the irradiation originating from the ambient environment (Figure 7.8a) with a smaller contribution of the irradiation from the top interface (Figure 7.8b) since the temperature T_{out} is higher than the temperatures at the top interface. On the other hand, at $z = 1$ (top interface), the irradiation originating from the bottom interface (Figure 7.9b) dominates the irradiation from the ambient environment (Figure 7.9a) since the temperature at the bottom interface is always higher than T_{out}. The same holds true for highly conductive solid plates.

7.3.6 Influence of the plate's thermal diffusivity on the radiative heat transfer

The dependence of the radiative heat flux on the thermal diffusivity ratio is discussed below. As shown in Section 7.2 and in Figures 7.3b, 7.3d and 7.6b, 7.6d, the distribution of the radiative heat flux is non-elliptical for $\hat{\kappa}_s/\hat{\kappa}_f = 0.003$ and elliptical-like for $\hat{\kappa}_s/\hat{\kappa}_f = 3.8$. In order to understand which of the Nu_r contributions is responsible for this change of shape, their influences are analysed individually below.

Since the irradiation through the side walls is independent of the thermal diffusivity ratio, this part of the radiative heat flux is not responsible for this difference in shapes.

There are two potential reasons why the irradiation from the opposite interface might be responsible for these differences. The first arises from the fact that the temperature distributions at the interfaces are less homogeneous for $\hat{\kappa}_s/\hat{\kappa}_f = 0.003$ than for $\hat{\kappa}_s/\hat{\kappa}_f = 3.8$. However, as mentioned and is to be proved

in Section 9.2 of Chapter 9, the non-homogeneity of the temperature distribution does not affect the distributions of $Nu_{b\to t}$ and $Nu_{t\to b}$, and hence neither that of Nu_r.

The second reason is the magnitude of the absolute temperature at the interfaces, which is smaller for $\hat{\kappa}_s/\hat{\kappa}_f = 0.003$ than for $\hat{\kappa}_s/\hat{\kappa}_f = 3.8$. Nevertheless, as discussed in this section, the mean temperature determines only the maximum and the gradation of the elliptical-like distribution of $Nu_{b\to t}$ and $Nu_{t\to b}$. Thus, the magnitude of $\langle T \rangle_{S_{z=0}}$ is responsible only for the strength of Nu_r and not for the shape of its distribution.

The remaining radiative heat flux contributor is the emissive heat flux. Considering $\hat{\kappa}_s/\hat{\kappa}_f = 3.8$ and $Ra = 6.3 \times 10^7$, the spatial standard deviation of Nu_e is approximately 0.003 at both interfaces, while that of Nu_{ir} is 2.2. Thus, since the variations of Nu_e are much smaller than those of Nu_{ir}, emission barely affects the shape of Nu_r and hence the latter follows the elliptical-like distribution of Nu_{ir}. On the other hand, for $\hat{\kappa}_s/\hat{\kappa}_f = 0.003$ and $Ra = 6.3 \times 10^7$, the spatial standard deviations of Nu_e and Nu_{ir} are approximately 1.0 at both interfaces. Thus, since the variations of Nu_e and Nu_{ir} are of the same order, the non-elliptical distribution of Nu_e alters the elliptical-like distribution of Nu_{ir} and finally the distribution of Nu_r is non-elliptical. It can be concluded that the non-homogeneity of the distribution of Nu_e, which depends on the thermal diffusivity ratio, has a very strong impact on the shape of the Nu_r distribution.

8

INFLUENCE OF RADIATION PARAMETERS

In the following, the control parameters for radiation, i.e. Nr and Θ, and for convection, i.e. Ra, are varied to study their influence on the radiative and convective heat transfer as well as on the effective Rayleigh number. The analysis is limited to the low conductivity plates, i.e. $\hat{\kappa}_s/\hat{\kappa}_f = 0.003$, since for the high conductivity plates, the radiation only marginally changes Nu_c and Ra_{eff}. The control parameters realised in the simulations considered here are summarised in Table A2.

In order to estimate these dependencies, the scaling relations will be analysed based on the time- and volume-averaged Nusselt number contributions and the time- and area-averaged ΔT_{eff} by employing the following approach. For a fixed Rayleigh number, the least squares fit to the data points is found at first for the same Θ and afterwards for the same Nr. The resulting scaling relations of the radiative and convective Nusselt numbers as well as the effective temperature difference are represented by the fitting function

$$\psi\big(Ra, \Theta, Nr\big) = \mathscr{A}\big(Ra\big) \cdot \exp\big(\mathscr{B}\,(Ra) \cdot \Theta\big) \cdot \ln\big(\mathscr{C}\,(Ra) \cdot Nr\big), \tag{8.1}$$

where $\mathscr{A}$, $\mathscr{B}$ and $\mathscr{C}$ are terms which depend on the Rayleigh number. They are

	a			b		
	Nu_r	Nu_c	ΔT_{eff}	Nu_r	Nu_c	ΔT_{eff}
$\mathscr{A}$	-0.14	-2.95	0.0578	7.38	29.08	-1.69
$\mathscr{B}$	0.0011	0.0017	0.0011	0.018	-0.088	-0.065
$\mathscr{C}$	-471.10	-4.58	-3.90	14785.48	240.06	173.70

TABLE 8.1: The least squares fitting parameters for Nu_r, Nu_c and ΔT_{eff}.

given by the second fitting function, $\zeta(Ra) = a\ln(Ra) + b$. The corresponding constants a and b are listed in Table 8.1.

Prior to the analysis of these scaling relations, it is necessary to understand how the dimensionless and dimensional quantities are related. While the strength of the convection is determined by the Rayleigh number Ra and the Prandtl number Pr, the strength of the radiation is represented by the radiation number Nr and the temperature ratio Θ. The thermal diffusivity ratio $\hat{\kappa}_s/\hat{\kappa}_f$ controls the conduction process in the solid plates. Since in the presence of radiation many mutually dependent dimensionless parameters are fixed, one set of these dimensionless control parameters determines one and only one set of the dimensional quantities. Thus, an increase in any of the control parameters for radiation, while keeping the others constant, leads to a strong increase in the mean temperature $\hat{T}_0$ as well as to a moderate increase in the height of the cell $\hat{H}$ and of all the fluid properties except the thermal expansion coefficient $\hat{\alpha}_p$, which drops due to a growth of $\hat{T}_0$. Besides the fact that the magnitude of the dimensional quantities scales differently with a change of the dimensionless control parameters for radiation, there is one principal difference, which arises from varying Θ or Nr. As Nr increases, the temperature difference $\hat{\Delta T}$ increases as well. However, if Θ increases, $\hat{\Delta T}$ decreases. Therefore, a change in the control parameters for radiation influences the ratios between the dimensional quantities. This leads to different radiative and convective contributions to the total heat transfer, which is important to remember for the upcoming interpretation.

8.1 Radiative Nusselt number

The time- and volume-averaged radiative Nusselt number versus Θ and Nr are presented in Figures 8.1a and 8.1b, respectively, and show that the radiative Nusselt number increases with increasing the control parameters for radiation. A similar observation was reported by Lan et al. (2003), although they considered a radiatively non-participating fluid, isothermal horizontal BCs, and adiabatic vertical BCs. The slope of the fitting function ψ, which is presented in Figure 8.1, is derived from (8.1) and Table 8.1 for Nu_r. It is 0.04 for $Ra = 6.3 \times 10^7$ and $Nr = 0.0008$ and 14.10 for the same Ra and $\Theta = 29$. This quantitatively illustrates that the radiative heat flux is more sensitive to a change in the radiation number than to a change in the temperature ratio. The same holds true for any other Rayleigh number, since, e.g. the slope for $Ra = 3.5 \times 10^5$ and $Nr = 0.0008$ equals 0.03, and the corresponding one for $\Theta = 29$ equals 13.81.

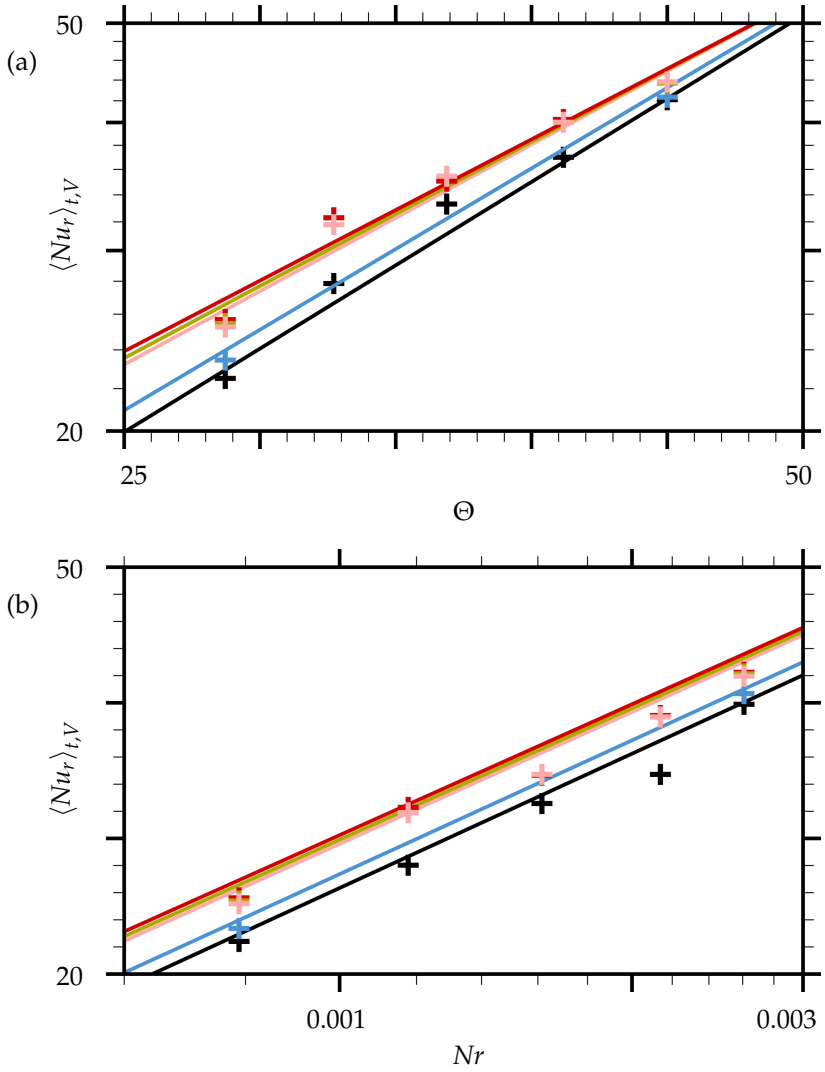

FIGURE 8.1: The time- and volume-averaged Nu_r versus Θ (a) and Nr (b) illustrated by a log-lin (a) and lin-log plot (b) for $Nr = 0.0008$ (a), $\Theta = 29$ (b) and $\hat{\kappa}_s/\hat{\kappa}_f = 0.003$. The solid lines represent the fitting function according to (8.1) for which the fitting error is 2.6%, and the symbols indicate the corresponding data for $Ra = 3.5 \times 10^5$, $Ra = 6.3 \times 10^5$, $Ra = 1.05 \times 10^6$, $Ra = 2.1 \times 10^7$ and $Ra = 6.3 \times 10^7$. Note that the uncertainty in the data due to statistical averaging is below 0.1, and hence the resulting error bars lie within the data points.

8.2 Convective Nusselt number

The time- and volume-averaged convective Nusselt numbers versus Θ and Nr are plotted in Figures 8.2a and 8.2b. The comparison of the relations obtained with the corresponding ones from Figure 8.1 for Nu_r reveals that whenever the convective Nusselt number drops due to an increase in the control parameters

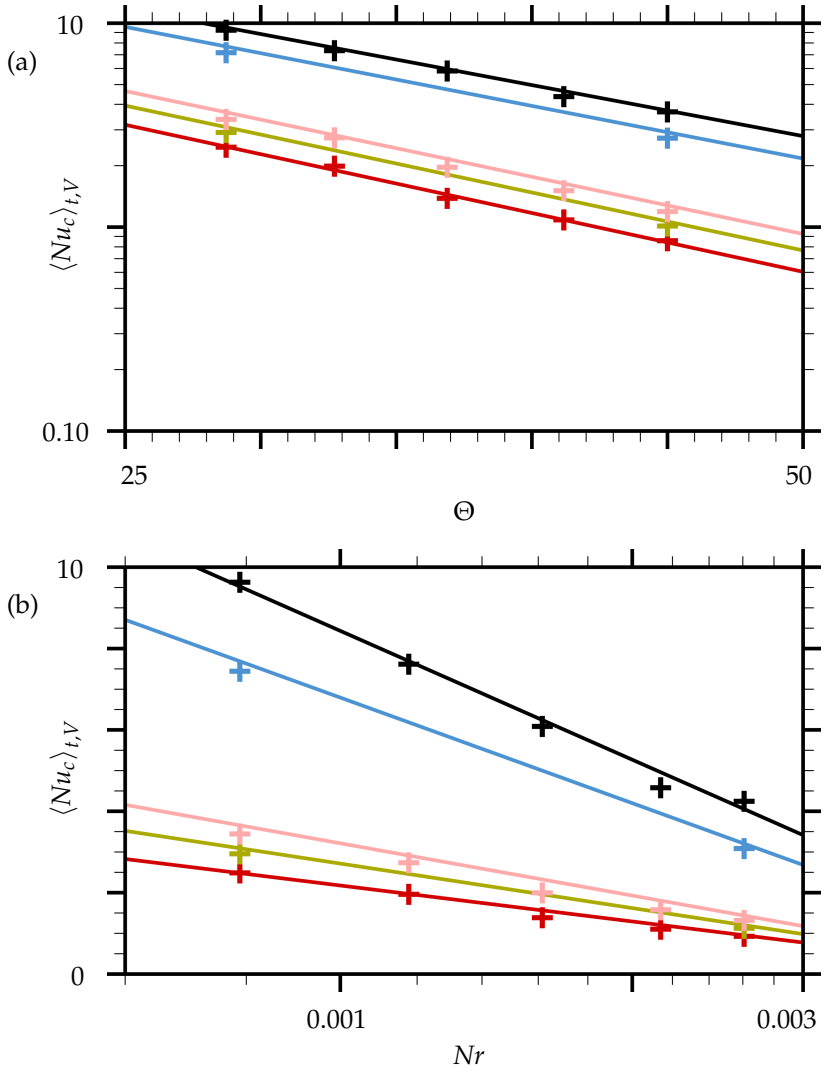

FIGURE 8.2: The time- and volume-averaged Nu_c versus Θ (a) and Nr (b) illustrated by a log-lin (a) and lin-log plot (b) for $Nr = 0.0008$ (a), $\Theta = 29$ (b) and $\hat{\kappa}_s/\hat{\kappa}_f = 0.003$. The solid lines represent the fitting function according to (8.1) for which the fitting error is 3.4%, and the symbols indicate the corresponding data for $Ra = 3.5 \times 10^5$, $Ra = 6.3 \times 10^5$, $Ra = 1.05 \times 10^6$, $Ra = 2.1 \times 10^7$ and $Ra = 6.3 \times 10^7$. Note that the uncertainty in the data due to statistical averaging is below 0.01, and hence the resulting error bars lie within the data points.

for radiation, the radiative Nusselt number increases. Moreover, the same relation between Nu_c and Nu_r is obtained if the Rayleigh number decreases. This extends the findings from Section 7.2 of Chapter 7 which stand for $\Theta = 29$, $Nr = 0.0008$ and $Ra = 6.3 \times 10^7$, clearly illustrating that both Nusselt number contributions are correlated also for higher values of the control parameters for radiation and lower Rayleigh numbers. Figure 8.2 further reveals that an in-

crease in at least one of the control parameters for radiation leads to a decrease in Nu_c. Additionally, the slope of the fitting curve derived from (8.1) and Table 8.1 for Nu_c is -0.058 for $Ra = 6.3 \times 10^7$ and $Nr = 0.0008$, and -4.60 for the same Ra and $\Theta = 29$. Thus, an increase in Nr or Θ stabilises the convective flow, although this process is more sensitive to an increase in Nr than to one in Θ.

8.3 Effective temperature difference between the interfaces

Figures 8.3a and 8.3b illustrate the dependence of the temperature difference between the interfaces, i.e. ΔT_{eff}, on Θ and Nr, respectively. It is clearly visible that ΔT_{eff} decreases if any of the control parameters for radiation increase. Moreover, it decreases even further with increasing Rayleigh number in order to satisfy the higher demand for the convective heat flux. However, the slope of the fitting function ψ for ΔT_{eff} is smaller than the one for Nu_c. As an example, for $Ra = 6.3 \times 10^7$ and $Nr = 0.0008$, it is -0.051, and for the same Ra and $\Theta = 29$ it is -0.221. The reason is that the thermal diffusivity of the fluid increases if any control parameter for radiation increases. Thus, thanks to the constant thermal diffusivity ratio $\hat{\kappa}_s/\hat{\kappa}_f$, the heat transfer through the solid plates can be sufficiently increased by a moderate drop in the temperature difference between the interfaces.

In future simulations, the obtained scaling relations for Nu_r, Nu_c and ΔT_{eff} can be used to estimate improved initial conditions. This will allow further reducing the CPU time requirements for the DNS presented here. Furthermore, when $Ra = 6.3 \times 10^7$, $\Theta = 45$ and $Nr = 0.0008$, the effective temperature difference, and consequently the effective Rayleigh number, is 69% smaller in the presence of radiation than in its absence. Thus, if this had been known *a priori*, then, according to the estimates by Shishkina et al. (2010), this simulation could have been performed on a coarser grid, with 750, 150 and 150 points in the x, y and z-directions, respectively. This could have reduced the total number of grid cells by almost a factor of 4, and hence sped up the whole simulation and especially the irradiation computations.

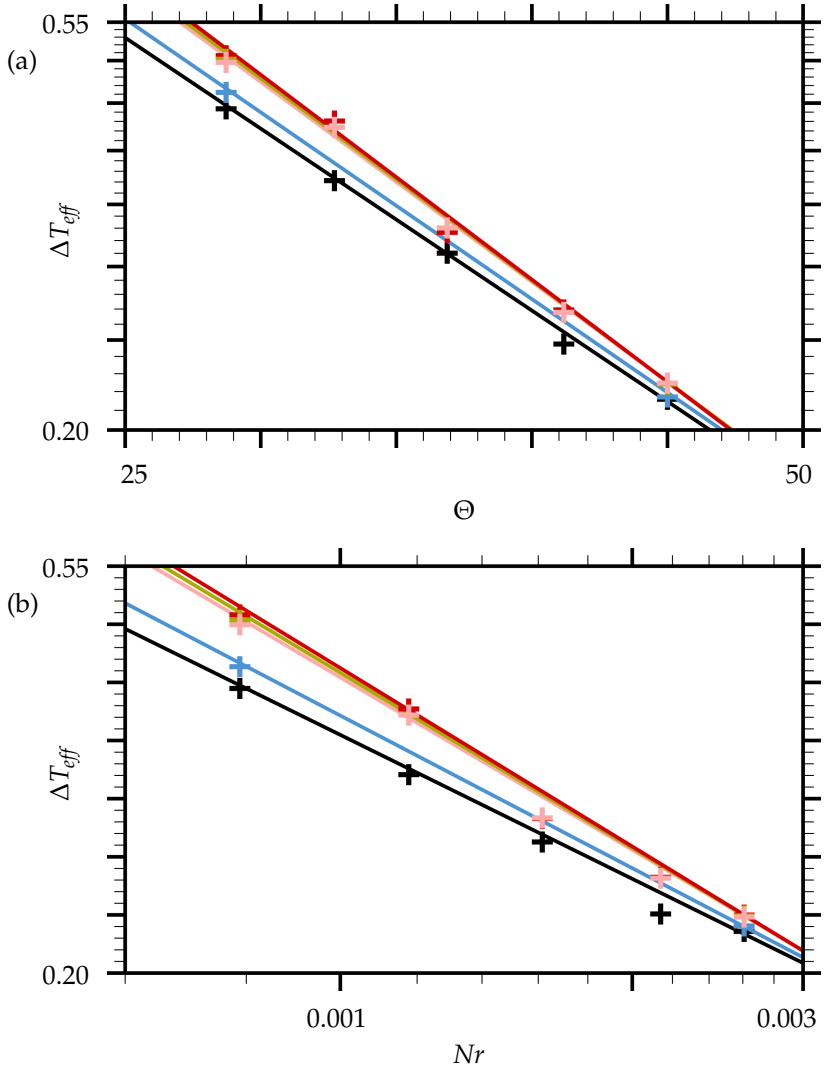

FIGURE 8.3: The time-averaged ΔT_{eff} versus Θ (a) and Nr (b) illustrated by a log-lin (a) and lin-log plot (b) for $Nr = 0.0008$ (a), $\Theta = 29$ (b) and $\hat{\kappa}_s/\hat{\kappa}_f = 0.003$. The solid lines represent the fitting function according to (8.1) for which the fitting error is 3.4%, and the symbols indicate the corresponding data for $Ra = 3.5 \times 10^5$, $Ra = 6.3 \times 10^5$, $Ra = 1.05 \times 10^6$, $Ra = 2.1 \times 10^7$ and $Ra = 6.3 \times 10^7$. Note that the uncertainty of the data due to statistical averaging is below 0.01, and hence the resulting error bars lie within the data points.

9

INFLUENCE OF THE BOUNDARY CONDITIONS AT THE ACTIVE PLATES

Since the temperatures which are developed at the solid–fluid interfaces of the low conductivity walls vary in time and space and are further modified by surface-to-surface radiation, the BCs considerably differ from the isothermal ones. However, the modelling of heat conduction through the plates as well as thermal radiation through the RB cell are computationally expensive (see Section 4.9 of Chapter 4), especially when engineering problems are of interest. Thus, it is desired by engineers to apply such simplified boundary conditions, which decrease the computational cost and implementation complexity but keep high accuracy of predictions. Due to the above, and taking into account that in thermal convection the proper predictions of the coherent structures are of interest, Section 9.1 focuses on answering the question how the coherent structures change with reducing the complexity level of the thermal boundary conditions.

Although, in thermal convection there exist two coherent structures which interact with each other, namely the large-scale circulation and the thermal plumes (Daya and Ecke 2001; Qiu and Tong 2001b), the analysis is limited to the thermal plumes. The reason for the latter is that only they stay in direct contact with the boundaries, and hence if the coherent structures are altered due to a change of BCs, the effect must be more pronounced for thermal plumes than large-scale flow structures. For the sake of simplicity, the analysis is limited to the hot plumes and the corresponding BCs at the bottom interface. Furthermore, since it is well known that plumes are fully developed at the border between the thermal boundary layer and the bulk, i.e. at $z{=}0.5H/Nu_{c,\mathit{eff}}$, that location is chosen for the investigation.

Furthermore, since the results presented in Section 7.3.3 of Chapter 7 indicates the potential for simplification of the irradiation calculations, it is to be verified in Section 9.2 whether the irradiation calculations based on the area-averaged temperature instead of the local ones give the accurate predictions.

Finally, Section 9.3 covers the discussion how the reduction of the complexity level of the thermal BCs affects the scaling of the global heat transfer.

9.1 Alteration of the coherent structures

Here, the boundary conditions used in this section are presented and the differences between them are described. The considered thermal boundary conditions are modelled by:

- solid horizontal plates of a finite thickness and $\hat{\kappa}_s/\hat{\kappa}_f = 0.003$, which account for the exchange of thermal radiation (abbreviated as LCP-rad)
- solid horizontal plates of a finite thickness and $\hat{\kappa}_s/\hat{\kappa}_f = 0.003$, which do not account for the exchange of thermal radiation (abbreviated as LCP)
- infinitely thin horizontal plates, which do not allow any temperature variations in time but the spatial temperature distribution follows the one of the time-averaged temperature distribution obtained from LCP (abbreviated as ITP-nh)
- infinitely thin horizontal plates, which do not allow any temperature variations in time nor in space (abbreviated as ITP).

From the above, the non-isothermal BCs are LCP-rad, LCP and ITP-nh. On the other hand, the isothermal BCs are only ITP. Moreover, since the BCs which account for radiative heat transfer are the most complex and the most realistic, the results obtained for LCP-rad are considered as the reference solution. On the other hand, the isothermal BCs (ITP) are considered as the most simplified BCs.

The above set of BCs is analysed for low, medium and high turbulence, which are obtained by setting different Rayleigh number for each type of the boundary condition. The control parameters for each configuration are listed in Table 9.1. Nevertheless, the simulations performed for each turbulence reflect the same effective Rayleigh number. Because of the latter, all the quantities analysed in this chapter are normalised with respect to Ra_{eff} as described in Section 2.3 of Chapter 2).

To have a clear picture of the considered boundary conditions, the temperature distributions evaluated at the bottom interfaces are plotted in Figure 9.1.

Since the topographies of the temperature distribution are similar for all considered Ra_{eff}, only one example set of the temperature distributions is shown there, which is obtained for $Ra_{eff} = 1.59 \times 10^7$.

When the solid plates are employed, the hot temperatures at the interfaces clearly mark the regions where the fluid rises the most frequently. Analogically, the cold temperatures indicate the regions where the fluid descends the most frequently. Thus, the interface conditions adapt to the flow and reflect large-scale circulations. On the other hand, when isothermal plates are employed, the local temperatures at the interfaces are the same as the time- and area-averaged one. In such a case, the interface conditions cannot adapt to the flow. By contrast, such simplification may affect thermal plumes' development, which is examined in the following sections.

Although the time- and area-averaged temperature at the interfaces $\langle T_{eff} \rangle_{t,S_z}$ is independent of the simplifications of the BCs and equals 0.5 and -0.5 at the bottom and top interface, respectively, the differences in the temperature distributions must be statistically described. This is done by calculating the spatial fluctuation of the temperature distribution, i.e.

$$\langle T_{eff,\delta_{S_z}} \rangle_t = \langle \sqrt{\langle (T_{eff} - \langle T_{eff} \rangle_{S_z})^2 \rangle_{S_z}} \rangle_t, \tag{9.1}$$

	Ra	Ra_{eff}	Nr	Θ	$\langle T_{eff,\delta_{S_z}} \rangle_t$	$\langle T_{eff,rms} \rangle_{S_z}$
LCP-rad	6.30×10^5	3.17×10^5	0.0008	29	0.0197	0.0015
LCP	3.50×10^5		–	–	0.0197	0.0015
ITP-nh	3.17×10^5		–	–	0.0197	0.0
ITP	3.17×10^5		–	–	0.0	0.0
LCP-rad	1.84×10^6	0.92×10^6	0.0008	29	0.0217	0.0016
LCP	1.05×10^6		–	–	0.0232	0.0020
ITP-nh	0.92×10^6		–	–	0.0232	0.0
ITP	0.92×10^6		–	–	0.0	0.0
LCP-rad	6.30×10^7	1.59×10^7	0.0026	29	0.0252	0.0016
LCP	2.10×10^7		–	–	0.0308	0.0020
ITP-nh	1.59×10^7		–	–	0.0308	0.0
ITP	1.59×10^7		–	–	0.0	0.0

TABLE 9.1: Details of the thermal boundary conditions at $z = 0$.

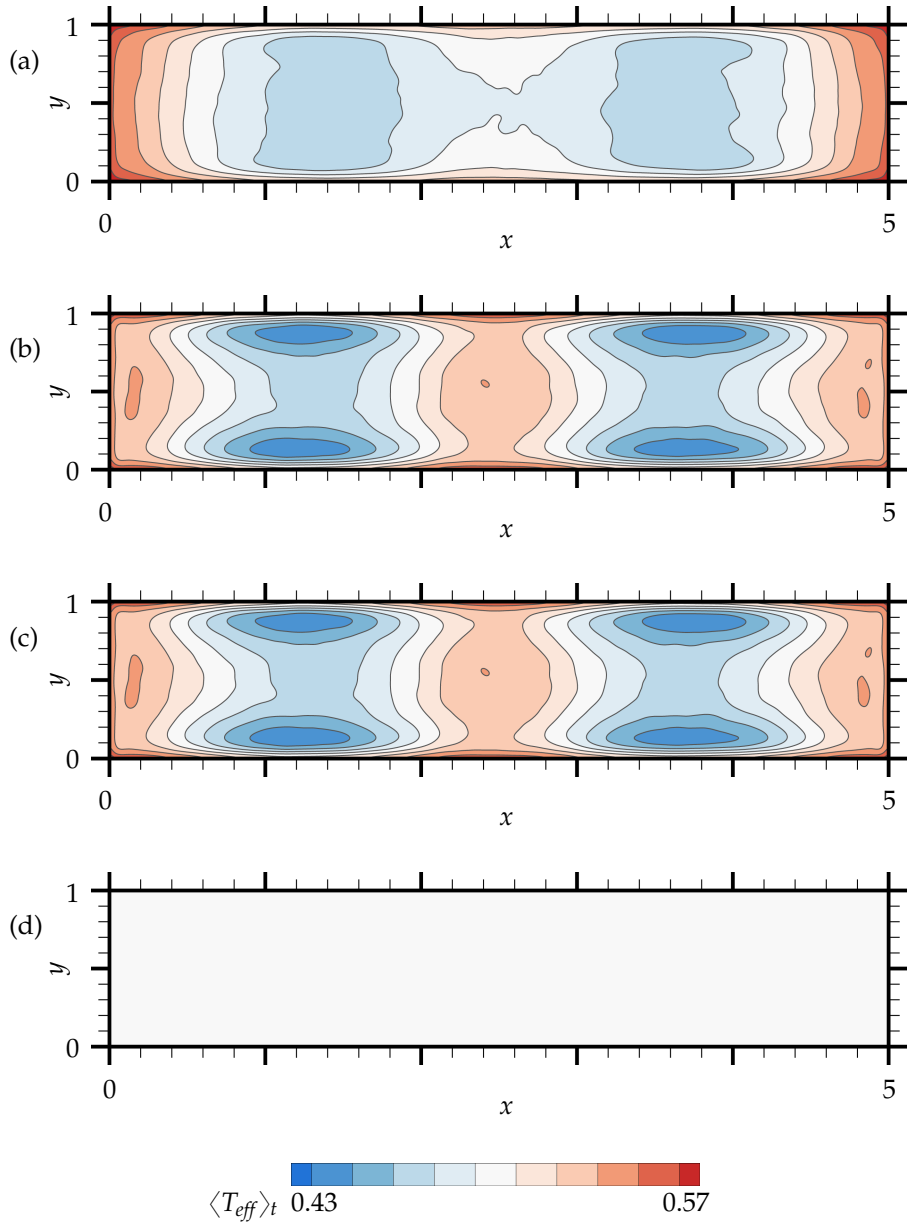

FIGURE 9.1: A horizontal cross-section showing a distribution of $\langle T_{eff} \rangle_t$ evaluated at $z = 0$ for $Ra_{eff} = 1.59 \times 10^7$ and LCP-rad (a), LCP (b), ITP-nh (c) and ITP (d). Note that the time and area-averaged temperature equals 0.5 for all considered cases, and the spatial temperature distribution for ITP-nh is obtained by time-averaging the temperature distribution for LCP.

(herein referred as the spatial non-homogeneity of the temperature distribution) and the temporal fluctuation of the temperature distribution, i.e.

$$\langle T_{eff,rms} \rangle_{S_z} = \langle \sqrt{\langle (T_{eff} - \langle T_{eff} \rangle_t)^2 \rangle_t} \rangle_{S_z}. \tag{9.2}$$

The above quantities are collected in Table 9.1 for all considered Rayleigh numbers and boundary conditions.

For isothermal BC represented by ITP, $\langle T_{eff,\delta_{S_z}} \rangle_t$ equals zero. If the complexity level of BCs increases, and the temperature at the interfaces varies in space (ITP-nh), $\langle T_{eff,\delta_{S_z}} \rangle_t = 0.0308$ for $Ra_{eff} = 1.59 \times 10^7$. If the complexity level of BCs increases even further, and radiation is taken into account (LCP-rad), $\langle T_{eff,\delta_{S_z}} \rangle_t = 0.0252$ for $Ra_{eff} = 1.59 \times 10^7$. Thus, increasing the complexity level may increase or decrease the spatial non-homogeneity of the temperature distribution. Similar behaviour is observed for temporal temperature fluctuations at the interface. If $Ra_{eff} = 1.59 \times 10^7$, they equal zero for ITP and ITP-nh, 0.0020 for LCP and 0.0016 for LCP-rad.

Due to the above, the main question about the dependency of the coherent structures on the simplicity level of the BCs boils down to the question about the dependency of the coherent structures on the spatial non-homogeneity and temporal fluctuations of the temperature distribution at the interface.

It is noteworthy that the mean spatial and temporal temperature fluctuations constitute at maximum 6.2% and 0.4% of the time- and area-averaged temperature at the interface, respectively. This is the case for $Ra_{eff} = 1.59 \times 10^7$. Although these deviations seem to be quite small, especially the temporal ones, they are still relatively large with respect to the considered Rayleigh number and low conductivity of the plates. Indeed, they would be even smaller for higher plates' conductivity.

9.1.1 Sheet-like plumes extraction

In order to study how the aforementioned BCs alter the coherent structures, which are developed within the thermal boundary layer, it is inevitable to at first identify the sheet-like thermal plumes. While Zhou et al. (2007) were able to visualise the sheet-like plumes in horizontal cross-section of the cylindrical RB cell using thermochromic liquid crystal microspheres, Shishkina and Wagner (2008) proposed a quantitative method to obtain the temperature threshold T_{thr}, which separates the sheet-like plumes from the turbulent background in a cylindrical container filled with water. The latter authors evaluated their procedure for $Ra = 2 \times 10^9$ and $Ra = 2 \times 10^{10}$ and analysed the temperature dependencies of the conditionally averaged plume characteristics. They observed a well-pronounced extremum of the conditionally averaged thermal dissipation rate at the certain temperature when evaluating the DNS data at the distance

of one thermal boundary layer thickness away from the bottom and top plates. Furthermore, they related this temperature to the threshold temperature T_{thr}, which determines the border between the sheet-like plumes and the turbulent background. Additionally, they found that SLP are characterised by high absolute values of the temperature and heat flux.

In the present study, the RB cell is cuboidal and is filled with air. Also the Ra_{eff} are lower than the ones in Shishkina and Wagner (2008). Nevertheless, Figure 9.2 shows that at the border between the thermal boundary layer and the bulk, i.e. at z=$0.5H/Nu_{c,eff}$, the highest values of the instantaneous temperature and convective heat flux can be found inside the sheet-like plumes, which is in agreement with Shishkina and Wagner (2008). Moreover, the highest values of the thermal dissipation rate

$$\epsilon_{T,eff} = \kappa_f \left(\nabla T_{eff}\right)^2 \tag{9.3}$$

coincide with the borders of SLP, which is also in agreement with Shishkina and Wagner (2008). Therefore, the method for the sheet-like plumes extraction, proposed by Shishkina and Wagner (2008), is challenged in the herein studied RB cell. Finally, the considered conditionally averaged function of the thermal dissipation rate is obtained by the time-averaging of $\epsilon_{T,eff}$ over $\sim$250 time units with sampling interval 0.25 time unit, and over those parts of the horizontal cross-section S_z at z=$0.5H/Nu_{c,eff}$ which correspond to the temperature interval $[T_k, T_{k+1}[$ as follows

$$\bar{\epsilon}_{T,eff}\left(T_k \leqslant T_{eff} < T_{k+1}\right) = \frac{\langle \epsilon_{T,eff} \vartheta\left(T_k \leqslant T_{eff} < T_{k+1}\right)\rangle_{t,S_z}}{\langle \vartheta\left(T_k \leqslant T_{eff} < T_{k+1}\right)\rangle_{t,S_z}}, \tag{9.4}$$

where

$$\vartheta\left(T_k \leqslant T_{eff} < T_{k+1}\right) = \mathscr{H}(T_{eff} - T_k) - \mathscr{H}(T_{eff} - T_{k+1}) \tag{9.5}$$

with $\mathscr{H}(x)$ the Heaviside function, i.e. $\mathscr{H}(x) = 1$ if $x \geqslant 0$ and $\mathscr{H}(x) = 0$ otherwise. Figure 9.3 indeed shows a well-pronounced peak of $\bar{\epsilon}_{T,eff}$ for all considered Rayleigh numbers, which clearly can provide the desired threshold.

All the quantities regarding a sheet-like plume are denoted with index $\mathscr{P}$. Moreover, the mean area of the sheet-like plumes identified in the entire horizontal cross-section S_z for all instantaneous fields, reads

$$\langle A^{\mathscr{P}}\rangle_{S_{\mathscr{P}}} = \{(x,y) \in S_z : T_{eff}(x,y) \in [T_{thr}, 0.5]\}, \quad z = 0.5H/Nu_{c,eff}. \tag{9.6}$$

Here, the vertical coordinate z and time t as well as averaging over time are omitted.

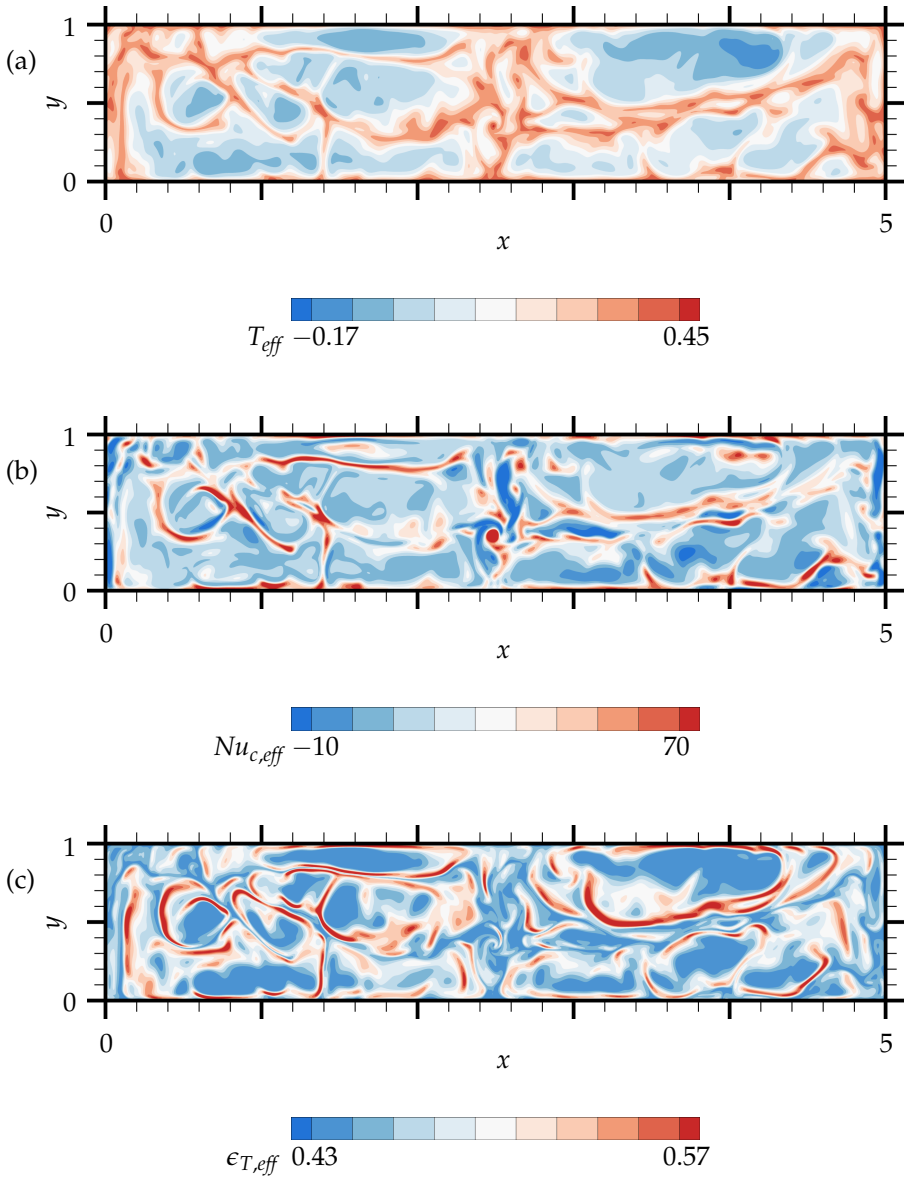

FIGURE 9.2: The instantaneous distributions of the temperature T_{eff} (a) convective Nusselt number $Nu_{c,eff}$ (b) and thermal dissipation rate $\epsilon_{T,eff}$ (c) evaluated at z=0.5$H/Nu_{c,eff}$ for $Ra_{eff} = 1.59 \times 10^7$ and ITP.

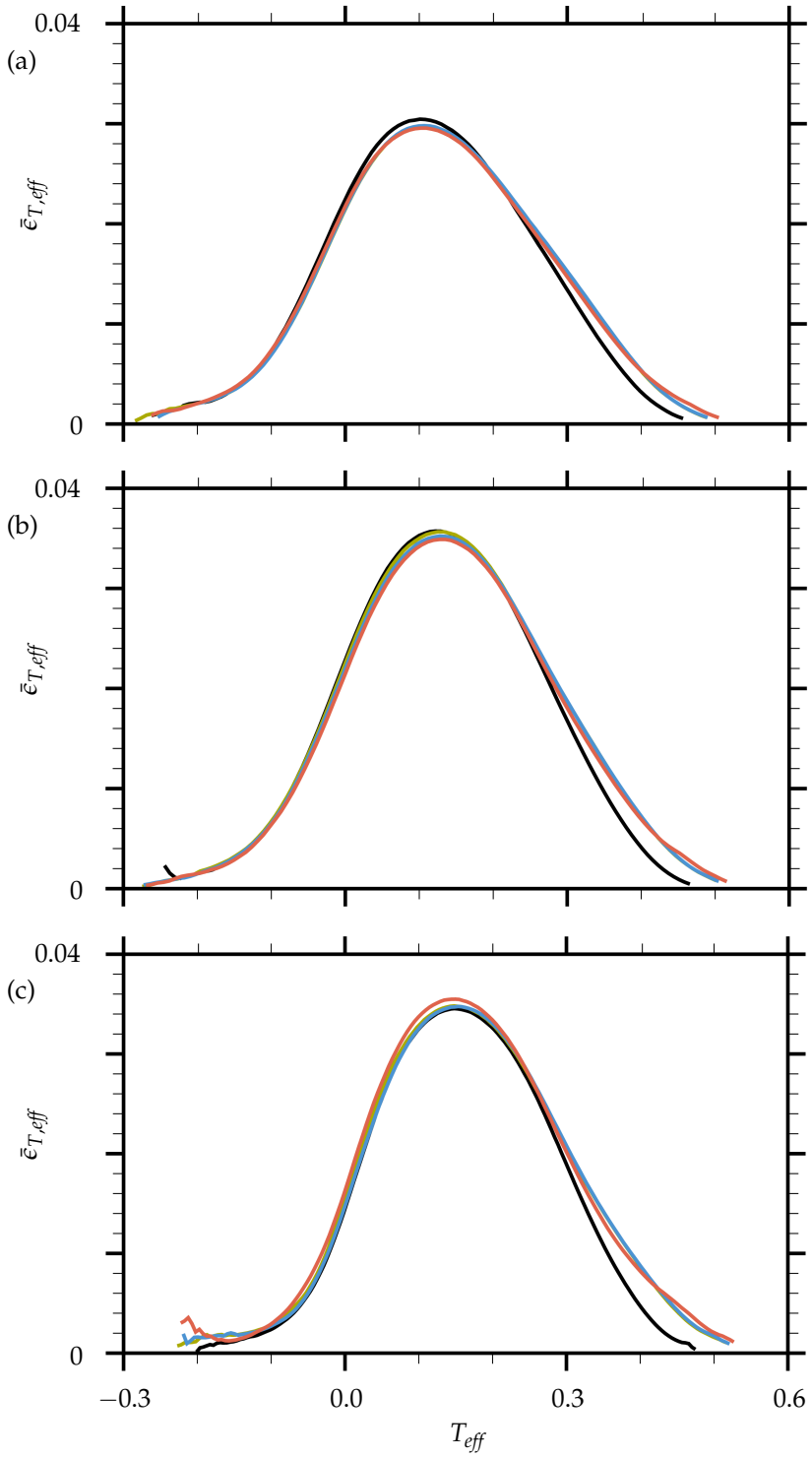

FIGURE 9.3: The conditionally averaged thermal dissipation rate $\bar{\epsilon}_{T,eff}$, evaluated at z=0.5$H/Nu_{c,eff}$ for $Ra_{eff} = 3.17 \times 10^5$ (a), $Ra_{eff} = 1.05 \times 10^6$ (b), $Ra_{eff} = 1.59 \times 10^7$ (c); LCP-rad, LCP, ITP-nh, ITP.

9.1.2 Mean threshold temperature

Figure 9.3 shows the conditionally averaged thermal dissipation rate $\bar{\epsilon}_{T,eff}$ for low, medium and high turbulence, which correspond to $Ra_{eff} = 3.17 \times 10^5$, $Ra_{eff} = 0.92 \times 10^6$ and $Ra_{eff} = 1.59 \times 10^7$, respectively. The temperatures, which represent the peak values of $\bar{\epsilon}_{T,eff}$ reflect the mean threshold temperatures. They are collected in Table 9.2 revealing that within one effective Rayleigh number they are very similar for all considered types of the boundary condition. Thus, the mean temperature, above which the development of thermal plumes statistically starts, is barely sensitive to the variations of the spatial non-homogeneity and temporal instability of the temperature distribution at the interfaces.

When Ra_{eff} increases, the mean temperature threshold increases equally for all studied BCs reaching $T_{thr} = 0.15$ for $Ra_{eff} = 1.59 \times 10^7$ so that warmer and more energetic plumes can be developed. Since the upper bound temperature is nearly constant for all Ra_{eff} and BCs, the rapidly growing T_{thr} leads to a shorter temperature range of SLP, which means smaller flow structures for higher turbulence for all BCs.

9.1.3 Mean temperature and area of the sheet-like plumes

The dependency of the coherent structures on the spatial non-homogeneity of the temperature distribution at the bottom interface is studied by comparing the mean temperature of SLP

$$\langle T^{\mathscr{P}} \rangle_{S_{\mathscr{P}}} = \frac{1}{\sum_{\mathscr{P} \in S_{\mathscr{P}}} A^{\mathscr{P}}} \int \int_{S_{\mathscr{P}}} T_{eff}\,(x,y)\, dS_{\mathscr{P}}. \tag{9.7}$$

Here, $S_{\mathscr{P}}$ denotes the surface of all sheet-like plumes identified in S_z, z=$0.5H/Nu_{c,eff}$ for all instantaneous fields. The above characteristics of the coherent structures are collected in Table 9.2 for all considered BCs and Ra_{eff}.

For any Ra_{eff}, $\langle T^{\mathscr{P}} \rangle_{S_{\mathscr{P}}}$ and $\langle A^{\mathscr{P}} \rangle_{S_{\mathscr{P}}}$ are respectively ∼3% smaller and greater for isothermal BC than for any non-isothermal ones. Thus, when any non-homogeneous temperature distribution at the interface is replaced by its simplified isothermal representation, i.e. ITP, the predicted sheet-like plumes are colder and larger.

The above finding, regarding the temperature of SLP, is explained with the help of Figure 9.4, which illustrates the PDF of the sheet-like plumes' temperature for all considered BCs and Ra_{eff}.

The shape of the PDFs and their behaviour with increasing Ra_{eff} suggest that the sheet-like plumes can be divided into three regions. The first one corresponds to SLP or their part, which temperatures are roughly below $\langle T^{\mathscr{P}} \rangle_{S_{\mathscr{P}}}$. The abbreviation SLP_I refers to these plumes. The second region corresponds to

	Ra_{eff}	T_{thr}	$\langle A^{\mathscr{P}} \rangle_{S_{\mathscr{P}}}$	$\langle T^{\mathscr{P}} \rangle_{S_{\mathscr{P}}}$	$\langle T^{\mathscr{P}}_{rms} \rangle_{S_{\mathscr{P}}}$	$\langle Nu^{\mathscr{P}} \rangle_{S_{\mathscr{P}}}$	$\langle Nu^{\mathscr{P}} \rangle_{S_{\mathscr{P}}} / \langle Nu_{c,eff} \rangle_{S_z}$ [%]
LCP-rad	3.17×10^5	0.10	2.59	0.249	0.094	7.48	63.66
LCP		0.11	2.60	0.252	0.094	7.46	63.78
ITP-nh		0.11	2.60	0.252	0.094	7.48	63.81
ITP		0.10	2.67	0.246	0.089	7.31	64.66
LCP-rad	0.92×10^6	0.13	2.62	0.266	0.088	10.58	66.68
LCP		0.13	2.62	0.267	0.088	10.67	66.51
ITP-nh		0.13	2.62	0.266	0.088	10.66	66.16
ITP		0.12	2.72	0.259	0.084	10.35	67.83
LCP-rad	1.59×10^7	0.15	2.30	0.264	0.077	28.45	70.07
LCP		0.15	2.19	0.268	0.077	28.59	69.21
ITP-nh		0.15	2.24	0.266	0.077	28.54	69.60
ITP		0.15	2.32	0.263	0.073	28.23	71.75

TABLE 9.2: Characteristics of the sheet-like plumes.

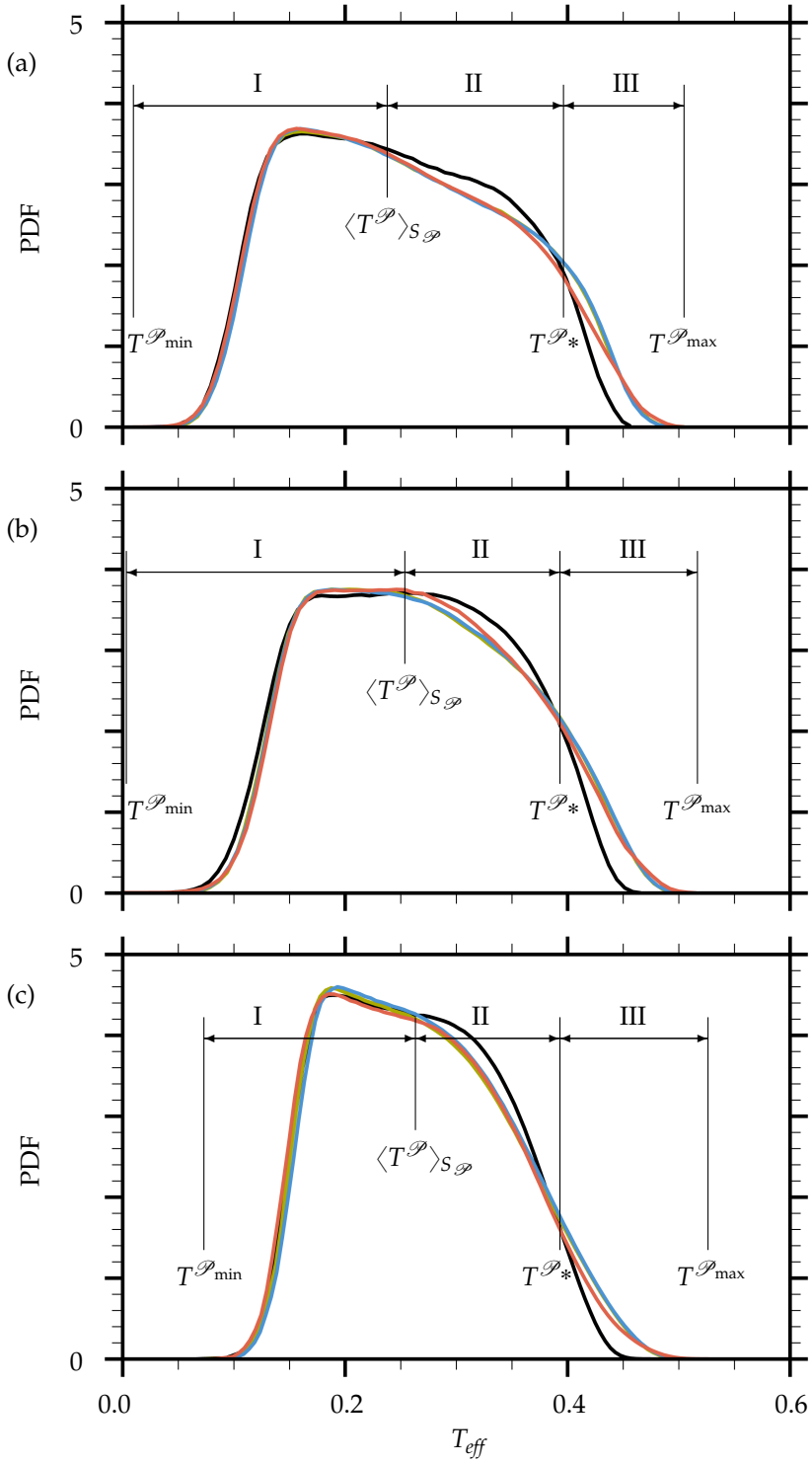

FIGURE 9.4: The probability density function of the temperature of the sheet-like thermal plumes, evaluated for $Ra_{eff} = 3.17 \times 10^5$ (a), $Ra_{eff} = 1.05 \times 10^6$ (b), $Ra_{eff} = 1.59 \times 10^7$ (c) at distance z=0.5$H/Nu_{c,eff}$; LCP-rad, LCP, ITP-nh, ITP. Note that the location of $\langle T^{\mathscr{P}} \rangle_{S_{\mathscr{P}}}$ is approximate since the actual value depends on the type of BC.

the plumes, of which temperatures are moderate. The upper separation point $T^{\mathscr{P}}*$ of this region is defined by the point, where the PDFs for all BCs intersect with each other. The abbreviation SLP_{II} refers to plumes from this region. The third region corresponds to the warmest SLP, i.e. the ones which temperatures are greater than $T^{\mathscr{P}}*$. Additionally, since the core of the plume is always hotter than its outer layer, this region represents especially the interior of SLP, and the greatest value in this region, i.e. $T^{\mathscr{P}_{\max}}$, states for the maximal core temperature. The abbreviation SLP_{III} is used to refer to these plumes.

Figure 9.4 further shows that in the first region, the PDFs nearly overlap for isothermal and non-isothermal BCs for all studied Ra_{eff}. Thus, the coherent structures represented by this region are not responsible for the observed change in $\langle T^{\mathscr{P}} \rangle_{S_{\mathscr{P}}}$. On the other hand, considering the second region, the PDF obtained for the isothermal BC lies above those obtained for the non-isothermal BCs. In order to quantitatively measure this trend, the integration of the PDFs over the interval $[\langle T^{\mathscr{P}} \rangle_{S_{\mathscr{P}}}, T^{\mathscr{P}}*]$ is performed. Finally, it is noticed that the production of the moderately warm SLP increases by 7.6% for $Ra_{eff} = 1.59 \times 10^7$ with a change of the BCs from the non-isothermal to the isothermal ones. Moreover, the opposite trend is observed in region III. Here, the production of the warmest SLP decreases by a factor of 2.1 for $Ra_{eff} = 1.59 \times 10^7$ with the same change of the BCs. The latter is empowered by a decrease of the sheet-like plumes' core temperature as indicated by a decrease of $T^{\mathscr{P}_{\max}}$ from 0.517 to 0.475 for $Ra_{eff} = 1.59 \times 10^7$.

All in all, $\langle T^{\mathscr{P}} \rangle_{S_{\mathscr{P}}}$ is colder for ITP because isothermal BCs cause overproduction of SLP_{II} and underproduction of SLP_{III}.

Before relating the underproduction of plumes from region III to the temperature distribution at the bottom interface, it is essential first to distinguish the contribution of the temporal temperature fluctuations at the interface to $\langle T^{\mathscr{P}} \rangle_{S_{\mathscr{P}}}$ from the contribution of the spatial non-homogeneity of the temperature distribution at the interface to $\langle T^{\mathscr{P}} \rangle_{S_{\mathscr{P}}}$.

The influence of the temporal fluctuations of the temperature at the bottom interface on the mean temperature of SLP is examined with the help of Table 9.2. Since ITP-nh and LCP reflect the same spatial temperature distribution but different temporal fluctuations of the temperature at the interface, they are chosen for this analysis. For low and medium turbulence, i.e. $Ra_{eff} \leqslant 1.05 \times 10^6$, $\langle T^{\mathscr{P}} \rangle_{S_{\mathscr{P}}}$ obtained for ITP-nh and LCP are similar. For $Ra_{eff} = 1.59 \times 10^7$ the mean temperature of SLP is less than 2% greater for LCP than for ITP-nh. Therefore, it is concluded that the temporal fluctuations of the temperature at the interfaces do not significantly influence the mean temperature of SLP in the considered Ra range. This might be however conditioned by low temperature fluctuations at the interface, which for the considered simulations are less than 0.002.

In the following, the relation between the production of the considered SLP

and the spatial non-homogeneity of the temperature distribution at the interface is analysed. For the sake of clarity, the analysis is limited to $Ra_{eff} = 1.59 \times 10^7$.

At first, ITP-nh and ITP are considered since they reflect a zero temporal fluctuations of temperatures at the interfaces, but non-zero and zero temperature spatial fluctuations $\langle T_{eff,\delta_{S_{z=0}}} \rangle_t$, respectively. To identify the places where SLP_{III} occur for both considered BCs at the cross-section S_z, z=$0.5H/Nu_{c,eff}$, the 2D PDFs of the SLP_{III} temperature are plotted in Figure 9.5. Since the PDFs reflect similar structures, the SLP_{III} are produced in similar locations independently of the homogeneity of the temperature distribution at the interface. However, the probability of finding temperature values in the centre and close to the lateral walls satisfying $T^{\mathscr{P}}{}_* \leqslant T^{\mathscr{P}} \leqslant T^{\mathscr{P}_{\max}}$ is twice as low for ITP than for ITP-nh. Thus, the production of the hottest SLP decreases in these locations if the isothermal BCs are employed instead of the non-isothermal ones.

Now, lets relate the locations, where the aforementioned underproduction of SLP occurs, to the temperature distribution at the bottom interface. This is done by superimposing the temperature distribution at the interface for ITP-nh (Figure 9.1c) to the 2D PDF of the SLP_{III} temperature at z=$0.5H/Nu_{c,eff}$ (Figure 9.5c). The analogical superimposition is done for ITP, i.e. Figure 9.1d is superimposed to Figure 9.5d. Comparing the resulting plot for ITP-nh with the one for ITP, it is found that wherever the temperature at the interface drops with a change of the BCs, the production of SLP_{III} decreases in the corresponding region at z=$0.5H/Nu_{c,eff}$. Thus, replacing the non-homogeneous temperature distribution by its simplified isothermal representation leads to the underproduction of the warmest SLP in the corresponding regions at the border of the thermal BL.

Since the temperature distribution at the bottom interface is different in the absence and presence of radiation, it is of interest to verify how the level of spatial non-homogeneity of the temperature distribution at the interface affects the production of SLP_{III}.

Therefore, LCP and LCP-rad are considered, and the superimpositions of the temperature distributions at the interface (Figure 9.1) to the corresponding 2D PDFs of SLP_{III} temperature at z=$0.5H/Nu_{c,eff}$ (Figure 9.5) are conducted. The resulting plots show that the temperatures in the centre of the bottom interface are higher in the absence of radiation (LCP) than in the presence of it (LCP-rad). Also the local PDFs of $T^{\mathscr{P}} \in \langle T^{\mathscr{P}}{}_*, T^{\mathscr{P}_{\max}} \rangle$ are greater there in the absence of radiation. On the other hand, the temperatures in the four corners of RB cell and the corresponding PDFs are smaller for LCP than for LCP-rad. Thus, the production of SLP_{III} strongly depends on the shape of the temperature distribution at the interface so that lower temperatures at the interface cause underproduction and higher ones cause overproduction of the warmest SLP.

In order to have a clear picture how the differences in the temperature distributions at $z = 0$ are linked to the change in the SLP production at

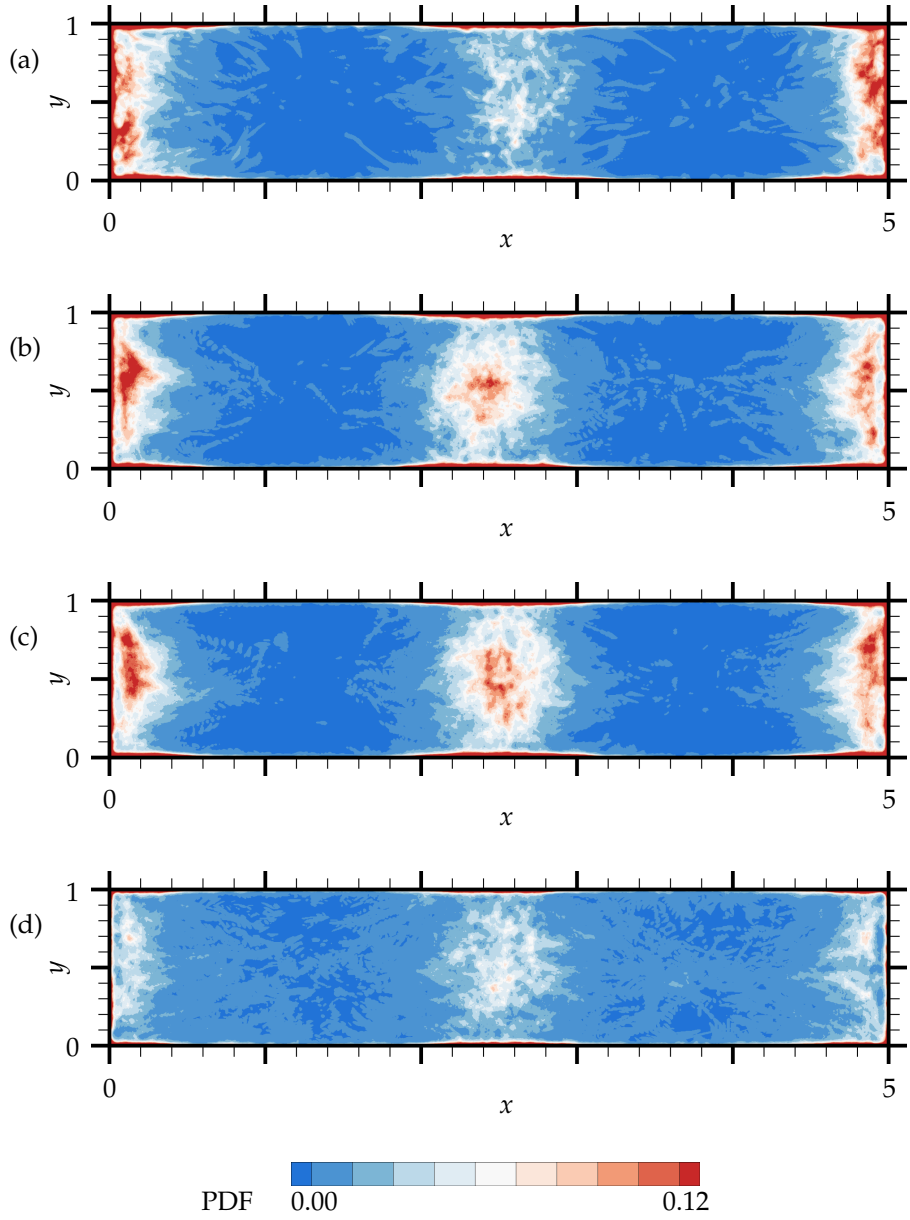

FIGURE 9.5: The probability density function of the temperature $T_{eff} \in \langle T^{\mathscr{P}*}, T^{\mathscr{P}_{\max}} \rangle \equiv \langle 0.40, 0.53 \rangle$ of the sheet-like thermal plumes, evaluated for $Ra_{eff} = 1.59 \times 10^7$ at distance $z{=}0.5H/Nu_{c,eff}$; LCP-rad (a), LCP (b), ITP-nh (c), ITP (d).

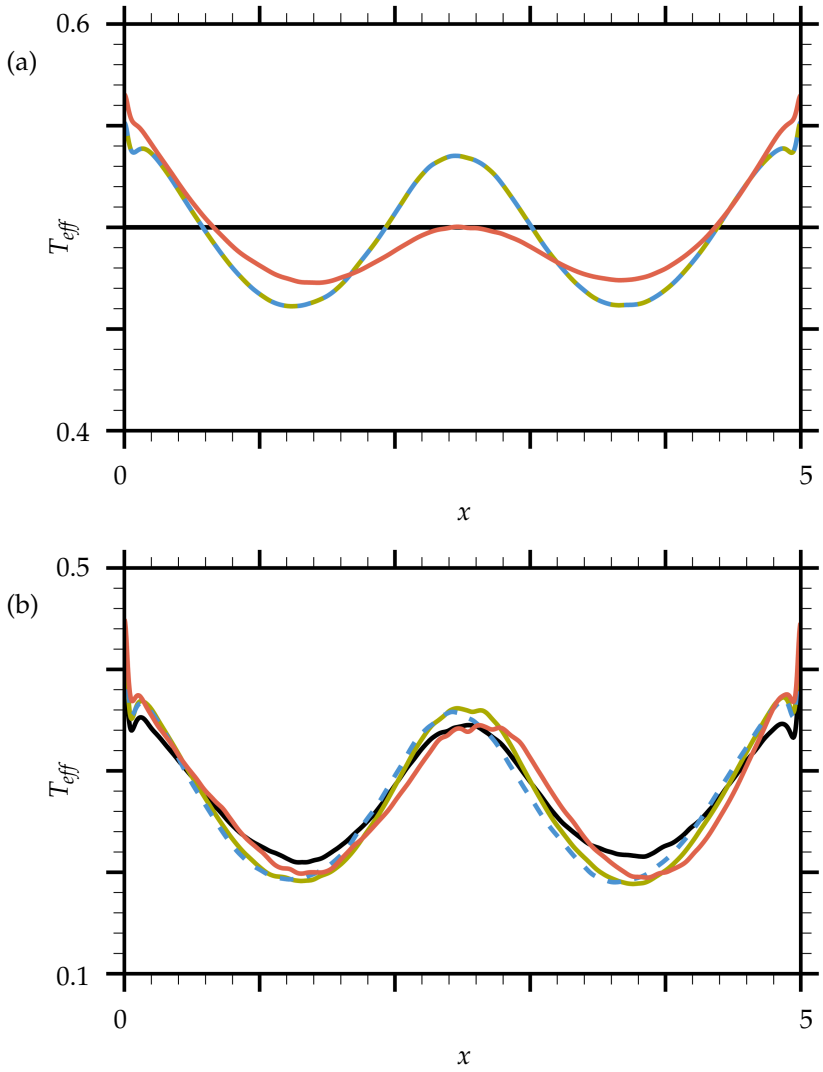

FIGURE 9.6: The time-averaged temperature profile, evaluated along the lengthwise wall at $y = 0.5W$ and $z = 0$ (a) and z=$0.5H/Nu_{c,eff}$ (b) for $Ra_{eff} = 1.59 \times 10^7$; LCP-rad, LCP, ITP-nh, ITP.

z=$0.5H/Nu_{c,eff}$, it is of interest to look at the temperature profiles evaluated at $z = 0$ and z=$0.5H/Nu_{c,eff}$. Thus, the time- and widthwise-averaged profiles of temperature $\langle T_{eff} \rangle_{t,y}$ evaluated at these heights are plotted in Figure 9.6 for all considered BCs. They show that the non-isothermal BCs as well as the isothermal one reflect the sinusoidal-like profiles at z=$0.5H/Nu_{c,eff}$. However, wherever the temperature at $z = 0$ is greater for one type of BC than for the other one, it is also greater at z=$0.5H/Nu_{c,eff}$. Simultaneously, wherever the temperature at $z = 0$ is equal for two types of BC, e.g. in the centre of the cross-section S_z for ITP and LCP-rad, the amplitude of oscillations of $\langle T_{eff} \rangle_{t,y}$

is also equal at z=0.5$H/Nu_{c,eff}$. Thus, the amplitude of oscillations of $\langle T_{eff}\rangle_{t,y}$ at z=0.5$H/Nu_{c,eff}$ is proportional to the temperature at the corresponding location at $z = 0$, i.e. at the interface. Then, since the oscillations of $\langle T_{eff}\rangle_{t,y}$ at z=0.5$H/Nu_{c,eff}$ reflect the spatial non-homogeneity of the temperature distribution caused by SLP, the temperature of SLP at z=0.5$H/Nu_{c,eff}$ is also proportional to the temperature at the interface. Moreover, the probability of finding the warmest SLP at z=0.5$H/Nu_{c,eff}$ is proportional to the maximal temperature at the corresponding location at $z = 0$. Finally, it becomes clear that the local production of the warmest SLP at z=0.5$H/Nu_{c,eff}$ is lower for isothermal BC than for non-isothermal ones because the local temperatures at the corresponding locations at the interface are lower.

The effect of the non-uniformly heated bottom plate on the temperature field was also discussed by Basak et al. (2006) and Aswatha et al. (2011). They considered a 2D cavity bounded by adiabatic top plate and constant temperature cold side walls. Moreover, the bottom plate was once subjected to a sinusoidally varying temperature with a maximum and minimum in the centre and at the side walls, respectively, and twice to a constant temperature. Comparing the results presented in terms of the stream function and isotherms revealed similar circulation patterns for both considered heating scenarios. However, the temperatures close to the side walls and in the centre of the cell were decreased and increased due to non-uniform heating, respectively. The latter is in agreement with the findings from the present study.

Furthermore, Freund et al. (2011) studied 2D RBC exposed to sinusoidal heating at the lower plate and constant cooling at the upper one. They noticed that the maximal up-flow occurs at the maxima of the temperature modulation, which agrees with the present study.

The influence of the Rayleigh number on the mean temperature of SLP is studied with the help of Table 9.2. It reveals a slow increase of $\langle T^{\mathscr{P}}\rangle_{S_{\mathscr{P}}}$ with increasing the Rayleigh number independently of the applied BCs. This is explained using Figure 9.4. When the Rayleigh number increases, the coldest SLP become warmer, and the warmest SLP possess similar temperature, which is represented by the narrower PDF. This finally leads to the increase of the threshold temperature T_{thr} and the mean temperature of the sheet-like plumes $\langle T^{\mathscr{P}}\rangle_{S_{\mathscr{P}}}$.

Table 9.2 is further used to study the influence of the Rayleigh number on the size of the sheet-like plumes. It reveals that for any considered BCs, the mean area of SLP decreases with increasing the Rayleigh number constituting lower contribution to the total fluid area at z=0.5$H/Nu_{c,eff}$. For example, when isothermal BCs are employed, SLP occupy 53% and 46% of the total area for

$Ra_{eff} = 3.17 \times 10^5$ and $Ra_{eff} = 1.59 \times 10^7$, respectively. Thus, thermal plumes become smaller and less visible for higher turbulence at the expense of turbulent background. A similar conclusion was drawn by Shishkina and Wagner (2006) who studied RBC in a wide cylindrical container and noted that the portion of the whole domain, which corresponds to the turbulent background increases with the Rayleigh number.

9.1.4 Temperature fluctuations of the sheet-like plumes

Since the temperature fluctuations are caused by thermal plumes, which production depends on the non-homogeneity of the interface temperature distribution, it is expected that the mean temperature fluctuation of the SLP

$$\langle T^{\mathscr{P}}_{rms} \rangle_{S_{\mathscr{P}}} = \sqrt{\frac{1}{\sum_{\mathscr{P} \in S_{\mathscr{P}}} A^{\mathscr{P}}} \int\int_{S_{\mathscr{P}}} \left(T_{eff}\,(x,y) - \langle T^{\mathscr{P}} \rangle_{S_{\mathscr{P}}} \right)^2 dS_{\mathscr{P}}} \tag{9.8}$$

evaluated at z=0.5$H/Nu_{c,eff}$ changes with varying the temperature distribution at $z = 0$ (the bottom interface). In order to verify the above, $\langle T^{\mathscr{P}}_{rms} \rangle_{S_{\mathscr{P}}}$ are calculated for all considered BCs and collected in Table 9.2.

Comparing $\langle T^{\mathscr{P}}_{rms} \rangle_{S_{\mathscr{P}}}$ obtained for ITP (isothermal BC) and $Ra_{eff} = 1.59 \times 10^7$ with the one for ITP-nh (non-isothermal BC) reveals that the mean temperature fluctuation of SLP increases by 6% as the mean temperature standard deviation $\langle T_{eff,\delta_{S_{z=0}}} \rangle_t$ (Table 9.1) grows at the interface from zero to 0.03. This means that applying the most simplified BC, i.e. isothermal BC, leads to the underprediction of the mean sheet-like plumes' temperature fluctuation.

The difference in $\langle T^{\mathscr{P}}_{rms} \rangle_{S_{\mathscr{P}}}$ predictions is explained with the help of Figure 9.7 which shows the probability density function of the SLP' temperature fluctuations for $Ra_{eff} = 1.59 \times 10^7$. There, the probability to find the fluctuations lower than $\langle T^{\mathscr{P}}_{rms} \rangle_{S_{\mathscr{P}}}$ is up to 19% greater for ITP than for ITP-nh. Relating these fluctuations to the certain group of plumes using figure 9.4 suggests that these fluctuations are caused by SLP_I and SLP_{II}, and hence these plumes determine $\langle T^{\mathscr{P}}_{rms} \rangle_{S_{\mathscr{P}}}$. On the other hand, the probability to find the fluctuations greater than $\langle T^{\mathscr{P}}_{rms} \rangle_{S_{\mathscr{P}}}$ is similar for both heating scenarios, especially in the range of very high $T^{\mathscr{P}}_{rms}$. Since these fluctuations are mainly caused by SLP_{III}, the latter do not determine the mean sheet-like plumes' temperature fluctuation.

Furthermore, Tables 9.1 and 9.2 show that $\langle T^{\mathscr{P}}_{rms} \rangle_{S_{\mathscr{P}}}$ are the same for ITP-nh and LCP even though the temporal temperature fluctuations at the interface are different for these BCs while the spatial ones are the same. For example, when $Ra_{eff} = 1.59 \times 10^7$, $\langle T_{eff,rms} \rangle_{S_{z=0}}$ equals zero and 0.002 for ITP-nh and LCP, respectively. Since also the PDF profiles in Figure 9.7 collapse for these BCs in the entire range of $T^{\mathscr{P}}_{rms}$, it can be concluded that the temporal fluctuations at

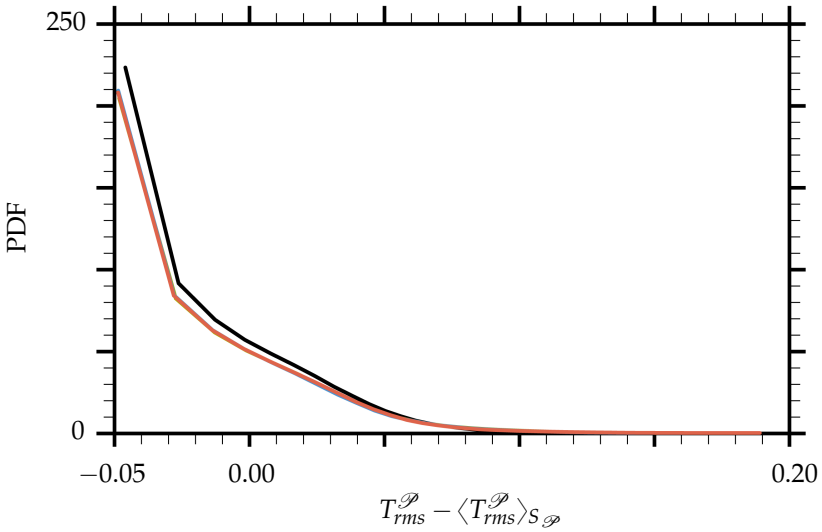

FIGURE 9.7: The probability density function of the sheet-like plumes' temperature fluctuations, evaluated for $Ra_{eff} = 1.59 \times 10^7$ at distance z=0.5$H/Nu_{c,eff}$; LCP-rad, LCP, ITP-nh, ITP.

the interface do not affect the local and mean fluctuations of the SLP. The latter might however occur because the time response of a system is longer than the period of the temperature fluctuations at the interface.

Tables 9.1 and 9.2 further show that $\langle T^{\mathscr{P}}_{rms} \rangle_{S_{\mathscr{P}}}$ are the same also for LCP and LCP-rad even though the spatial and temporal temperature fluctuations at the interface are different for these BCs. Thus, not all the temperature fluctuations at the interface are related to plumes, which was also suggested by Verzicco and Sreenivasan (2008).

Having a closer look on the local temperature fluctuations of the SLP for $Ra_{eff} = 1.59 \times 10^7$ (Figure 9.7) as well as for $Ra_{eff} = 1.05 \times 10^6$ and $Ra_{eff} = 3.17 \times 10^5$ in Figures 9.8a and 9.8b, respectively, discloses that for any Rayleigh number $T^{\mathscr{P}}_{rms}$ is the highest for the most complex BC, i.e. LCP-rad. It is noteworthy that the mean temperature standard deviation $\langle T_{eff,\delta_{S_{z=0}}} \rangle_t$ evaluated at the interface is not the greatest for LCP-rad. Indeed, it is lower than the one for LCP and ITP-nh and greater than $\langle T_{eff,\delta_{S_z}} \rangle_t$ for ITP. For example, for $Ra_{eff} = 1.59 \times 10^7$, $\langle T_{eff,\delta_{S_{z=0}}} \rangle_t = 0.0224$ for LCP-rad and 0.0315 for LCP (see Table 9.1). The above might come from the fact that $T^{\mathscr{P}}_{rms}$ depends on the maximal local temperature at the interface. The latter is verified by comparing the probability density function obtained for $Ra_{eff} = 1.59 \times 10^7$ from a time series of 2D interface temperature distributions (∼250 time units with sampling interval 0.25 time unit). They are plotted in Figure 9.9 revealing that the highest local temperature at the interface exists in the case of LCP-rad and equals 0.59.

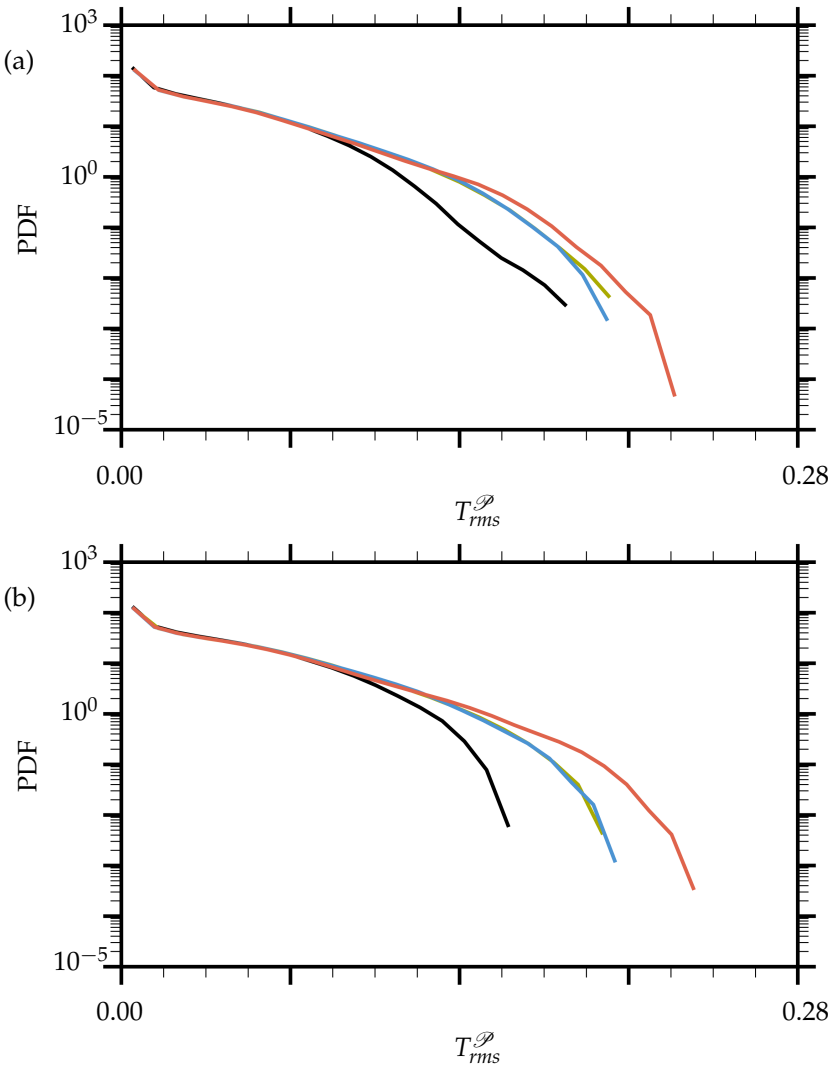

FIGURE 9.8: The probability density function of the sheet-like plumes' temperature fluctuations, evaluated for $Ra_{eff} = 1.05 \times 10^6$ (a) and $Ra_{eff} = 3.17 \times 10^5$ (b) at distance z=0.5$H/Nu_{c,eff}$; LCP-rad, LCP, ITP-nh, ITP.

On the other hand, since the PDF profiles obtained for LCP and ITP-nh nearly collapse, the maximal interface temperatures are similar for these cases and equal $T_{\max} = 0.58$. Although PDF for ITP is not included in Figure 9.9, the maximal local temperature is of course 0.50, and hence it is the lowest. Additionally, the 2D time-averaged temperature distributions in Figure 9.1 clearly illustrate that unless the distribution is isothermal, the highest temperatures are located in small regions close to the widthwise walls, where SLP_{III} are likely created. Thus, the increase of the system complexity leads to the increase of the maximal local temperature in the regions where SLP_{III} are likely created and eventually of the local production of the SLP. The latter is responsible for higher

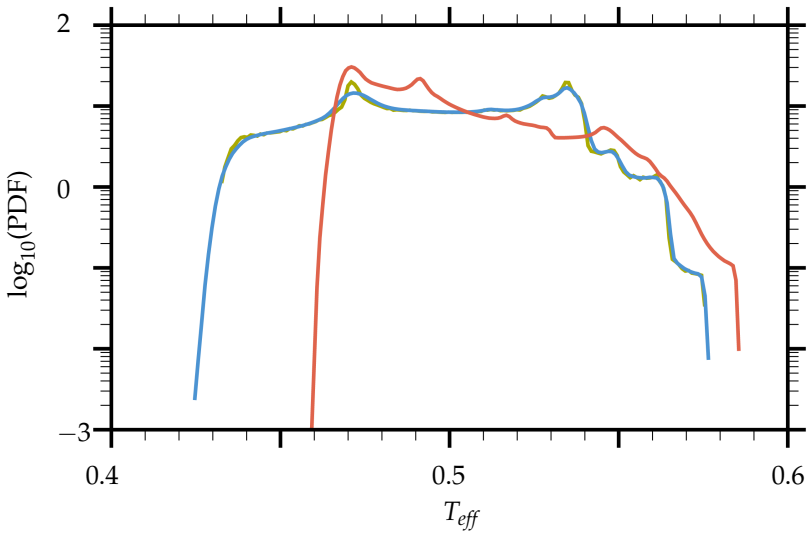

FIGURE 9.9: The temperature probability density function evaluated for $Ra_{eff} = 1.59 \times 10^7$ at the bottom interface; LCP-rad, LCP, ITP-nh. Note that the PDF for ITP is not included because of the constant temperature $T_{eff} = 0.5$.

fluctuations of the SLP' temperature, which is consistent with Hunt et al. (2003).

The dependency of the sheet-like plumes' temperature fluctuations on the Rayleigh number is examined with the help of Table 9.2. It shows that for all considered BCs $\langle T'^{\mathscr{P}}_{rms} \rangle_{S_{\mathscr{P}}}$ evaluated at $z{=}0.5H/Nu_{c,eff}$ decreases by 18% with increasing Ra from $Ra_{eff} = 3.17 \times 10^5$ to $Ra_{eff} = 1.59 \times 10^7$. Furthermore, Table 9.1 shows that the corresponding homogeneity of the temperature distribution at the interface increases by a factor of 1.28 with equal increase of Ra. Hence, increasing the Rayleigh number leads to the lower temperature fluctuations of SLP spotted at the border between the BL and the bulk but greater fluctuations of the temperature distribution at the interface.

Since for all BCs the threshold temperature T_{thr} increases with the considered increase of Ra by $\sim$0.04 and determines the minimal plumes' temperature $T^{\mathscr{P}_{\min}}$, the latter also increases with Ra by $\sim$0.04. Simultaneously, the maximal temperature at the bottom interface, which determines the maximal plumes' temperature $T^{\mathscr{P}_{\max}}$, increases by $\sim$0.01 with Ra for all BCs. Thus, the range of the SLP' temperature shrinks with Ra independently of the BCs, and the SLP have less freedom to change their temperature. On the contrary, the temperature fluctuations at the bottom interface increase because the temperature differences between the descending plumes and the hot interface increases with increasing Rayleigh number.

9.1.5 Convective heat flux of the sheet-like plumes

In order to analyse how the vertical heat flux of the SLP varies with a change of the temperature BCs, the convective Nusselt number calculated over the SLP $\langle Nu_c^{\mathscr{P}} \rangle_{S_{\mathscr{P}}}$ is listed in Table 9.2. Considering isothermal (ITP) and non-isothermal heating (ITP-nh), $\langle Nu_c^{\mathscr{P}} \rangle_{S_{\mathscr{P}}}$ is 2.3% greater for non-isothermal BC and $Ra = 3.17 \times 10^5$. For higher Rayleigh numbers the behaviour is similar. For $Ra_{eff} = 1.59 \times 10^7$ $\langle Nu_c^{\mathscr{P}} \rangle_{S_{\mathscr{P}}}$ is 1.1% greater. Finally, it can be concluded that the Nusselt number of the SLP is underestimated if a simplified isothermal BC is applied.

The latter is explained with the help of the temperature distribution at the interface (Figure 9.1c–9.1d) and the corresponding convective Nusselt number plotted in Figure 9.10a–9.10b. They reveal that wherever the local temperature is greater for ITP-nh, the corresponding local Nusselt number is greater for ITP-nh as well. This is particularly visible in the centre of the interface and close to the widthwise walls. Since most of the SLP are developed above these regions, they eventually transport more heat which is represented by a higher value of $\langle Nu_c^{\mathscr{P}} \rangle_{S_{\mathscr{P}}}$ for ITP-nh.

Similar findings were noted by Basak et al. (2006) and Aswatha et al. (2011) who studied how the local temperature at the boundary influences the heat flux. They employed uniform and sinusoidal temperatures at the bottom plate and found that non-uniform heating, with a maximum in the centre of a plate, produces greater heat transfer rates in the centre of the plate than the uniform heating for $10^3 \leqslant Ra \leqslant 10^5$.

Table 9.2 further shows that the difference between $\langle Nu_c^{\mathscr{P}} \rangle_{S_{\mathscr{P}}}$ obtained for all non-isothermal BCs, i.e. ITP-nh, LCP and LCP-rad, is less than 0.8% for all considered Rayleigh numbers. Thus, small differences in the temperature variations at the interface lead to even smaller differences in the heat flux of the sheet-like plumes.

The contributions of the sheet-like plumes to the mean vertical heat flux are calculated from the area of the SLP $A^{\mathscr{P}}$, their Nusselt number $\langle Nu_c^{\mathscr{P}} \rangle_{S_{\mathscr{P}}}$ and the total Nusselt number evaluated at $z{=}0.5H/Nu_{c,eff}$. These contributions are listed in Table 9.2 for all considered Rayleigh numbers and BCs. Since the SLP account for 64% to 72% of the total Nusselt number depending on the Rayleigh number and BCs, they contain the dominating part of the mean vertical heat flux. The latter is in agreement with Shishkina and Wagner (2008), who studied the role of plumes in heat transport of a cylindrical Rayleigh–Bénard cell of aspect ratio one filled with water.

Nevertheless, if the BCs are non-isothermal, the SLP have less contribution to the mean vertical heat flux than in the case of isothermal BCs. In particular,

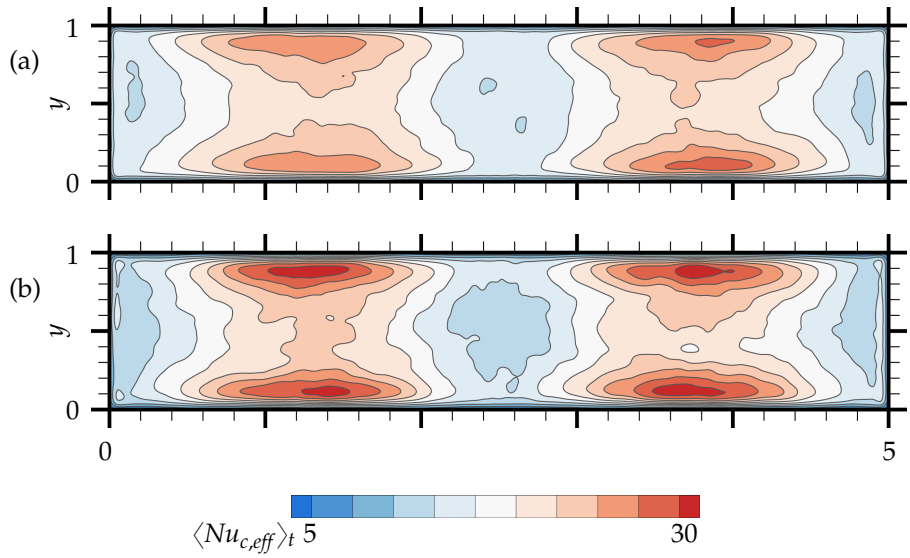

FIGURE 9.10: A horizontal cross-section showing a distribution of $\langle Nu_{c,eff} \rangle_t$ evaluated at $z = 0$ for $Ra_{eff} = 1.59 \times 10^7$ and ITP-nh (a), ITP (b).

in the case for $Ra_{eff} = 1.59 \times 10^7$ their contribution to the mean vertical heat flux is approximately 2% lower for ITP-nh than for ITP.

Furthermore, Table 9.2 shows that the contribution of the SLP to the mean vertical heat flux is not more than 65% for $Ra = 3.17 \times 10^5$ and it increases up to 72% for $Ra_{eff} = 1.59 \times 10^7$. On the other hand, the area of the SLP is not less than $A^{\mathscr{P}} = 2.59$ for $Ra = 3.17 \times 10^5$ and it decreases down to $A^{\mathscr{P}} = 2.19$ for $Ra_{eff} = 1.59 \times 10^7$. Thus, the sheet-like plumes are more energetic but occupy smaller area if the turbulence level grows.

9.2 Simplification of the irradiation calculations

In order to verify the hypothesis, postulated in Section 7.3.3 of Chapter 7, that the irradiation calculations based on the local temperature can be accurately approximated by the ones based on the area-averaged temperature, it is desired to analyse such temperature field which reflects the greatest temperature standard deviation at the interfaces. Thus, the instantaneous temperature field obtained for LCP ($\hat{\kappa}_s/\hat{\kappa}_f = 0.003$) and $Ra = 6.3 \times 10^7$, for which the standard deviation equals 6%, is selected. With this field, the irradiation $Nu_{b\to t}$ leaving the bottom interface and reaching the top one is calculated first by evaluating the second term of (7.5), i.e. $Nu_{b\to t} = Nr \sum_{S_j} \left(T_j + \Theta\right)^4 F_{ij}$. Then, a simplified calculation of $Nu_{b\to t}$ is performed based on the corresponding area-averaged temperature, i.e. $Nu_{b\to t} = Nr \left(\langle T \rangle_{S_{z=0}} + \Theta\right)^4 \sum_{S_j} F_{ij}$. In the first approach, $T_j = \langle T \rangle_{S_z} + T_j'$ and

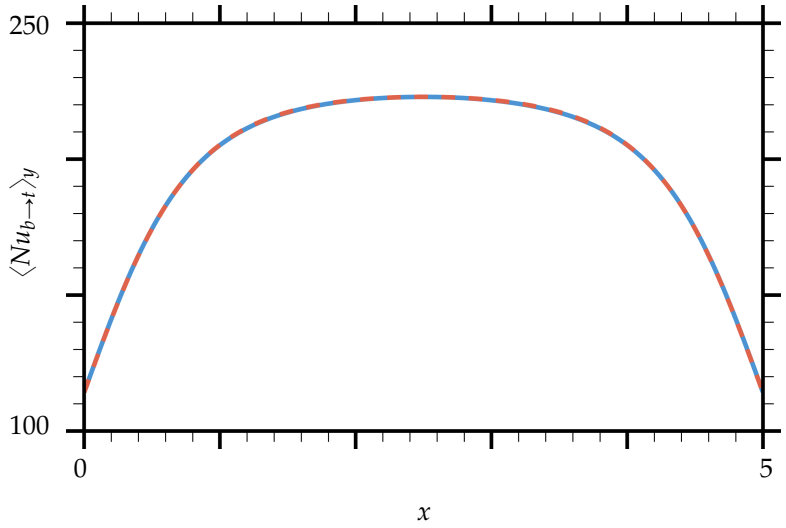

FIGURE 9.11: Profiles of line-averaged $Nu_{b\to t}$ in the presence of radiation for $Ra = 6.3 \times 10^7$ and $\hat{\kappa}_s/\hat{\kappa}_f = 0.003$, which are calculated based on the local (—) and area-averaged (- - -) temperature of the bottom interface.

is decomposed into its mean $\langle T\rangle_{S_z}$ and the fluctuating part $T_j^{'}$. Thus, it is clear that the only difference between the two approaches is the temperature spatial fluctuations $T_j^{'}$. Moreover, if these fluctuations are much smaller than $\langle T\rangle_{S_z} + \Theta$, the irradiations obtained from the two approaches must be similar. This indicates the potential for future simplification of the irradiation calculation. It is noteworthy that the number of operations needed to calculate $Nu_{b\to t}$ decreases by a factor of seven if the mean temperature field is used instead of the instantaneous one. Moreover, since calculating $Nu_{b\to t}$ is the computationally most expensive part of the radiation calculation, and consequently the calculation of the temperature at the interface (see (4.35)), the latter are significantly reduced.

In order to verify whether $\langle T\rangle_{S_z} + \Theta >> T_j^{'}$ and the aforementioned simplification is applicable, the widthwise-averaged profiles of $Nu_{b\to t}$, calculated by the two approaches, are plotted in Figure 9.11. Comparing these profiles reveals that they collapse at the interface. Moreover, $T_j^{'}$ is three orders of magnitude smaller than $\langle T\rangle_{S_z} + \Theta$. Thus, $\langle T\rangle_{S_z} + \Theta >> T_j^{'}$, and hence the temperature spatial variations of 6% are too small to alter the shape of $Nu_{b\to t}$.

9.3 The scaling of the global convective Nusselt number

Since, as discussed in Section 9.1.5, the sheet-like plumes transfer different amount of heat depending on the complexity level of the applied BCs and account for the dominating part of the mean vertical heat flux, it is of interest to know if the heating scenarios affect the scaling of the global convective Nusselt

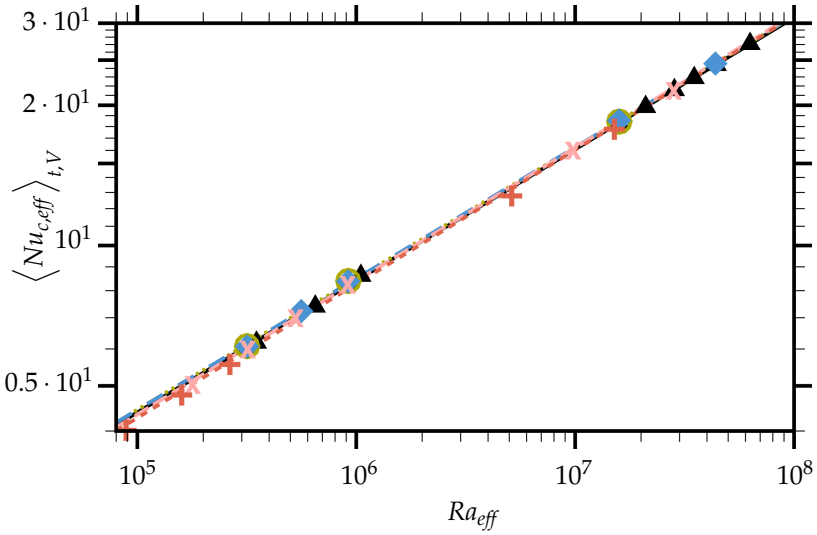

FIGURE 9.12: The time- and volume-averaged effective Nusselt number $\langle Nu_{c,eff} \rangle_{t,V}$ versus the effective Rayleigh number Ra_{eff} illustrated by a log-log plot for LCP-rad (Nr=0.0026, Θ=29), LCP-rad (Nr=0.0008, Θ=29), LCP, ITP-nh and ITP. The lines represent the fitting functions according to (9.9) for which the fitting errors are smaller than 0.9%, and the symbols indicate the corresponding data. Note that the uncertainty in the data due to statistical averaging is at most 0.02, and hence the resulting error bars lie within the data points.

number with the Rayleigh number. In fact, the boundary-related differences in the $Nu_c \sim Ra$ scaling has been already studied by e.g. Ahlers (2000); Roche et al. (2001); Verzicco (2004); Brown et al. (2005); Wittenberg (2010). Nevertheless, the previous studies have not addressed the herein considered heating scenarios.

In order to compare the present scaling with the ones from previous studies, all the quantities used to build the scaling are normalised as described in Section 2.3 of Chapter 2). The time- and volume-averaged effective convective Nusselt number $\langle Nu_{c,eff} \rangle_{t,V}$ is plotted in Figure 9.12 versus the effective Rayleigh number Ra_{eff} for all considered boundary conditions, i.e. ITP, ITP-nh, LCP and LCP-rad. Moreover, in the case of LCP-rad, the Nusselt number is obtained for $\Theta = 29$ and two radiation numbers, namely $Nr = 0.0008$ and $Nr = 0.0026$. It is clearly visible that for each heating scenario a power law

$$\langle Nu_{c,eff} \rangle_{t,V} = \mathscr{A} Ra_{eff}^{\mathscr{B}} \tag{9.9}$$

can represent the relation between the Nusselt and Rayleigh numbers. The prefactor $\mathscr{A}$ and the exponent $\mathscr{B}$ are obtained from the least squares fit to the data points, and they are listed in Table 9.3.

For all considered BCs, the scaling exponent $\mathscr{B}$ equals approximately 2/7, and the standard deviation of the exponent values obtained for all heating scenarios equals 0.0024. Moreover, $\mathscr{B}$ is around 1.5% greater for LCP-rad than for

	Nr	Θ	$\mathscr{A}$	$\mathscr{B}$
LCP-rad	0.0026	29	0.156	0.287
LCP-rad	0.0008	29	0.161	0.286
LCP	–	–	0.173	0.282
ITP-nh	–	–	0.174	0.281
ITP	–	–	0.170	0.282

TABLE 9.3: The least squares fitting parameters in $Nu_{c,eff} - Ra_{eff}$ scaling obtained for different heating scenarios.

ITP revealing that the scaling slope is only slightly affected when the complexity level of the BCs is reduced.

Furthermore, the standard deviation of the prefactor values obtained for all heating scenarios equals 0.007. Thus, $\mathscr{A}$ varies more, approximately by a factor of 3, than $\mathscr{B}$. However, since $\mathscr{B}$ is the exponent and $\mathscr{A}$ reflects the amplitude, both parameters have eventually similar contribution to the scaling especially in high Ra_{eff} regime.

It has been often argued that in some experiments the heating and cooling plates are closer to the constant temperature BC and in other experiments they are closer to the constant heat flux BC, which may explain the discrepancies between obtained scaling exponents in the $Nu_{c,eff} - Ra_{eff}$ scaling. For example, Chavanne et al. (2001) found the 2/7 exponent while Niemela et al. (2000) reported $\mathscr{B} = 0.309$ performing experiments in the same geometry and for the same medium. From the present results, it can be excluded that the differences in the heating scenarios may have such significant influence on the scaling exponent. Similar statement was recently noted by Stevens et al. (2011) who performed DNS in cylindrical RB cell up to $Ra = 2 \times 10^{12}$ for the constant heat flux and constant temperature BCs at the bottom plate.

Another conclusion can be drawn from the scaling parameters obtained in the presence of radiation. As shown in Table 9.3, the scaling exponent $\mathscr{B}$ is very close to 2/7 for both considered radiation numbers, which matches Grossmann and Lohse (2004) prediction of $Nu_{c,eff} \sim Ra_{eff}^{0.286}$ for fluids with $Pr \approx 1$. On the other hand, the prefactor $\mathscr{A}$ decreases by 3.1% with increasing the radiation number by a factor of 3.25. Thus, the prefactor $\mathscr{A}$ depends on radiation effects that modify the temperature distribution at the solid–fluid interface. It is noteworthy that recently Stevens et al. (2013) has shown the importance of the accurate determination of the prefactors of the Grossmann–Lohse theory. They noticed the significant improvement of the Nusselt number predictions after updating the prefactors that were originally developed in the early 21st century using scarce and often contradicting data due to insufficient understanding of

the physics.

10

CONCLUSIONS

The present research was set out to investigate the effects of radiation in the buoyancy driven flows with transient heating and cooling as well as to explore the consequences of employing simplified boundary conditions. For that purpose, I have implemented the horizontal solid plates of a finite thickness and conductivity as well as the surface-to-surface radiation model.

With this in mind, three-dimensional DNS of turbulent convection and surface-to-surface radiation were performed in a long cuboidal Rayleigh–Bénard cell equipped with solid horizontal plates of finite conductivity. Additionally, the simulations in the absence of radiation in the same RB cell with solid plates as well as with infinitely thin plates were performed and compared with these obtained in the presence of radiation.

The medium considered in this research was a dry air that is CO_2 free for which the Prandtl number equals 0.7. Furthermore, in order to study the dependencies of flow quantities on the Rayleigh number and the thermal diffusivity ratio, the simulations were conducted for Rayleigh numbers ranging from $Ra = 3.5 \times 10^5$ to $Ra = 6.3 \times 10^7$. Additionally, low and high thermal diffusivity ratios were considered. They are $\hat{\kappa}_s/\hat{\kappa}_f = 0.003$ and $\hat{\kappa}_s/\hat{\kappa}_f = 3.8$ which correspond to commonly used materials – Plexiglas (poss. Elastollan or Stimulite) and aluminium, respectively. Finally, the radiation was controlled by the radiation number, ranging from $Nr = 0.0008$ to $Nr = 0.0026$, and the temperature ratio, ranging from $\Theta = 29$ to $\Theta = 45$.

10.1 Findings

In the following, the main findings with regard to the research questions are synthesised.

How does the surface-to-surface radiation affect the bulk dynamics in the RB cell of aspect ratio five with conductive active walls and how do these changes depend on the thermal diffusivity ratio and the Rayleigh number?

The analysis of the LSC revealed that radiation has only a weak influence on the large-scale flow structures, since four convection rolls of similar shape appear in similar locations independently of the thermal diffusivity ratio. Nevertheless, it was observed that the smallest plumes are less pronounced in the presence of radiation.

Despite the similar flow structures, radiation renders the bulk more uniform when low conductivity plates are employed. This process takes place because the bulk is dominated by wider LSC driven by colder rising and warmer descending plumes in the presence of radiation than in its absence. Moreover, the plumes' temperatures are changed due to radiation-induced changes of the temperatures at the hot and cold horizontal walls. In other words, the increased homogeneity of the bulk is related to the temperature change at the interfaces of the conductive horizontal active walls. A similar increase was observed by Ridouane et al. (2004) who considered a square RB cell with isothermal horizontal active walls. However, they related this process to the temperature change at the adiabatic side walls.

Moreover, it was found that the homogeneity of the bulk, expressed in terms of $PDF_{V,T=0}$, grows linearly with the logarithm of the Rayleigh number, independently of the radiation scenario and the thermal diffusivity ratio. Proposed fitting functions for $\hat{\kappa}_s/\hat{\kappa}_f = 0.003$ show that the increase in the bulk homogeneity with increasing Rayleigh numbers is 52% stronger in the presence of radiation than in its absence.

On the other hand, the influence of radiation on the bulk homogeneity is significantly weaker for high thermal diffusivity ratios. This is directly related to the influence of the radiation on the temperatures at the interfaces, which also decreases with increasing $\hat{\kappa}_s/\hat{\kappa}_f$.

Furthermore, the analysis of the turbulence intensities in the bulk for $\kappa_s/\hat{\kappa}_f = 0.003$ reveals that thermal radiation damps the temperature and velocity fluctuations in the entire convection cell. Nevertheless, the greatest decrease is observed in the locations of their maxima and for the lowest *Ra*. In contrast, the turbulent fluctuations evaluated in the bulk for $\kappa_s/\hat{\kappa}_f = 3.8$ are not affected by radiation for any considered *Ra*.

How do the radiation-induced changes of the interface conditions affect the thermal plumes in the cuboidal RB cell with conductive active walls and how do these interface condition modifications depend on the thermal diffusivity ratio and the Rayleigh number?

The influence of radiation on the temperature of the heat sources and hence thermal plumes was investigated by analysing the footprints of the LSC left on the solid–fluid interfaces. It was found that the temperatures at the interfaces are not uniformly affected by radiation. This is particularly visible at the hot interface. It was shown that this irregular behaviour is related to the thermal plumes, of which the cold ones are equally altered by radiation, while the hot ones are with different strengths, depending on their location: there is a stronger influence in the centre than close to the widthwise side walls. This is true for any Rayleigh number and thermal diffusivity ratio.

It was also shown that radiation breaks the symmetry between the homogeneity of the temperature distribution at the top and bottom interfaces, mainly due to large spatial variations of the temperatures $T > \langle T \rangle_{S_{z=0}}$ at the bottom interface. The latter was interpreted as there are less homogeneous hot plumes generated at the bottom interface compared to the cold plumes generated at the top interface.

Furthermore, it was found that radiation damps the temporal and spatial fluctuations of the temperature distribution whenever the plates have low conductivity. Moreover, these fluctuations further decrease with decreasing Rayleigh number. On the other hand, if the plates are highly conductive, radiation does not affect the temporal fluctuations but it emphasises the spatial ones. Nevertheless, this increase is negligibly small and the fluctuations of the temperature distributions at the interfaces are still of the order of 10^{-5} for any considered Rayleigh number.

How do the convective and radiative heat fluxes contribute to the total heat transfer with respect to the changes of the thermal diffusivity ratio and the Rayleigh number?

From the definition, the total heat transferred through the RB cell with the solid plates is the conductive heat flux evaluated at the outer side of the solid plates, where the temperature is fixed. This heat is further split into the convective and radiative parts evaluated at the fluid side of the interfaces.

It was shown that the total heat transfer in the presence of radiation is greater than the one in the absence of radiation for any thermal diffusivity ratio and the Rayleigh number. As discussed, the responsibility for that lies with the radiative heat flux for which extra heat is supplied through the solid plates.

However, the absolute value of the total heat transfer, expressed in terms of the global Nusselt number, changes with the thermal diffusivity ratio and the Rayleigh number, and the contribution of convective and radiative Nusselt numbers changes accordingly. When the high conductivity plates are replaced by the low conductivity ones, the convective and especially radiative Nusselt numbers decrease as a consequence of the temperature changes at the interfaces.

Furthermore, when the Rayleigh number increases and the other control parameters are constant, the contribution of the convective heat flux increases, and simultaneously the contribution of the radiative heat flux decreases. It was shown that the latter is due to the decrease of $\langle Nu_r \rangle_{t,S_z}$ which is over-compensated by the increase of $\langle Nu_c \rangle_{t,S_z}$, thanks to the specific change of the dimensional parameters.

What are the mechanisms of the convective drop in the RB cell with low conductivity active walls and how does this drop vary in space?

The evaluation of the convective Nusselt number at the interfaces revealed that radiation locally decreases $\langle Nu_c \rangle_t$. That was referred to as the local convective drop. One major result of this research is that the convective drop is smaller in regions where plumes detach than in those where plumes impinge on the interfaces.

Moreover, it was shown that this occurs due to a combination of two mechanisms. In regions where plumes emerge, only the radiative heat flux and its intensity is responsible for the local convective drop, while in regions where plumes arrive, the convective heat transported by the arriving plumes also contributes.

Although the convective drop has been already reported (Akiyama and Chong 1997; Balaji and Venkateshan 1993; Gad and Balaji 2010; Ridouane et al. 2004), other research address no more than the role of the radiative heat flux in the mean convective drop. Therefore, the present study advances our understanding of this phenomenon.

Furthermore, thanks to the spatial variations of the convective drop, the vertical temperature gradient at the interfaces better resembles the constant heat flux boundary conditions in the presence of radiation than in its absence.

What is the correlation between the convective and radiative Nusselt number in time and space in the considered RB enclosure with low and high conductivity plates?

Analysing the correlation coefficients of the time series of Nu_c and Nu_r reveals that convective and radiative Nusselt numbers are strongly anti-correlated in time. The correlation is slightly stronger for plates of low conductivity than for those with high conductivity. Furthermore, it was shown that the anti-correlation is obtained because these processes take place on similar time scales.

Moreover, analysing the spatial correlation of Nu_c and Nu_r reveals that although these processes are anti-correlated for $\hat{\kappa}_s/\hat{\kappa}_f = 0.003$, the correlation in space is a lot weaker for $\hat{\kappa}_s/\hat{\kappa}_f = 3.8$. This indicates that a spatially varying convective heat flux is accompanied by more variations of the radiative heat flux for the lower thermal diffusivity ratio. This is due to the fact that the

distribution of Nu_r depends on the temperature at the interface, which also varies more for the lower thermal diffusivity ratio.

How does the distribution of the radiative Nusselt number depend on the thermal diffusivity ratio?

At first the dependency was analysed qualitatively by making use of 2D distributions of the radiative Nusselt number evaluated for low and high thermal diffusivity ratio for $Ra = 6.3 \times 10^7$. These visualisations revealed that the shape of the Nu_r distribution changes from the elliptical-like to the non-elliptical when the thermal diffusivity ratio is decreased from $\hat{\kappa}_s/\hat{\kappa}_f = 3.8$ to $\hat{\kappa}_s/\hat{\kappa}_f = 0.003$.

The reason for the above was found by analysing the dependency of the Nu_r components on the thermal diffusivity ratio. With this in mind, it was shown that the irradiation originating from the ambient environment which passes through the side walls depends exclusively on the ambient temperature and the control parameters for radiation, which in turn do not vary with $\hat{\kappa}_s/\hat{\kappa}_f$.

With regard to another Nu_r component - the irradiation originating from the opposite interface - two factors, which might determine $Nu_{t\to b}$ and $Nu_{b\to t}$, were identified and inspected. The first factor arises from the fact that the temperature distributions at the interfaces are less homogeneous for $\hat{\kappa}_s/\hat{\kappa}_f = 0.003$ than for $\hat{\kappa}_s/\hat{\kappa}_f = 3.8$. Nevertheless, it was shown that the non-homogeneity of the temperature distribution does not affect the distribution of $Nu_{t\to b}$ and $Nu_{b\to t}$ and hence neither that of Nu_r. The second factor arises from the fact that the magnitude of the absolute temperature at the interfaces is smaller for $\hat{\kappa}_s/\hat{\kappa}_f = 0.003$ than for $\hat{\kappa}_s/\hat{\kappa}_f = 3.8$. However, the mean temperature determines only the maximum and the gradation of the elliptical-like distribution of $Nu_{t\to b}$ and $Nu_{b\to t}$ and therefore does not influence the shape of Nu_r.

The analysis of the remaining radiative Nusselt number contributor revealed that the distribution of the emissive Nusselt number is non-elliptical for low as well as for high thermal diffusivity ratio. However, when $Ra = 6.3 \times 10^7$ and $\hat{\kappa}_s/\hat{\kappa}_f = 3.8$, the spatial standard deviation of the emissive Nusselt number is three orders of magnitude smaller than that of the irradiative Nusselt number while these deviations are of similar order for $\hat{\kappa}_s/\hat{\kappa}_f = 0.003$. Thus, for high thermal diffusivity ratio, the shape of the radiative Nusselt number is mainly determined by the irradiative Nusselt number, while for low thermal diffusivity ratio both emissive and irradiative Nusselt numbers play equal role.

How do the control parameters for radiation and the Rayleigh number affect the radiative and convective Nusselt numbers as well as the effective Rayleigh number in the RB cell with low conductivity active walls?

The radiation effects were parameterised by the dimensionless radiation number Nr and the temperature ratio Θ. These control parameters determine

the strength of the radiation, and hence the radiative Nusselt number increases if Nr or Θ increase. On the other hand, the convective Nusselt number and the effective temperature difference decrease when any of the control parameters for radiation increase.

Furthermore, it was shown that whenever the convective Nusselt number drops due to a decrease in the Rayleigh number, the radiative Nusselt number and the effective Rayleigh number increase.

Finally, in order to scale the above relations a fitting function was proposed. The slopes of these fitting functions quantitatively illustrate that the change of Nu_r, Nu_c or ΔT_{eff} is more sensitive to a change in the radiation number than to a change in the temperature ratio.

How do the coherent structures and the global heat transfer change with reducing the complexity level of the thermal boundary conditions?

The analysis of the sheet-like plumes and the time- and volume-averaged effective Nusselt number was performed for four types of boundary conditions, which were employed in the cuboidal RB cell. The most complex BCs were modelled by the low conductivity solid plates which account for the exchange of thermal radiation. The first reduction of the complexity level was done by excluding the existence of radiation. Further reduction was to trim a finite thickness of the solid plates leading to a fixed temperature distribution prescribed on the infinitely thin plates. Finally, the most simplified BCs were a constant temperature BCs which do not allow any variations in time nor in space.

It was noticed that the reduction of the complexity level eventually affects the spatial and temporal variations of the interface temperature. Thus, the postulated research question was boiled down to the question about the dependency of the thermal plumes and the global Nu_{eff} on the spatial non-homogeneity and temporal fluctuations of the temperature distribution at the interface.

The conditionally averaged thermal dissipation rate was used to extract the thermal plumes from the turbulent background at the border between the thermal boundary layer and the bulk, i.e. at $z{=}0.5H/Nu_{c,eff}$.

It was shown that the mean temperature, above which the plumes development starts in a statistical sense, is barely sensitive to the variations of the spatial non-homogeneity and temporal instability of the interface temperature. Nevertheless, when the spatial temperature distribution at the interface is replaced by its simplified isothermal representation, the predicted sheet-like plumes are colder and larger. This decrease of the SLP' temperature is evident due to underproduction of SLP_{III} (i.e. the warmest plumes) and overproduction of SLP_{II} (moderately warm plumes; see Figure 9.4) when plates are isothermal.

Moreover, the underproduction of the warmest plumes takes place in the centre and close to the lateral walls at the horizontal plane S_z, $z{=}0.5H/Nu_{c,eff}$. It

was also found that this local phenomenon is related to the temperature distribution at the nearby interface. In other words, the local production of the warmest SLP at z=0.5$H/Nu_{c,\mathit{eff}}$ is lower for isothermal BC than for non-isothermal ones because the local temperatures at the corresponding locations at the interface are lower.

Similar local phenomenon was found when the most complex BCs, i.e. LCP-rad, were simplified by excluding heat radiation, i.e. LCP. This simplification leads to the underproduction of SLP_{III} close to the lateral walls and overproduction of SLP_{III} in the centre since the local temperatures at the corresponding locations at the interface are respectively lower and higher. Therefore, the production of SLP_{III} strongly depends on the shape of the temperature distribution at the interface.

Furthermore, it was shown that the temporal fluctuations of the interface temperature have a weak influence on the mean temperature of SLP and no effect on the non-homogeneity of SLP' temperature in the considered Ra range. However, the fluctuations at the interface were at most 0.002 (LCP, $Ra = 6.3 \times 10^7$), which could be responsible for such small or even negligibly effects.

Applying the most simplified BC, i.e. the isothermal BC, leads to underprediction of the mean sheet-like plumes' temperature fluctuations, which is mainly caused by overproduction of SLP_I and SLP_{II}.

On the other hand, applying less drastic simplifications, i.e. ITP-nh and LCP, does not visibly affect $\langle T^{\mathscr{P}}_{rms} \rangle_{S_{\mathscr{P}}}$ even though it causes a decrease of the maximal temperature fluctuations of SLP_{III}. The latter is however only a local event caused by a decrease of the local temperatures in the regions where SLP_{III} are likely created. Moreover, not all the temperature fluctuations at the interface are related to plumes, which was also suggested by Verzicco and Sreenivasan (2008).

The evaluation of the SLP' Nusselt number for $Ra = 3.17 \times 10^5$ unveiled that replacing the non-homogeneous temperature distribution at the interface with its isothermal representation causes the underestimation of Nu up to 2.3%. However, this factor decreases with increasing the Rayleigh number and reaches 1.1% for $Ra = 1.59 \times 10^7$. It was shown that such underprediction of $\langle Nu^{\mathscr{P}}_c \rangle_{S_{\mathscr{P}}}$ is related to the locally lower temperatures at the interface, especially in the regions where the SLP are most often created. Furthermore, since the temperature distributions at the interfaces for LCP-rad and LCP differ even less, $\langle Nu^{\mathscr{P}}_c \rangle_{S_{\mathscr{P}}}$ is overestimated less than 0.8% for all considered Rayleigh numbers in the absence of radiation.

It was pinpointed that the SLP contain the dominating part of the mean vertical heat flux for all considered Rayleigh numbers and BCs, which is in agreement with Shishkina and Wagner (2008). In addition, the sheet-like plumes are more energetic but occupy smaller area if the turbulence level grows. Nevertheless, if

the BCs are isothermal, the SLP contribute more to the mean vertical heat flux than in the case of non-isothermal BCs. In particular, for $Ra_{eff} = 1.59 \times 10^7$ their contribution to the mean vertical heat flux is approximately 2% greater for ITP than for ITP-nh.

When it comes to the global heat transfer, a power law $\langle Nu_{c,eff} \rangle_{t,V} = \mathscr{A} Ra_{eff}^{\mathscr{B}}$ was used to represent the relation between the Nusselt and Rayleigh numbers. For all considered BCs, the scaling exponent $\mathscr{B}$ equals approximately 2/7, which matches Grossmann and Lohse (2004) prediction of $Nu_{c,eff} \sim Ra_{eff}^{0.286}$ for fluids with $Pr \approx 1$. However, it is around 1.5% underestimated when the complexity level of the BCs is reduced from LCP-rad to ITP. On the other hand, when radiation is present, the scaling exponent $\mathscr{B}$ is very close to 2/7 for both considered radiation numbers, i.e. $Nr = 0.0008$ and $Nr = 0.0026$, but the prefactor $\mathscr{A}$ decreases by 3.1% with increasing the radiation number. The latter reveals that the prefactor $\mathscr{A}$ depends on radiation effects that modify the temperature distribution at the solid–fluid interface.

From the presented results, it could be excluded that employing various heating and cooling systems in the experimental setup, may be responsible for significant discrepancies in the scaling exponent that were observed by experimentalists working with the same geometry and medium. This finding is in agreement with Stevens et al. (2011).

How can the irradiation calculations be simplified?

The analysis of the irradiation originating from the interface and the one that passes through the side walls gave rise to the hypothesis that the irradiation calculations based on the local temperature could be accurately approximated by the ones based on the area-averaged temperature. It was shown that these two approaches result in similar values of the irradiation if the spatial fluctuations of the interface temperature are at least three orders of magnitude smaller than $\langle T \rangle_{S_z} + \Theta$.

Furthermore, this simplification decreases the number of operations, needed to calculate $Nu_{t \to b}$ and $Nu_{b \to t}$, by a factor of seven, and hence significantly reduces the computational time needed for the entire radiation calculation and eventually the temperature at the interface.

10.2 Theoretical implications

In this section, I attempt to briefly argue how my findings could contribute to the general knowledge in the subject.

This study is particularly interesting for anyone concerned how the horizon-

tal plates of a finite thickness affect the heat and fluid flow in the presence and absence of surface-to-surface radiation, and how they can be simplified.

When fluid is bounded by perfectly conductive plates ($\kappa_s = \infty$) or at least by highly conductive plates, i.e. $\hat{k}_s/\hat{k}_f \geqslant 9480$, e.g. air bounded by aluminium or copper plates, and sufficiently low plates' thickness, i.e. $h_s \leqslant 0.065H$, the temperatures at the interfaces coincide with these at the outer side of the plates. Therefore, the implementation complexity and the computational cost can be easily decreased by employing infinitely thin plates (ITP) instead of highly conductive plates (HCP). For such a case, the first and second order quantities are predicted with the same accuracy as when HCP are employed. This certainly holds true in the absence of radiation, but also in the presence of radiation if the radiation control parameters are sufficiently small. To be on the safe side, $Nr \leqslant 0.0008$ and $\Theta \leqslant 29$.

On the other hand, when fluid is bounded by low conductivity plates, i.e. $\hat{k}_s/\hat{k}_f \leqslant 7.6$, e.g. air bounded by Plexiglas, Elastollan or Stimulite, and sufficiently high plates' thickness, i.e. $h_s \geqslant 0.065H$, a certain temperature distributions are developed at the interfaces. These distributions considerably differ from the constant temperature fixed at the outer side of the plates. Thus, if the flow quantities have to be predicted with the DNS accuracy or the analysis of the plume dynamics is of interest, it is important to employ the low conductivity plates and incorporate the radiative heat transfer. The latter is particularly important for very high Rayleigh numbers, e.g. about the ultimate regime, since the non-homogeneity of the temperature distribution at the interface increases with Ra.

Considering CFD applications except the thermal comfort problems, it seems to be sufficient to employ infinitely thin plates with constant temperature (ITP) instead of low conductivity plates. However, since the temperature distributions developed at the interfaces determine $\Delta T_{eff} < \Delta T$, the boundary temperatures have to be normalized with ΔT_{eff}. Moreover, although this simplification seems to be reasonable in the range of radiation parameters considered in this study, it might produce unacceptably imprecise predictions for very high values of Nr and Θ or if the expected level of non-homogeneity of the temperature distribution at the interfaces is very high. In such cases, it is desired to fix at least the infinitely thin plates with the effective temperature distribution which varies in space (ITP-nh).

Last but not least, this study may be used as a reference for studies concerning simplifications of radiation calculations, such as grid coarsening, or approximation and statistical methods, e.g. the P-1 approximation, the discrete ordinates method or the Monte Carlo method.

10.3 Limitations of the study and open questions

Besides answering the questions posed in Section 1.5.2 of Chapter 1, there are many more that can be asked. Some of them originate from the limitations of this study.

Assuming the heating and cooling plates to emit and absorb radiation as a blackbody allows to investigate only the maximal effects of radiation. On the other hand, performing simulations in the absence of radiation allows to study only the minimal effects of radiation. Thus, conducting further studies in this subject, it might be of interest to perform simulations for some intermediate radiative properties and analyse scaling relations. It would be however necessary to implement modifications to the numerical code, which noticeably increase the computational time.

Technically speaking, it is hardly possible to maintain a constant temperature outside the RB cell with transparent side walls, i.e. in the entire laboratory room. However, if the ambient temperature T_{out} is lower than the bulk temperature T_0, the energy transferred from the ambient environment to the cell is lower than the energy leaving the cell through the transparent side walls. And vice versa, if $T_{out} > T_0$, the cell gains energy. These scenarios break the energy conservation in the RB cell. Therefore, it would be interesting to investigate how the variations of the ambient temperature affect the convective heat transport and the flow symmetry through the incoming and outcoming radiation. This is particularly interesting if the RB cell is equipped with low conductivity plates.

Since the simplified BCs only slightly alter the plumes for $Ra \lesssim 10^8$, for which the temperature fluctuations at the interfaces are small, it would be interesting to examine how the coherent structures change for a very high Ra, e.g. about the ultimate regime, for which these variations are much stronger.

Another issue is related to the technical aspects. Since experimentalists use different systems to cool and heat the fluid contained in the RB cell, e.g. water heating and air cooling, the thermal conductivity and the size of the entire heating and cooling systems eventually differ from each other. Thus, it would be interesting to know how the differences between the plates' thickness and thermal conductivities affect the plume development, heat transfer and the flow symmetry.

As with any investigative study, answering one question might lead to new ones. This opens the whole zoo of queries and leaves space for a follow-up research activity.

APPENDIX A. SIMULATION PARAMETERS

Ra $[-]$	Pr $[-]$	Nr $[-]$	Θ $[-]$	$\hat{T}_0$ $[C]$	$\hat{\Delta T}$ $[C]$	$\hat{H}$ $[m]$	plates
3.5×10^5	0.7	0.0008	29	198	16.0	0.12	LCP, HCP
6.3×10^5	0.7	0.0008	29	170	15.4	0.14	LCP, HCP
1.1×10^6	0.7	0.0008	29	149	14.7	0.15	LCP, HCP
2.1×10^7	0.7	0.0008	29	40	10.9	0.29	LCP, HCP
6.3×10^7	0.7	0.0008	29	8	9.8	0.37	LCP, HCP

TABLE A1: Dimensionless and dimensional control parameters used in the simulations with solid plates for which results are presented in Chapters 5–7.

Ra [−]	Pr [−]	Nr [−]	Θ [−]	$\hat{T}_0$ [C]	$\Delta\hat{T}$ [C]	$\hat{H}$ [m]	plates
		0.0008	45	400	15.0	0.21	LCP
		0.0008	41	354	15.2	0.19	LCP
		0.0008	37	301	15.6	0.16	LCP
		0.0008	33	249	16.0	0.14	LCP
3.5×10^5	0.7	0.0008	29	198	16.0	0.12	LCP
		0.0012	29	258	18.5	0.14	LCP
		0.0016	29	310	20.3	0.15	LCP
		0.0021	29	361	22.1	0.17	LCP
		0.0026	29	400	23.4	0.18	LCP
		0.0008	45	360	14.1	0.24	LCP
6.3×10^5	0.7	0.0008	29	170	15.4	0.14	LCP
		0.0026	29	360	22.0	0.21	LCP
		0.0008	45	330	13.4	0.27	LCP
		0.0008	41	289	13.7	0.24	LCP
		0.0008	37	242	14.0	0.21	LCP
		0.0008	33	195	14.3	0.18	LCP
1.1×10^6	0.7	0.0008	29	149	14.7	0.15	LCP
		0.0012	29	203	16.6	0.18	LCP
		0.0016	29	250	18.2	0.20	LCP
		0.0021	29	296	19.8	0.22	LCP
		0.0026	29	330	21.0	0.23	LCP
		0.0008	45	175	10.0	0.52	LCP
2.1×10^7	0.7	0.0008	29	40	10.9	0.29	LCP
		0.0026	29	175	15.6	0.45	LCP
		0.0008	45	128	8.9	0.66	LCP
		0.0008	41	101	9.1	0.59	LCP
		0.0008	37	70	9.3	0.51	LCP
		0.0008	33	39	9.5	0.44	LCP
6.3×10^7	0.7	0.0008	29	8	9.8	0.37	LCP
		0.0012	29	44	11.0	0.43	LCP
		0.0016	29	75	12.1	0.48	LCP
		0.0021	29	105	13.2	0.53	LCP
		0.0026	29	128	14.0	0.57	LCP

TABLE A2: Dimensionless and dimensional control parameters used in the simulations with solid plates for which results are presented in Chapter 8.

Bibliography

Ahlers, G., 2000. Effect of sidewall conductance on heat-transport measurements for turbulent Rayleigh–Bénard convection. Physical Review E 63 (1), 015303.

Ahlers, G., 2009. Trend: turbulent convection. Physics 2, 74.

Ahlers, G., Grossmann, S., Lohse, D., 2009. Heat transfer and large scale dynamics in turbulent Rayleigh–Bénard convection. Reviews of Modern Physics 81 (2), 503.

Akiyama, M., Chong, Q., 1997. Numerical analysis of natural convection with surface radiation in a square enclosure. Numerical Heat Transfer, Part A: Applications 32 (4), 419–433.

Antohe, B., Lage, J., 1996a. Amplitude effect on convection induced by time-periodic horizontal heating. International Journal of Heat and Mass Transfer 39 (6), 1121–1133.

Antohe, B., Lage, J., 1996b. Experimental investigation on pulsating horizontal heating of a water-filled enclosure. Journal of Heat Transfer 118 (4), 889–896.

Archimedes of Syracuse, about 250 BCE. On Floating Bodies.

Aswatha, C., Gangadhara, G., Sridhara, S., Seetharamu, K., 2011. Effect of different thermal boundary conditions at bottom wall on natural convection in cavities. Journal of Engineering Science and Technology 6 (1), 109–130.

Atofina Chemicals, Inc., 2000. Atoglas PLEXIGLAS®Acrylic Sheet, General information and physical properties. Taylor & Francis.

Balaji, C., Venkateshan, S., 1993. Interaction of surface radiation with free convection in a square cavity. International Journal of Heat and Fluid Flow 14 (3), 260–267.

Basak, T., Roy, S., Balakrishnan, A., 2006. Effects of thermal boundary conditions on natural convection flows within a square cavity. International Journal of Heat and Mass Transfer 49 (23), 4525–4535.

BASF SE, 2011. Thermoplastic Polyurethane Elastomers, technical information. URL `www.polyurethanes.basf.de/pu/Elastollan`

BASF SE, 2013. Elastollan®, Stimulite®, product information. URL `www.aerospace.basf.com/seating-components`

Batchelor, G., et al., 1959. Small-scale variation of convected quantities like temperature in turbulent fluid. Journal of Fluid Mechanics 5 (1), 113–133.

Belmonte, A., Libchaber, A., 1996. Thermal signature of plumes in turbulent convection: The skewness of the derivative. Physical Review E 53 (5), 4893.

Belmonte, A., Tilgner, A., Libchaber, A., 1994. Temperature and velocity boundary layers in turbulent convection. Physical Review E 50 (1), 269.

Bérnard, H., 1900. Les tourbillons cellulaires dans une nappe liquide [the cellular vortices in a liquid layer]. Rev Gén Sci Pure Appl 11, 1261–1271.

Blasius, H., 1908. Grenzschichten in Flüssigkeiten mit kleiner Reibung. Z. Math. Phys. 56, 1–37.

Boltzmann, L., 1884. Ableitung des Stefan'schen Gesetzes betreffend die Abhängigkeit der Wärmestrahlung von der Temperatur aus der electromagnetischen Lichttheorie. Annalen der Physik und Chemie 22, 291–294.

Brown, E., Nikolaenko, A., Funfschilling, D., Ahlers, G., 2005. Heat transport in turbulent Rayleigh–Bénard convection: Effect of finite top- and bottom-plate conductivities. Physics of Fluids 17, 075108.

Castaing, B., Gunaratne, G., Heslot, F., Kadanoff, L., Libchaber, A., Thomae, S., Wu, X.-Z., Zaleski, S., Zanetti, G., 1989. Scaling of hard thermal turbulence in Rayleigh–Bénard convection. Journal of Fluid Mechanics 204, 1–30.

Cattaneo, F., Emonet, T., Weiss, N., 2003. On the interaction between convection and magnetic fields. The Astrophysical Journal 588 (2), 1183.

Chavanne, X., Chilla, F., Chabaud, B., Castaing, B., Hebral, B., 2001. Turbulent Rayleigh–Bénard convection in gaseous and liquid He. Physics of Fluids 13 (5), 1300–1320.

Chillá, F., Ciliberto, S., Innocenti, C., Pampaloni, E., 1993. Boundary layer and scaling properties in turbulent thermal convection. Il Nuovo Cimento D 15 (9), 1229–1249.

Chillà, F., Rastello, M., Chaumat, S., Castaing, B., 2004. Ultimate regime in Rayleigh–Bénard convection: The role of plates. Physics of Fluids 16 (7), 2452–2456.

Ching, E. S., Guo, H., Shang, X.-D., Tong, P., Xia, K.-Q., 2004. Extraction of plumes in turbulent thermal convection. Physical Review Letters 93 (12), 124501.

Chorin, A. J., 1968. Numerical solution of the Navier–Stokes equations. Mathematics of Computation 22 (104), 745–762.

Cioni, S., Ciliberto, S., Sommeria, J., 1997. Strongly turbulent Rayleigh–Bénard convection in mercury: Comparison with results at moderate Prandtl number. Journal of Fluid Mechanics 335, 111–140.

Clark, R. A., Ferziger, J. H., Reynolds, W., 1979. Evaluation of subgrid-scale models using an accurately simulated turbulent flow. Journal of Fluid Mechanics 91 (1), 1–16.

Collins, G. W., 1989. The fundamentals of stellar astrophysics. New York, WH Freeman and Co.

Colomer, G., Costa, M., Consul, R., Oliva, A., 2004. Three-dimensional numerical simulation of convection and radiation in a differentially heated cavity using the discrete ordinates method. International Journal of Heat and Mass Transfer 47 (2), 257–269.

Czarnota, T., Wagner, C., 2011a. Direct numerical simulations of the turbulent convection and thermal radiation in a Rayleigh–Bénard cell. In: Proceedings of the 7th International Symposium On Turbulence and Shear Flow Phenomena.

Czarnota, T., Wagner, C., 2011b. Turbulent convection in a Rayleigh–Bénard cell with solid horizontal plates of finite conductivity. In: Kürten, H., Geurts, B., Armenio, V., Fröhlich, J. (Eds.), Direct and Large Eddy Simulation VIII. Vol. 15. Springer, pp. 371–376.

Czarnota, T., Wagner, C., 2013. Turbulent convection in a Rayleigh–Bénard cell with solid horizontal plates of finite conductivity. In: New Results in Numerical and Experimental Fluid Mechanics VIII. Springer, pp. 607–614.

Czarnota, T., Wagner, C., 2014. Direct numerical simulations of turbulent convection and thermal radiation in a Rayleigh–Bénard cell with solid plates. In: Deville, M. O., Estivalezes, J.-L., Gleize, V., Lê, T.-H., Terracol, M., Vincent, S. (Eds.), Turbulence and Interactions. Vol. 125 of Notes on Numerical Fluid Mechanics and Multidisciplinary Design. Springer, pp. 39–46.

Daya, Z., Ecke, R., 2001. Does turbulent convection feel the shape of the container? Physical Review Letters 87 (18), 184501.

Daya, Z., Ecke, R., 2002. Prandtl number dependence of interior temperature and velocity fluctuations in turbulent convection. Physical Review E 66 (4), 045301.

Deardorff, J., 1973. The use of subgrid transport equations in a three-dimensional model of atmospheric turbulence. Journal of Fluids Engineering 95 (3), 429–438.

Du Puits, R., RESAGK, C., Tilgner, A., Busse, F., Thess, A., 2007. Structure of thermal boundary layers in turbulent Rayleigh–Bénard convection. Journal of Fluid Mechanics 572, 231–254.

Ebert, A., Resagk, C., Thess, A., 2008. Experimental study of temperature distribution and local heat flux for turbulent Rayleigh–Bénard convection of air in a long rectangular enclosure. International Journal of Heat and Mass Transfer 51 (17), 4238–4248.

Emran, M., Schumacher, J., 2008. Fine-scale statistics of temperature and its derivatives in convective turbulence. Journal of Fluid Mechanics 611, 13–34.

Feldmann, D., Wagner, C., 2012. Direct numerical simulation of fully developed turbulent and oscillatory pipe flows at $Re_\tau = 1440$. Journal of Turbulence 13 (32), 1–28.

Fitzjarrald, D. E., 1976. An experimental study of turbulent convection in air. Journal of Fluid Mechanics 73 (04), 693–719.

Freund, G., Pesch, W., Zimmermann, W., 2011. Rayleigh–Bénard convection in the presence of spatial temperature modulations. Journal of Fluid Mechanics 673, 318–348.

Gad, M. A., Balaji, C., 2010. Effect of surface radiation on RBC in cavities heated from below. International Communications in Heat and Mass Transfer 37 (10), 1459–1464.

Gauthier, F., Roche, P.-E., 2008. Evidence of a boundary layer instability at very high Rayleigh number. Europhysics Letters 83 (2), 24005.

Gille, J., Goody, R., 1964. Convection in a radiating gas. Journal of Fluid Mechanics 20 (01), 47–79.

Gray, D. D., Giorgini, A., 1976. The validity of the Boussinesq approximation for liquids and gases. International Journal of Heat and Mass Transfer 19 (5), 545–551.

Grossmann, S., Lohse, D., 2000. Scaling in thermal convection: A unifying theory. Journal of Fluid Mechanics 407, 27–56.

Grossmann, S., Lohse, D., 2001. Thermal convection for large Prandtl numbers. Physical Review Letters 86 (15), 3316.

Grossmann, S., Lohse, D., 2002. Prandtl and Rayleigh number dependence of the Reynolds number in turbulent thermal convection. Physical Review E 66 (1), 016305.

Grossmann, S., Lohse, D., 2003. On geometry effects in Rayleigh–Bénard convection. Journal of Fluid Mechanics 486, 105–114.

Grossmann, S., Lohse, D., 2004. Fluctuations in turbulent Rayleigh–Bénard convection: The role of plumes. Physics of Fluids 16 (12), 4462–4472.

Grötzbach, G., 1983. Spatial resolution requirements for direct numerical simulation of the Rayleigh–Bénard convection. Journal of Computational Physics 49 (2), 241–264.

Hartmann, D. L., Moy, L. A., Fu, Q., 2001. Tropical convection and the energy balance at the top of the atmosphere. Journal of Climate 14 (24), 4495–4511.

Hertz, H., 1887. Ueber sehr schnelle electrische schwingungen. Annalen der Physik 267 (7), 421–448.

Horn, S., 2015. Rotation and non-Oberbeck–Boussinesq effects in turbulent Rayleigh–Bénard convection. Ph.D. thesis.

Horn, S., Shishkina, O., Wagner, C., 2013. On non-Oberbeck–Boussinesq effects in three-dimensional Rayleigh–Bénard convection in glycerol. Journal of Fluid Mechanics 724, 175–202.

Huizenga, C., Zhang, H., Mattelaer, P., Yu, T., Arens, E. A., Lyons, P., 2006. Window performance for human thermal comfort. In: Final report to the National Fenestration Rating Council.

Hunt, J., Vrieling, A., Nieuwstadt, F., Fernando, H., 2003. The influence of the thermal diffusivity of the lower boundary on eddy motion in convection. Journal of Fluid Mechanics 491, 183–205.

Hutchison, J., Richards, R., 1999. Effect of nongray gas radiation on thermal stability in carbon dioxide. Journal of Thermophysics and Heat Transfer 13 (1), 25–32.

Hyun, J. M., 1994. Unsteady buoyant convection in an enclosure. Advances in Heat Transfer 24, 277.

Incropera, F. P., Lavine, A. S., DeWitt, D. P., 2011. Fundamentals of Heat and Mass Transfer. John Wiley & Sons.

Jaikrishna, C. R., Aswatha, Rathan, R., Seetharamu, K., 2010. Effect of discrete heat sources on natural convection in a square cavity. In: Proceedings of the 37th National & 4th International Conference on Fluid Mechanics and Fluid Power.

Johnston, H., Doering, C. R., 2009. Comparison of turbulent thermal convection between conditions of constant temperature and constant flux. Physical Review Letters 102 (6), 064501.

Julien, K., Legg, S., McWILLIAMS, J., Werne, J., 1999. Plumes in rotating convection. Part 1. Ensemble statistics and dynamical balances. Journal of Fluid Mechanics 391, 151–187.

Kaczorowski, M., 2009. Untersuchung turbulenter thermischer Konvektion in kartesischen Geometrien mittels DNS und LES. Ph.D. thesis, Technische Universität Ilmenau.

Kaczorowski, M., Shishkin, A., Shishkina, O., Wagner, C., 2008. Developement of a numerical procedure for direct simulations of turbulent convection in a closed rectangular cell. In: New Results in Numerical and Experimental Fluid Mechanics VI. Springer, pp. 381–388.

Kaczorowski, M., Wagner, C., 2007. Direct numerical simulation of turbulent convection in a rectangular Rayleigh–Bénard cell. In: Proceedings of the 5th International Symposium on Turbulence and Shear Flow Phenomena. Vol. 2. pp. 499–504.

Kaczorowski, M., Wagner, C., 2009. Analysis of the thermal plumes in turbulent Rayleigh–Bénard convection based on well-resolved numerical simulations. Journal of Fluid Mechanics 618 (1), 89–112.

Kaczorowski, M., Wagner, C., 2010. Study on the resolution requirements for DNS in turbulent Rayleigh–Bénard convection. In: Notes on Numerical Fluid Mechanics and Multidisciplinary Design, Turbulence and Interactions. Vol. 110. Springer, pp. 199–206.

Kadanoff, L. P., 2001. Turbulent heat flow: Structures and scaling. Physics Today 54 (8), 34–39.

Kandaswamy, P., Nithyadevi, N., Ng, C., 2008. Natural convection in enclosures with partially thermally active side walls containing internal heat sources. Physics of Fluids 20 (9), 097104.

Kerr, R. M., 1996. Rayleigh number scaling in numerical convection. Journal of Fluid Mechanics 310, 139–179.

Kolmogorov, A. N., 1941. Dissipation of energy in the locally isotropic turbulence. In: Dokl. Akad. Nauk SSSR. Vol. 32. pp. 16–18.

Konstantinov, M., Lautenschlager, W., Shishkin, A., Wagner, C., 2014. Numerical simulation of the air flow and thermal comfort in aircraft cabins. In: New Results in Numerical and Experimental Fluid Mechanics IX. Springer, pp. 293–301.

Konstantinov, M., Rütten, M., Lambert, M., Wagner, C., 2009. Strahlung als wesentlicher Faktor der numerischen Simulation von Flugzeugkabineninnenströmungen für Komfortvorhersagen. In: Tagungsband des Deutschen Luft- und Raumfahrtkongresses. Vol. 501. p. 121285.

Kraichnan, R. H., 1962. Turbulent thermal convection at arbitrary Prandtl number. Physics of Fluids 5 (11), 1374–1389.

Krishnamurti, R., Howard, L. N., 1981. Large-scale flow generation in turbulent convection. Proceedings of the National Academy of Sciences 78 (4).

Kunnen, R., Clercx, H., Geurts, B., 2010. Vortex statistics in turbulent rotating convection. Physical Review E 82 (3), 036306.

Kunnen, R., Clercx, H., Geurts, B., Van Bokhoven, L., Akkermans, R., Verzicco, R., 2008. Numerical and experimental investigation of structure-function scaling in turbulent Rayleigh–Bénard convection. Physical Review E 77 (1), 016302.

Kwak, H. S., Hyun, J. M., 1996. Natural convection in an enclosure having a vertical sidewall with time-varying temperature. Journal of Fluid Mechanics 329, 65–88.

Lakhal, E., Hasnaoui, M., Vasseur, P., 1999. Numerical study of transient natural convection in a cavity heated periodically with different types of excitations. International Journal of Heat and Mass Transfer 42 (21), 3927–3941.

Lan, C., Ezekoye, O., Howell, J., Ball, K., 2003. Stability analysis for three-dimensional Rayleigh–Bénard convection with radiatively participating medium using spectral methods. International Journal of Heat and Mass Transfer 46 (8), 1371–1383.

Lienhard, J., 1987. An improved approach to conductive boundary conditions for the Rayleigh–Bénard instability. Journal of Heat Transfer 109 (2), 378–387.

Lienhard, J., 1990. Thermal radiation in Rayleigh–Bénard instability. ASME Transactions Journal of Heat Transfer 112, 100–109.

Lienhard IV, J., Lienhard V, J., 2008. A Heat Transfer Textbook, Third Edition. Phlogiston Press, Cambridge, MA, US.

Marshall, J., Schott, F., 1999. Open-ocean convection: Observations, theory, and models. Rev. Geophys 37 (1), 1–64.

Maxwell, J. C., 1863. A dynamical theory of the electromagnetic field. Proceedings of the Royal Society of London 13, 531–536.

Maystrenko, A., Resagk, C., Thess, A., 2007. Structure of the thermal boundary layer for turbulent Rayleigh–Bénard convection of air in a long rectangular enclosure. Physical Review E 75 (6), 066303.

Mishra, S. C., Prasad, M., 1998. Radiative heat transfer in participating media – A review. Sadhana 23 (2), 213–232.

Nielsen, P. V., 2009. Control of airborne infectious diseases in ventilated spaces. Journal of the Royal Society Interface 6 (Suppl 6), S747–S755.

Nielsen, P. V., Barszcz, E., Czarnota, T., Dymalski, D. P., Jasienski, M. A., Nowotka, A., Mozer, A., Wiankowska, S. M., Jensen, R. L., 2008. The influence of draught on a seat with integrated personalized ventilation. In: Proceedings of the 11th International Conference on Indoor Air Quality and Climate, Paper ID: 247.

Niemela, J., Skrbek, L., Sreenivasan, K., Donnelly, R., 2000. Turbulent convection at very high Rayleigh numbers. Nature 404 (6780), 837–840.

Niemela, J., Sreenivasan, K., 2003. Rayleigh-number evolution of large-scale coherent motion in turbulent convection. Europhysics Letters 62 (6), 829–833.

Nikolaenko, A., Brown, E., Funfschilling, D., Ahlers, G., 2005. Heat transport by turbulent Rayleigh–Bénard convection in cylindrical cells with aspect ratio one and less. Journal of Fluid Mechanics 523, 251–260.

Nithyadevi, N., Kandaswamy, P., Sivasankaran, S., 2006. Natural convection in a square cavity with partially active vertical walls: Time-periodic boundary condition. Mathematical Problems in Engineering 2006, 1–16.

Planck, M., 1900. Über eine verbesserung der wienschen spektralgleichung. verh. d. dt. phys. ges. 2, 202–204. abgedr. Phys. Vorträge und Abhandlungen Bd. l, S 687, 237–245.

Pompea, S. M., Breault, R. P., 2004. Black surfaces for optical systems. In: Bass, M. (Ed.), Handbook of Optics, 2nd ed. McGraw-Hill, Ch. 37.

Prandtl, L., 1905. Über Flüssigkeiten bei sehr kleiner Reibung. In: Verhandlungen des III Internationalen Mathematiker-Kongresses, Heidelberg. pp. 484–491.

Priestley, C., 1954. Convection from a large horizontal surface. Australian Journal of Physics 7 (1), 176–201.

Qiu, X.-L., Tong, P., 2001a. Large-scale velocity structures in turbulent thermal convection. Physical Review E 64 (3), 036304.

Qiu, X.-L., Tong, P., 2001b. Onset of coherent oscillations in turbulent Rayleigh–Bénard convection. Physical Review Letters 87 (9), 094501.

Qiu, X.-L., Tong, P., 2002. Temperature oscillations in turbulent Rayleigh–Bénard convection. Physical Review E 66 (2), 026308.

Rayleigh, L., 1916. On convection currents in a horizontal layer of fluid, when the higher temperature is on the under side. The London, Edinburgh, and Dublin Philosophical Magazine and Journal of Science 32 (192), 529–546.

Ridouane, E., Hasnaoui, M., Amahmid, A., Raji, A., 2004. Interaction between natural convection and radiation in a square cavity heated from below. Numerical Heat Transfer, Part A: Applications 45 (3), 289–311.

Ridouane, E., Hasnaoui, M., Campo, A., 2006. Effects of surface radiation on natural convection in a Rayleigh–Bénard square enclosure: Steady and unsteady conditions. Heat and Mass Transfer 42 (3), 214–225.

Roche, P.-E., Castaing, B., Chabaud, B., Hébral, B., Sommeria, J., 2001. Side wall effects in Rayleigh–Bénard experiments. The European Physical Journal B 24 (3), 405–408.

Roche, P.-E., Gauthier, F., Chabaud, B., Hébral, B., 2005. Ultimate regime of convection: Robustness to poor thermal reservoirs. Physics of Fluids (1994-present) 17 (11), 115107.

Saravanan, S., Sivaraj, C., 2013. Coupled thermal radiation and natural convection heat transfer in a cavity with a heated plate inside. International Journal of Heat and Fluid Flow 40, 54–64.

Schmitt, L., Friedrich, R., 1982. Numerische Simulation turbulenter Grenzschichten (Large-eddy-simulation). In: Technical Report 82/2. Institute für Strömungsmechanik, TU München.

Schmitt, L., Richter, K., Friedrich, R., 1986. Large-eddy simulation of turbulent boundary layer and channel flow at high Reynolds number. In: Schumann, U., Friedrich, R. (Eds.), Direct and Large Eddy Simulation of Turbulence. Vieweg, Braunschweig, pp. 161–176.

Schumann, U., 1973. Ein Verfahren zur direkten numerischen Simulation turbulenter Strömungen in Platten- und Ringspaltkanälen und über seine Anwendung zur Untersuchung von Turbulenzmodellen. Ph.D. thesis, TH Karlsruhe, KFK 1854.

Shang, X.-D., Qiu, X.-L., Tong, P., Xia, K.-Q., 2003. Measured local heat transport in turbulent Rayleigh–Bénard convection. Physical Review Letters 90 (7), 074501.

Shi, N., Emran, M. S., Schumacher, J., 2012. Boundary layer structure in turbulent Rayleigh–Bénard convection. Journal of Fluid Mechanics 706, 5.

Shishkina, O., Shishkin, A., Wagner, C., 2009. Simulation of turbulent thermal convection in complicated domains. Journal of Computational and Applied Mathematics 226 (2), 336–344.

Shishkina, O., Stevens, R. J., Grossmann, S., Lohse, D., 2010. Boundary layer structure in turbulent thermal convection and its consequences for the required numerical resolution. New Journal of Physics 12 (7), 075022.

Shishkina, O., Wagner, C., 2004. Stability conditions for the leapfrog–Euler scheme with central spatial discretization of any order. Applied Numerical Analysis & Computational Mathematics 1 (1), 315–326.

Shishkina, O., Wagner, C., 2006. Analysis of thermal dissipation rates in turbulent Rayleigh–Bénard convection. Journal of Fluid Mechanics 546, 51–60.

Shishkina, O., Wagner, C., 2007a. Boundary and interior layers in turbulent thermal convection in cylindrical containers. International Journal of Computing Science and Mathematics 1 (2), 360–373.

Shishkina, O., Wagner, C., 2007b. A fourth order finite volume scheme for turbulent flow simulations in cylindrical domains. Computers & Fluids 36 (2), 484–497.

Shishkina, O., Wagner, C., 2008. Analysis of sheet-like thermal plumes in turbulent Rayleigh–Bénard convection. Journal of Fluid Mechanics 599, 383–404.

Shishkina, O., Wagner, S., Horn, S., 2014. Influence of the angle between the wind and the isothermal surfaces on the boundary layer structures in turbulent thermal convection. Physical Review E 89 (3), 033014.

Shraiman, B. I., Siggia, E. D., 1990. Heat transport in high-Rayleigh-number convection. Physical Review A 42 (6), 3650.

Siggia, E. D., 1994. High Rayleigh number convection. Annual Review of Fluid Mechanics 26 (1), 137–168.

Spalart, P., Jou, W., Strelets, M., Allmaras, S., Liu, C., Liu, Z., 1997. Comments on the feasibility of LES for wings and on a hybrid RANS/LES approach. Advances in DNS/LES 1, 4–8.

Sreenivasan, K. R., Bershadskii, A., Niemela, J., 2002. Mean wind and its reversal in thermal convection. Physical Review E 65 (5), 056306.

Stefan, J., 1879. Über die Beziehung der Wärmestrahlung und der Temperatur. Sitzungs berichte d. K. Akademie d. Wissenschaften, Mathematische-Naturwissenschaftliche Classe Abteilung II (7), 391–428.

Stevens, R. J., Lohse, D., Verzicco, R., 2011. Prandtl and Rayleigh number dependence of heat transport in high Rayleigh number thermal convection. Journal of Fluid Mechanics 688, 31–43.

Stevens, R. J., van der Poel, E. P., Grossmann, S., Lohse, D., 2013. The unifying theory of scaling in thermal convection: The updated prefactors. Journal of Fluid Mechanics 730, 295–308.

Stevens, R. J., Verzicco, R., Lohse, D., 2010. Radial boundary layer structure and nusselt number in Rayleigh–Bénard convection. Journal of Fluid Mechanics 643, 495.

Swarztrauber, P. N., 1974. A direct method for the discrete solution of separable elliptic equations. SIAM Journal on Numerical Analysis 11 (6), 1136–1150.

Swarztrauber, P. N., Sweet, R., 1975. Efficient FORTRAN subprograms for the solution of elliptic partial differential equations. In: Technical Report IA-109. National Center for Atmospheric Research Boulder, Colorado.

Threlfall, D., 1975. Free convection in low-temperature gaseous helium. Journal of Fluid Mechanics 67 (01), 17–28.

Triveni, M. K., Sen, D., Panua, R., 2014. Laminar natural convection for thermally active partial side walls in a right-angled triangular cavity. Arabian Journal for Science and Engineering 39 (12), 9025–9038.

Unger, F., 1994. Numerische Simulation turbulenter Rohrstromungen. Ph.D. thesis, Technische Univerität München.

VDI-Gesellschaft Verfahrenstechnik und Chemieingenieurwesen and others, 2010. VDI Heat Atlas.

Verzicco, R., 2004. Effects of nonperfect thermal sources in turbulent thermal convection. Physics of Fluids 16, 1965–1979.

Verzicco, R., Sreenivasan, K., 2008. A comparison of turbulent thermal convection between conditions of constant temperature and constant heat flux. Journal of Fluid Mechanics 595 (1), 203–219.

Villermaux, E., 1995. Memory-induced low frequency oscillations in closed convection boxes. Physical Review Letters 75 (25), 4618.

Wagner, C., 1996. Direkte numerische Simulation turbulenter Strömungen in einer Rohrerweiterung. Ph.D. thesis, Dissertation an der Technischen Univerität München, Fortschr.-Ber. VDI Reihe 7 Nr. 283, VDI-Verlag, Düsseldorf, Germany.

Wagner, C., 2014. Systeme und Technologien für das Energiemanagement in leistungsoptimierten Flugzeugarchitekturen. In: Schlussbericht des Vorhabens FKZ 20Y0907B. Deutsches Zentrum für Luft- und Raumfahrt, Göttingen.

Wagner, C., Friedrich, R., Narayanan, R., 1994. Comments on the numerical investigation of Rayleigh and Marangoni convection in a vertical circular cylinder. Physics of Fluids 6 (4), 1425–1433.

Wagner, S., Shishkina, O., 2013. Aspect-ratio dependency of Rayleigh–Bénard convection in box-shaped containers. Physics of Fluids 25, 85–110.

Wagner, S., Shishkina, O., Wagner, C., 2012. Boundary layers and wind in cylindrical Rayleigh–Bénard cells. Journal of Fluid Mechanics 697, 336–366.

Webb, B., Viskanta, R., 1987. Analysis of radiation-induced natural convection in rectangular enclosures. Journal of Thermophysics and Heat Transfer 1 (2), 146–153.

Weiss, S., Seiden, G., Bodenschatz, E., 2014. Resonance patterns in spatially forced Rayleigh–Bénard convection. Journal of Fluid Mechanics 756, 293–308.

Wittenberg, R. W., 2010. Bounds on Rayleigh–Bénard convection with imperfectly conducting plates. Journal of Fluid Mechanics 665, 158–198.

Wu, X.-Z., Libchaber, A., 1992. Scaling relations in thermal turbulence: The aspect-ratio dependence. Physical Review A 45 (2), 842.

Xi, H.-D., Lam, S., Xia, K.-Q., 2004. From laminar plumes to organized flows: The onset of large-scale circulation in turbulent thermal convection. Journal of Fluid Mechanics 503, 47–56.

Xu, B., Ai, X., Li, B., 2007. Stabilities of combined radiation and Rayleigh–Bénard–Marangoni convection in an open vertical cylinder. International Journal of Heat and Mass Transfer 50 (15), 3035–3046.

Yücel, A., Acharya, S., Williams, M., 1989. Natural convection and radiation in a square enclosure. Numerical Heat Transfer 15 (2), 261–278.

Zhou, Q., Sun, C., Xia, K.-Q., 2007. Morphological evolution of thermal plumes in turbulent Rayleigh–Bénard convection. Physical Review Letters 98 (7), 074501.

Zhou, S.-Q., Xia, K.-Q., 2002. Plume statistics in thermal turbulence: Mixing of an active scalar. Physical Review Letters 89 (18), 184502.